

PROPERTIES AND APPLICATIONS OF LASER
INDUCED GRATINGS IN RARE
EARTH DOPED GLASSES

By

EDWARD G. BEHRENS

Bachelor of Science
Southeastern Oklahoma State University
Durant, Oklahoma
1984

Master of Science
Oklahoma State University
Stillwater, Oklahoma
1986

Submitted to the Faculty of the
Graduate College of the
Oklahoma State University
in partial fulfillment of
the requirements for
the Degree of
DOCTOR OF PHILOSOPHY
July, 1989

Thesis
1989D
B451P
Lop. 2

PROPERTIES AND APPLICATIONS OF LASER
INDUCED GRATINGS IN RARE
EARTH DOPED GLASSES

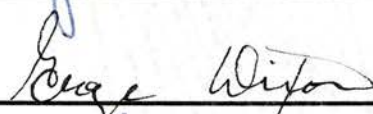
Thesis Approved:



Thesis Adviser











Dean of Graduate College

ACKNOWLEDGMENTS

I would like to express my thanks to all of the people responsible for helping me during my studies at Oklahoma State University. Foremost among these is my thesis adviser, Dr. Richard C. Powell. I want to thank him for giving me a chance to work in his laboratory and also for his guidance and patience throughout the time spent here at Oklahoma State University. I also wish to thank the other members of my committee, Dr. George S. Dixon, Dr. Hugh L. Scott, Dr. Stephen W. McKeever, and Dr. Elizabeth M. Holt. Special thanks go to Dr. Frederic M. Durville for his assistance in performing some of the measurements.

Financial support was provided by the U. S. Army Research Office. Samples for this work were provided by Dr. Douglas H. Blackburn of the National Institute of Standards and Technology.

TABLE OF CONTENTS

Chapter		Page
I.	INTRODUCTION	1
	Statement of the Problem	1
	Outline of Thesis	2
II.	PROPERTIES OF LASER-INDUCED GRATINGS	4
	Introduction	4
	Experimental Procedures	7
	Properties of the Active Ions	17
	Properties of the Host Glass	48
	Two-Level System Model	65
	Summary and Conclusions	75
III.	APPLICATIONS OF LASER-INDUCED GRATINGS	78
	Introduction	78
	Experimental Configuration	79
	Holographic Information Storage	79
	Demultiplexing Results	80
	Signal Modulation	94
	Summary and Conclusions	96
IV.	SUMMARY AND CONCLUSIONS	98
	Summary of Thesis	98
	Future Work	100
	BIBLIOGRAPHY	102
	APPENDIX	105

LIST OF TABLES

Table		Page
I.	LIG Signal Intensity as a Function of Write Beam Crossing Angle $2\Theta_A$ in Pr^{3+} Sample.	20
II.	Build-Up and Erase Times of the Permanent LIG as a Function of the Total Write Beam Crossing Angle $2\Theta_A$ in Pr^{3+} Sample.	23
III.	LIG Signal Intensity as a Function of the Total Laser Write Beam Power in Pr^{3+} Sample.	26
IV.	Build-Up and Erase Time of the Permanent LIG as a Function of the Total Laser Write Beam Power in Pr^{3+} Sample.	29
V.	Summary of Parameters from Thermal Lensing Experiments	44
VI.	Sample Compositions	49
VII.	Experimental Values of the Effective Scattering Intensity as a Function of the Mass of the Alkali-Metal Ion	60
VIII.	Experimental Values of the Scattering Intensity as a Function of the Temperature	62
IX.	Activation Energies of Alkali-Metal Glasses	64
X.	Summary of Parameters from Two-Level System Model	73
XI.	Values of Activation Energy and Asymmetry	74
XII.	Signal Intensity as a Function of Probe Beam Angle for MP10 Sample	83
XIII.	Signal Intensity as a Function of Probe Beam Angle for LS5 Sample	87

LIST OF FIGURES

Figure		Page
1.	Time Evolution of the Build-Up, Transient Decay, and Erasure of LIG Signals in a Eu^{3+} -Doped Glass.	5
2.	Experimental Configuration to Produce Laser-Induced Gratings . . .	8
3.	Write Session Parameters.	9
4.	Wavevectors for Grating Formation.	11
5.	Read Session Parameters.	13
6.	Experimental Setup for Measuring Laser-Induced Changes in the Refractive Index.	15
7.	LIG Signal Intensity as a Function of Write Beam Crossing Angle $2\Theta_A$ in Pr^{3+} Sample.	18
8.	Build-Up Time of the Permanent LIG Signal as a Function of the Total Write Beam Crossing Angle $2\Theta_A$ in Pr^{3+} Sample.	20
9.	Erase Time of the Permanent LIG Signal as a Function of the Total Write Beam Crossing Angle $2\Theta_A$ in Pr^{3+} Sample.	21
10.	LIG Signal Intensity as a Fuction of the Total Laser Write Beam Power in Pr^{3+} Sample.	24
11.	Build-Up Time of the Permanent LIG as a Function of the Total Laser Write Beam Power in Pr^{3+} Sample.	27
12.	Erase Time of the Permanent LIG as a Function of the Total Laser Write Beam Power in Pr^{3+} Sample.	28
13.	Partial Energy Level Diagram for Several Trivalent Rare Earth Ions.	30
14.	Room Temperature Fluorescence of the Pr^{3+} -Doped Glass Sample after Excitation Into the $^3\text{P}_0$ Excited State.	31

Figure	Page
15. Room Temperature Fluorescence of the Er^{3+} -Doped Glass Sample after Excitation Into the ${}^4\text{F}_{7/2}$ Excited State.	34
16. Spatial Profile of Transmitted Probe Beam as a Function of Excitation Beam Power in NP.	36
17. Spatial Profile of Transmitted Probe Beam as a Function of Excitation Beam Power in ED2 Silicate Glass.	37
18. Time Evolution of the Intensity at the Center of the Transmitted Probe Beam for the NP Sample.	39
19. Time Evolution of the Intensity at the Center of the Transmitted Probe Beam for the EP Sample.	40
20. Theoretical Fit of the Time Evolution of the Signal in the NP Sample.	43
21. Raman Spectra (Dashed Line) and Resonant Raman Spectra (Solid Line) of Europium Pentaphosphate Glass.	51
22. Raman Spectra (Dashed Line) and Resonant Raman Spectra (Solid Line) of Eu^{3+} -Doped Lithium Phosphate Glass.	52
23. Raman Spectra (Dashed Line) and Resonant Raman Spectra (Solid Line) of Eu^{3+} -Doped Sodium Silicate Glass.	53
24. Raman Spectra (Dashed Line) and Resonant Raman Spectra (Solid Line) of Eu^{3+} -Doped Lithium Silicate Glass.	54
25. Scattering Efficiency of Silicate Glass Samples as a Function of the Alkali-Metal Ion.	59
26. Temperature Dependence of LIG Scattering Intensity for Alkali-Metal Glasses.	61
27. Two-Level System Model.	67
28. Intensity of LIG Signal as a Function of the Angle Between the Probe Beam and the Perpendicular to the MP10 Sample.	81
29. Angle in the Sample at Which Maximum Scattering Intensity Occurs Versus Probe Beam Wavelength in the MP10 Sample.	88

Figure	Page
30. Definition of Bragg Angle and Other Angles Involved in Grating Spacing Calculation.	91
31. Definition of Angles Involved in Thermal Lensing Process.	93
32. From Top to Bottom: Write, Probe, and Signal Beam Intensities in Modulation Experiment.	95

CHAPTER I

INTRODUCTION

During the past decade, a significant amount of work has been performed in the development of new optical devices designed to provide functions such as switching, modulation, phase conjugation, and bistability which are important in optical data processing applications. Glasses are very attractive materials for these devices because of their low cost and ease of fabrication compared to single crystals, and because they provide the opportunity for developing monolithic devices within systems based on fiber-optic transmission. Laser-induced refractive-index changes have been observed in several types of glasses [1, 2, 3, 4, 5] and used to produce holographic storage, narrow-band filters, optical switching, and phase conjugation. In most cases, the physical mechanism producing the photorefractive change has not been explained.

Statement of the Problem

In order to create new optical devices which operate on the basis of refractive index changes in glasses the physical mechanisms responsible for these changes need to be understood. One spectroscopic technique for investigating the laser-induced change in the refractive index is four-wave-mixing (FWM)[6] which produces a laser-induced grating (LIG) in the material. The physical processes underlying the LIGs that give rise to FWM signals are of significant importance to the development of new optical devices and in understanding laser-induced damage. The purpose of this thesis is to present new results of measurements performed on superimposed transient and permanent gratings in rare earth-doped glasses and

describe the mechanism responsible for the formation of these gratings. The type of glasses investigated in this thesis include common silicate and phosphate glasses which can be made into fibers, and thus the LIG devices can be used in fiber optic systems. It is also the purpose of this thesis to demonstrate potential applications of permanent LIGs in these glasses by creating some simple optical devices.

Outline of Thesis

In the next chapter a brief discussion of LIGs and the experimental procedure employed to produce LIGs in rare earth-doped glasses is presented along with a brief review of what has been accomplished previously. The results obtained from new experiments are separated into two sections, those related to the rare earth ion, and those related to the glass host.

In the section pertaining to the rare earth ion the first results presented are those obtained from a Pr^{3+} -doped silicate glass. These results are discussed in terms of an empirical two-level system model. The results of fluorescence measurements performed on the Pr^{3+} -doped silicate glass and an Er^{3+} -doped silicate glass are presented next. These results are used to explain the inability to produce permanent LIGs in some of the glasses. To further investigate these results thermal lensing measurements are performed on Eu^{3+} and Nd^{3+} -doped phosphate glasses. The final part of this section contains additional experiments which investigate the affect of write beam polarization and wavelength on the formation of permanent LIGs.

In the section on the glass host the results of investigating numerous hosts doped with Eu^{3+} are presented. Several of these glasses are then examined through Raman scattering. These results are discussed in terms of the various structures of the hosts. The final results reported in this section are concerned with the affect of the network modifier ions on the permanent LIG. The intensity and temperature dependence of the permanent LIG is measured as a function of the mass of the network modifier ion.

The next section in Chapter II uses a two-level system model to derive an equation for the permanent LIG signal intensity. This equation is fit to the experimental results obtained in the previous section and quantitative values are obtained for the parameters of the two-level system model. These parameters are compared with experimental results and related to the physical structure of the glass sample.

Chapter III discusses potential applications of LIGs in optical devices. Several experiments are performed which demonstrate the feasibility of using these glasses for the development of new devices. These include: measuring the long-term stability of the permanent LIG and discussing its applications to information storage, demultiplexing multifrequency laser beams to demonstrate applications such as frequency selective filters, and modulating the permanent LIG signal intensity to produce beam-to-beam information transfer.

Chapter IV summarizes the results of this thesis and presents suggestions for future work.

CHAPTER II

PROPERTIES OF LASER-INDUCED GRATINGS

Introduction

FWM processes are currently of significant interest in science and technology owing to their importance in modern optics applications such as phase conjugation and because they provide a powerful spectroscopic tool for probing the properties of the interaction of light and matter. The physical processes underlying the LIGs that give rise to FWM signals can be placed into two categories according to their decay times after the laser write beams have been turned off. The first is that of transient gratings with fast decay times, and the second is that of permanent gratings (also referred to as holographic gratings), which remain for a long time after the laser write beams have been turned off. The change in the refractive index associated with a LIG can be due to a number of physical processes [7]. These include the nonlinear susceptibility of bound electrons or free electrons, thermal changes in the refractive index, density fluctuations, charge relocation, and the difference in the susceptibility of ions in an excited state compared to the ground state. This last type of LIG is called a population grating since the density of ions in the excited state varies spatially in the form of a sine wave.

In 1986 we reported the first observations of FWM signals in Eu^{3+} -doped glasses which displayed a transient component associated with a Eu^{3+} population grating and a permanent component associated with a holographic grating [8, 9]. The purpose of this chapter is to report the results of new research in this area which provides additional information relevant to the understanding of the mechanism responsible for producing the permanent LIG.

Figure 1 displays a typical time evolution of the signal obtained at room

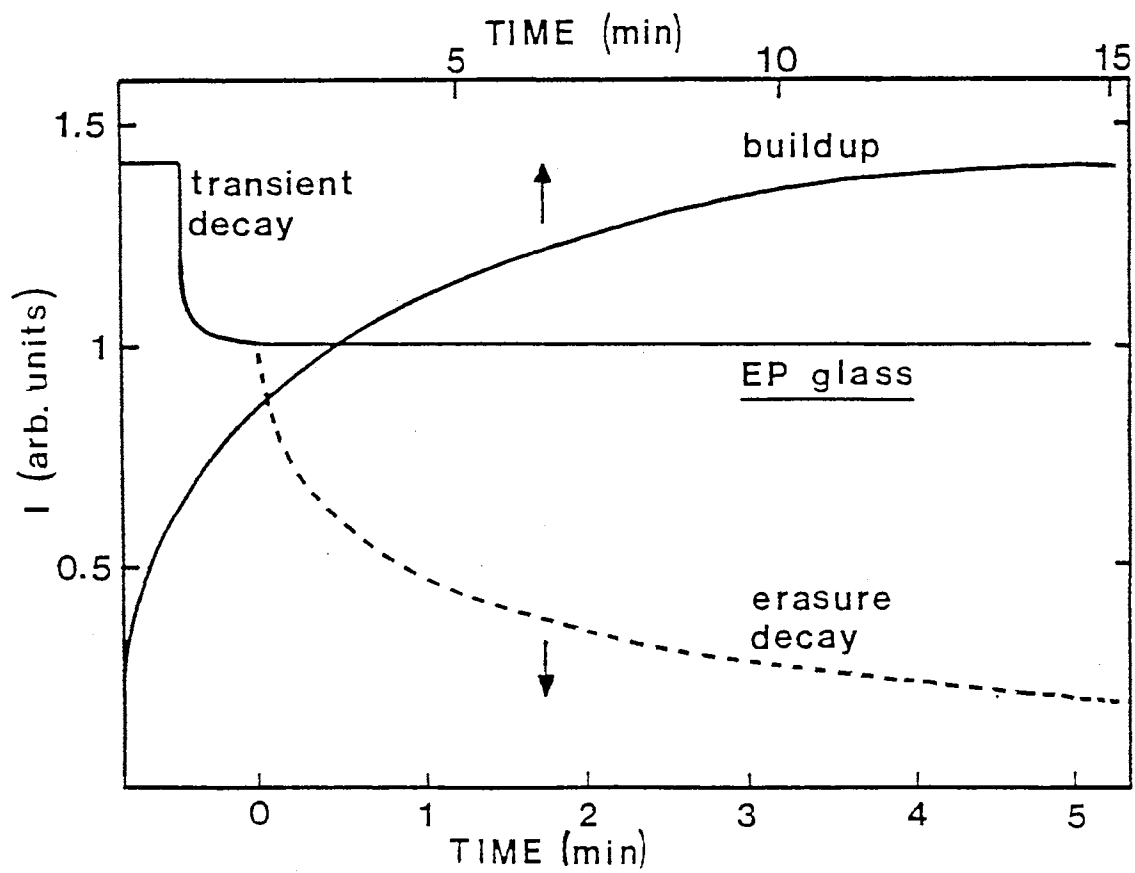


Figure 1. Time Evolution of the Build-Up, Transient Decay, and Erasure of LIG Signals in a Eu^{3+} -doped Glass.

temperature by scattering from a LIG in a Eu^{3+} -doped glass, however this behavior is typical of LIG signals in other rare earth-doped glasses although the time scale may change. The laser write beams are tuned to resonance with a transition to a highly excited state of the rare earth ion. The signal immediately appears at a relatively low intensity and then slowly builds up to its maximum level. In the Eu^{3+} -doped sample this build-up took several minutes. When the write beams are turned off, the signal beam decays rapidly but not to zero. It levels off at a relatively high intensity and remains there permanently. If the two write beams are turned back on, the signal will rapidly return to its maximum value. If the sample temperature is raised, the grating will be thermally erased and the signal will decay to zero. If the sample is exposed to a single laser beam tuned to resonance with the same absorption transition used to write the grating, the grating will be optically erased and the signal will decay to zero. In the Eu^{3+} -doped sample the erasure times are again of the order of several minutes.

The general signal characteristics described above are consistent with producing two superimposed gratings, one transient grating and one permanent grating. The transient LIG is responsible for the fast components of the signals initial buildup and initial decay. It has the characteristics of a population grating associated with the difference in the complex refractive index of the material when the rare earth ions are in the metastable state versus the ground state. The response times for writing and erasing this grating are associated with the pumping and decay rates of the metastable state of the rare earth ion. The permanent LIG is responsible for the long-lived signal. It has the characteristics of a grating associated with a local structural phase transition. The properties of the permanent LIG are discussed further in a later section. They indicate that the radiationless relaxation processes occurring in the laser excited rare earth ion produce enough local heating to cause the structural phase transition which results in a local change in the refractive index.

Population gratings have been observed in several rare earth-doped glasses [7, 8, 9, 10, 11] and theoretically should be observable for all trivalent rare earth ions

if the metastable state lifetime is long enough and the ion density high enough. Attempts to produce permanent LIGs have been less successful in these glasses indicating the importance of having both ions and hosts with very specific types of physical properties.

Seven different types of oxide and fluoride glasses doped with Eu^{3+} were studied previously [8, 9]; three of these exhibited permanent LIGs (europium pentaphosphate, lithium phosphate, and sodium silicate) and four did not (lithium silicate, lithium borate, lithium germanate, and zirconium fluoride). An empirical model was suggested to explain the origin of these gratings based on having a local glass structure at the site of the Eu^{3+} ions which allows each electronic state to be described by a double-minima potential curve. It is assumed in this model that the refractive index of the material is different, depending on which potential minimum is occupied by the Eu^{3+} ions. It is further assumed that the heat generated through radiationless relaxation of the excited Eu^{3+} ions can cause the local structure to change so that the ions move from one potential minimum to the other.

The model described above is consistent with the results reported previously, but further work is required to better understand the physical processes involved. The work reported in this chapter extends previous investigations by looking at different types of glass hosts, different rare earth ions and different excitation wavelengths. In the last section of this chapter the two-level system model is developed quantitatively and its predictions are discussed in terms of the FWM signal intensity.

Experimental Procedures

The experimental configuration used to produce LIGs in rare earth-doped glasses is displayed in Fig. 2. The output of a cw Ar^+ ion laser tuned in resonance with an absorption transition of the rare earth ion dopant is split into two beams and crossed inside the sample at an angle $2\Theta_S$ as defined in Fig. 3. These two beams are referred to as the “write” beams and have wavelength λ_W . It should be pointed

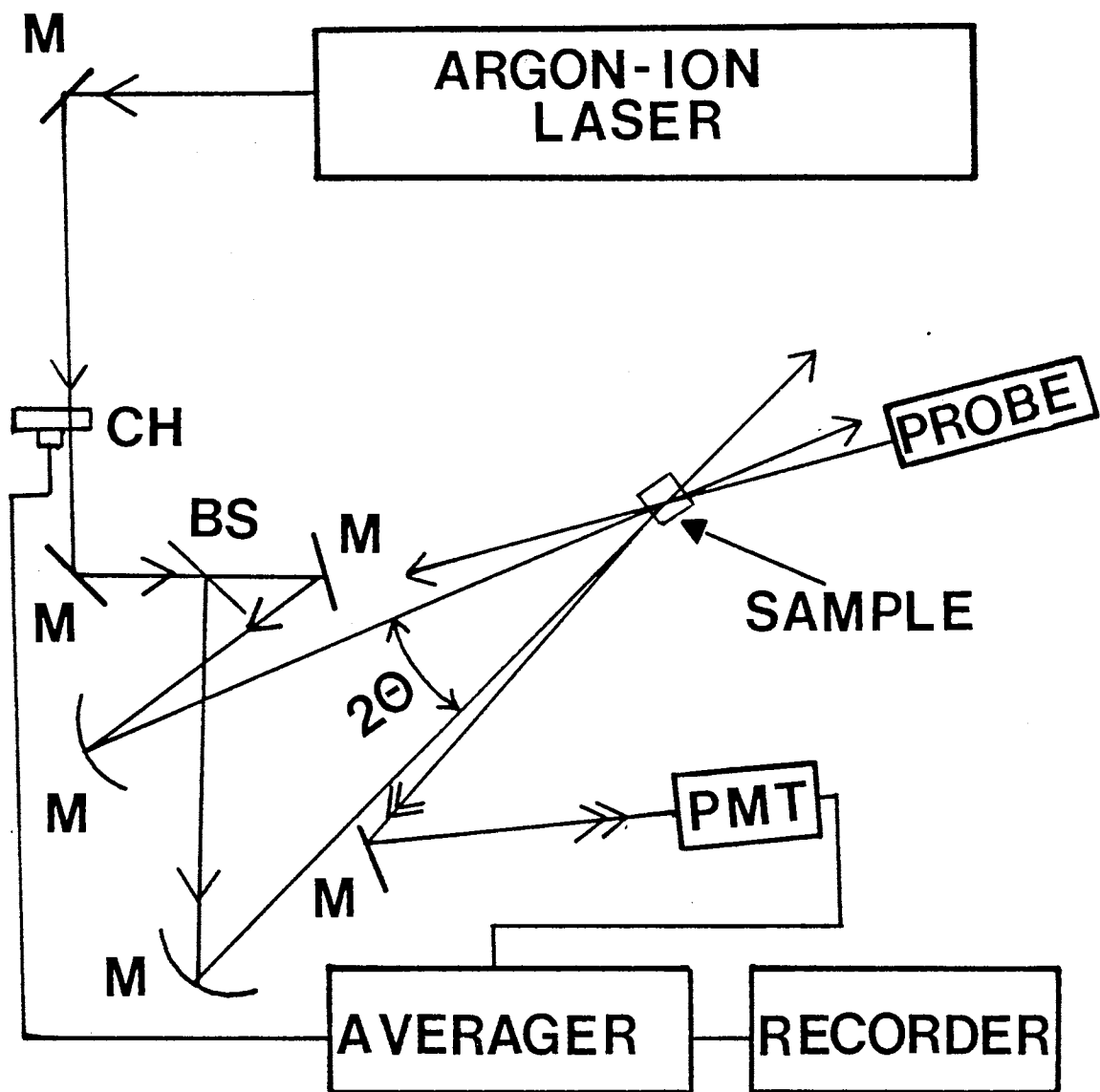


Figure 2. Experimental Configuration to Produce Laser-Induced Gratings

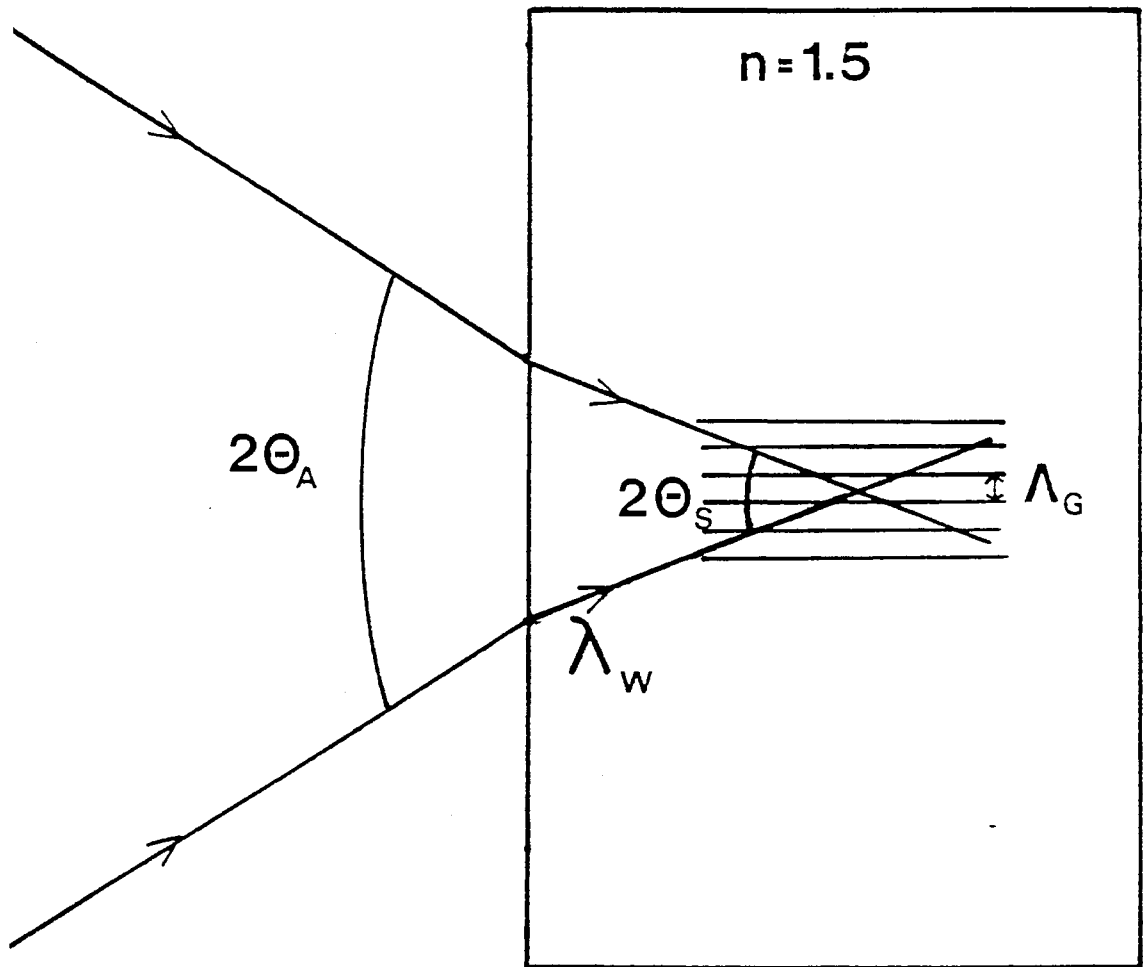


Figure 3. Write Session Parameters.

out here that the subscripts S and A refer to angles measured in the sample and air respectively, and for all calculations laser wavelengths are corrected for the index of refraction. The laser is operated in the Gaussian mode and the path lengths of the write beams are maintained equal to within the coherence length of the laser. When the two coherent Gaussian beams cross inside the sample a sinusoidal interference pattern will be created. This light intensity pattern interacts with the optical properties of the sample altering its refractive index. This results in a spatially modulated refractive index in the form of a sine wave. For the experiments performed here the spacing between the peaks of the modulated refractive index is the same as the spacing between the peaks of the light interference pattern.

To calculate the spacing between the peaks of the light interference pattern consider the laser write beams as traveling waves which have the form [12]

$$\vec{E}_1 = \vec{E}_0 \exp i(\vec{k}_1 \cdot \vec{r} - \omega_1 t) \quad (1)$$

$$\vec{E}_2 = \vec{E}_0 \exp i(\vec{k}_2 \cdot \vec{r} - \omega_2 t). \quad (2)$$

In the region where these beams cross the total electric field will be the vector sum of the original two beams. The light intensity in this region is given by the absolute square of the total electric field which in this case is given by

$$I \propto |(\vec{E}_1 + \vec{E}_2) \cdot (\vec{E}_1 + \vec{E}_2)|^2. \quad (3)$$

Thus the intensity of the light in the overlap region is found to be

$$I \propto |\vec{E}_0|^2 \left\{ 2 + 2 \exp \left[(\vec{k}_1 - \vec{k}_2) \cdot \vec{r} - (\omega_1 - \omega_2)t \right] \right\}. \quad (4)$$

The wavevector associated with the light intensity pattern is called the grating wavevector, \vec{k}_G , and is given by $\vec{k}_G = \vec{k}_1 - \vec{k}_2$. This is displayed graphically in Fig. 4. With a coordinate system as defined in Fig. 4 the intensity component of interest is that in the z direction, thus setting x=y=0 the intensity along the z axis is

$$I(0, 0, z, t) \propto |\vec{E}_0|^2 \left\{ 2 + 2 \cos [(k_{1z} - k_{2z})\hat{z} \cdot z\hat{z} - (\omega_1 - \omega_2)t] \right\} \quad (5)$$

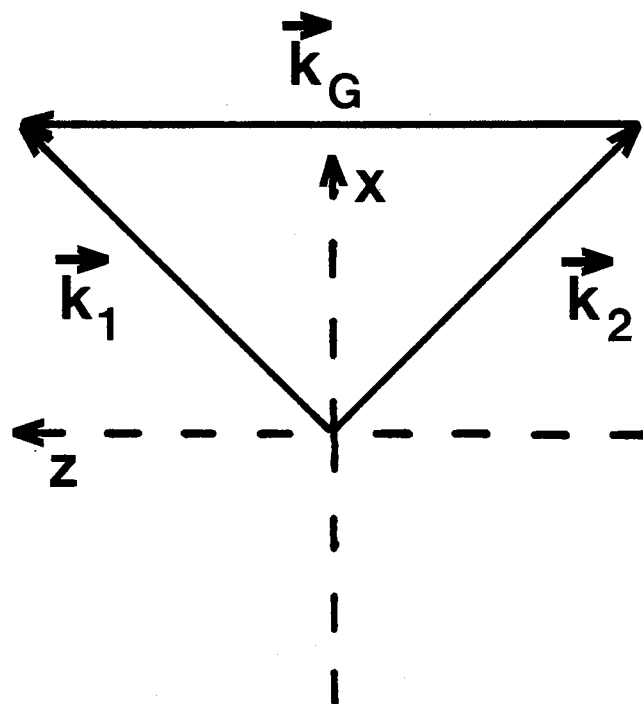


Figure 4. Wavevectors for Grating Formation.

where k_{1z} and k_{2z} are the z-components of \vec{k}_1 and \vec{k}_2 , respectively. The magnitude of these components are given by

$$k_{1z} = k_1 \sin \Theta_S \quad (6)$$

$$k_{2z} = k_2 \sin \Theta_S \quad (7)$$

where k_1 and k_2 are the magnitudes of \vec{k}_1 and \vec{k}_2 , respectively, and Θ_S is half the write beam crossing angle as defined in Fig. 3. When these are substituted into Eq. 5 the intensity in the z-direction becomes

$$I(0, 0, z, t) \propto |\vec{E}_0|^2 \{2 + 2 \cos [z(k_1 \sin \Theta_S + k_2 \sin \Theta_S) - (\omega_1 - \omega_2)t]\}. \quad (8)$$

For identical write beams, which are present in these experiments, $k_1 = k_2 = k$ and $\omega_1 = \omega_2$, which gives the intensity along the z-axis as

$$I(0, 0, z, t) \propto |\vec{E}_0|^2 \{2 + 2 \cos(2kz \sin \Theta_S)\}. \quad (9)$$

Thus it is seen that the intensity along the z-axis displays a constant background with a sinusoidally varying component superimposed on top of it. For the purpose of the experiments performed here only the sinusoidal component is of interest. Looking at just this sinusoidal component it is seen that the intensity will vary between a minimum and a maximum as z goes from 0 to $2\pi n/2k \sin \Theta_S$. Therefore, the LIG will display a grating wavelength of

$$\Lambda_G = 2\pi n/2k \sin \Theta_S. \quad (10)$$

The magnitude of the wavevector \vec{k} is $2\pi/\lambda_W$ so that the wavelength, or spacing between fringes, of the LIG is

$$\Lambda_G = \frac{n\lambda_W}{2 \sin \Theta_S}. \quad (11)$$

The LIG is probed by a beam from a He-Ne laser, called the probe beam, with wavelength λ_P which makes an angle Φ_S with the perpendicular to the sample surface as shown in Fig. 5. The spatially modulated refractive index appears as a diffraction grating to the probe beam and a portion of the He-Ne beam is diffracted

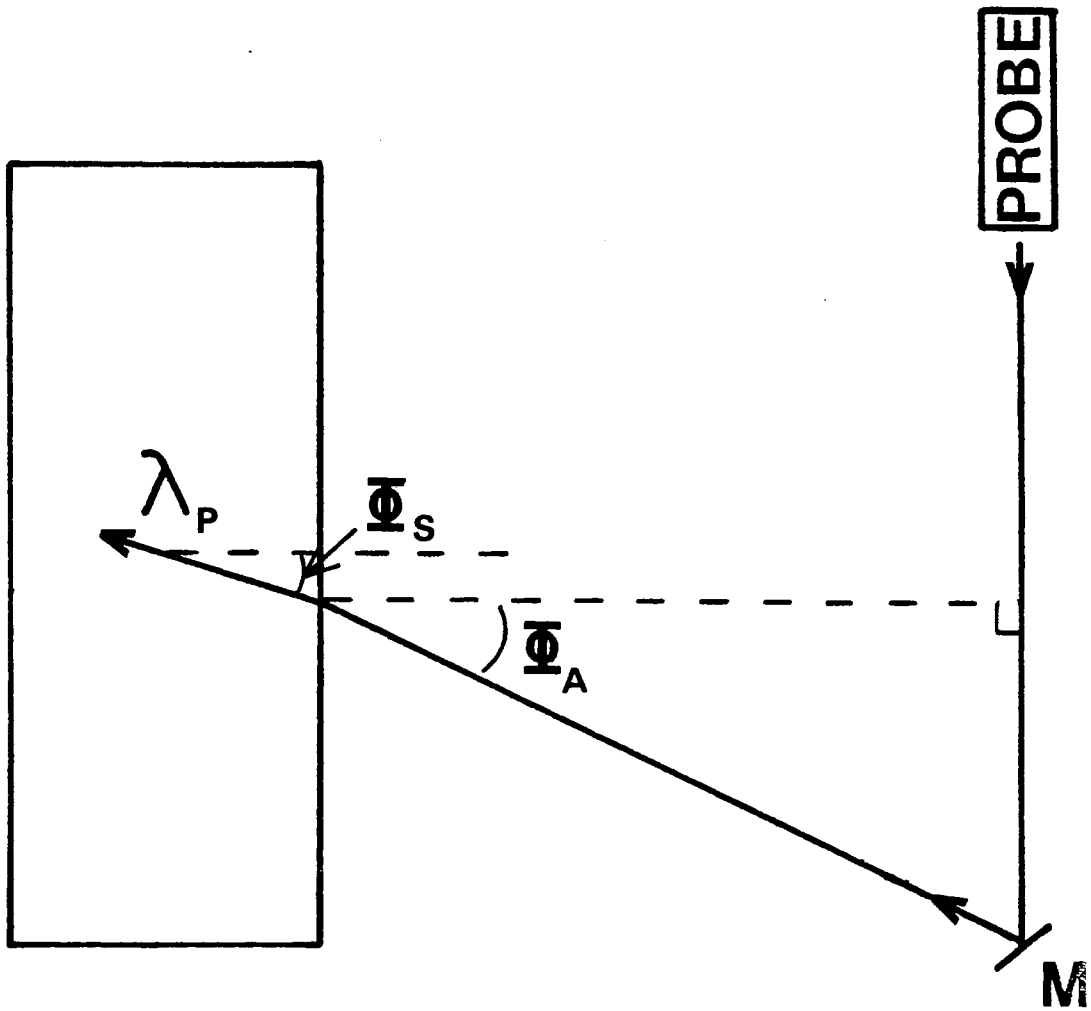


Figure 5. Read Session Parameters.

by this grating. To obtain the maximum signal intensity from the diffracted beam, the He-Ne beam is aligned with respect to the LIG to fulfill the Bragg scattering condition

$$n\lambda_P = 2\Lambda_G \sin \Theta_B \quad (12)$$

where Θ_B is the Bragg angle.

The portion of the probe beam diffracted by the LIG is called the signal beam and is detected by a photomultiplier tube. A monochromator or cut-off filters are used to minimize stray scattered light and sample fluorescence and the signal is recorded on a strip chart recorder. To study the transient response of the signal, a chopper is used to turn the write beams on and off while a boxcar averager is used to process the signal before sending it to the recorder. A pulse generator is used to control the chopper and trigger the boxcar averager. To determine the absolute intensity of the signal beam a calibrated power meter is used.

A number of experimental parameters can be varied in characterizing the properties of the LIGs. The wavelength of the laser write beams can be changed and in some cases a tunable dye laser is pumped by the argon laser to obtain a broader tuning range. A variable neutral density filter is used in front of the laser to measure the affect of the power of the laser write beams. By changing the crossing angle of the write beams the spacing of the LIG can be changed according to Eq. 11. The sample is placed in either a cryogenic refrigerator or a furnace to control the temperature. To study the optical erasure of the LIGs, a single beam from the argon laser is used as an erase beam.

The major parameters of interest in characterizing the LIGs are the maximum scattering efficiency, the writing and erasure times, the power needed to write the LIG, the temperature dependence of the LIG, and the long-term stability of the gratings at ambient temperature.

The experimental setup used for thermal lensing measurements is shown in Fig. 6. The excitation source is a Spectra-Physics Model 164 argon laser. Several different output lines can be chosen so that the experiments can be performed either in resonance or out of resonance with an electronic transition of the rare

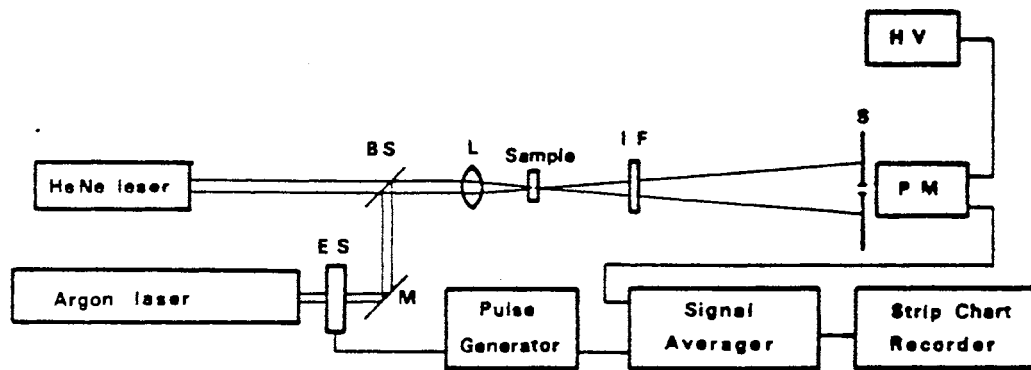


Figure 6. Experimental Setup for Measuring Laser-Induced Changes in the Refractive Index.

earth ions. The 4658 Å line is used to excite resonantly the ${}^7F_0-{}^5D_2$ transition of Eu^{3+} in the EP glass (composition to be given later). The 5145 Å line is used for off-resonance excitation of the EP glass and for resonance excitation of the ${}^4I_{9/2}-{}^2G_{9/2}$ transition of the Nd^{3+} in the NP glass (composition to be given later). The 4880 Å line is used for off-resonance excitation of the NP glass. An electronic shutter is used to switch the laser beams on and off, and their power is varied through the laser power supply and neutral density filters. A 10-mW He-Ne laser is used as a probe beam to detect changes in the index of refraction induced by the excitation beam. The weak beam at this wavelength does not cause a perturbation of the refractive index.

For thermal lensing studies, the excitation and probe beams are collinear and focused inside the sample with a 76.2-mm focal length lens. The transmitted excitation beam is filtered out, and the intensity at the center of the probe beam is detected through a pinhole by a Hamamatsu R1547 photomultiplier tube. The signal is processed by an EG&G/PAR signal averager and read out on a strip-chart recorder.

Properties of the Active Ions

To determine the role played by the rare earth ion dopant in the formation of the permanent LIGs experiments were conducted on glass samples doped with Eu^{3+} , Pr^{3+} , Nd^{3+} , and Er^{3+} . Of these four samples permanent LIGs were seen only in those doped with Eu^{3+} and Pr^{3+} . The characteristics of the permanent LIG in Eu^{3+} -doped glasses were described previously [8, 9, 13]. The properties of the LIG in the Pr^{3+} -doped sample have just recently been investigated and are listed below [11].

The characteristics of the LIG in a Pr^{3+} -doped silicate glass (70 SiO_2 , 15 Na_2O , 5 ZnO , 5 BaO , and 5 Pr_2O_3 in mol %) were investigated as functions of the laser power and write beam crossing angle. The same qualitative behavior as seen in the Eu^{3+} -doped glasses was observed. When the Pr^{3+} sample was illuminated by the write beams tuned to resonance with the ${}^3H_4-{}^3P_0$ absorption transition a

small signal was observed immediately, followed by a gradual build-up of signal intensity. The time required to reach the maximum LIG signal intensity is of the order of tens of seconds with the exact time depending on the laser power. If the laser write beams are not tuned in resonance with a Pr^{3+} absorption transition, no signal is observed. This demonstrates the significant enhancement of the nonlinear optical properties of the material which can be realized by resonantly pumping a rare earth ion absorption transition. When the write beams are blocked the LIG signal intensity initially decreased, not back to the baseline but rather to a value of approximately sixty percent of the maximum LIG signal where it remains indefinitely. This permanent signal can be erased by illuminating the grating with a single laser beam tuned to resonance with the same Pr^{3+} absorption transition used to write the grating. The erase time is of the order of tens of seconds with the exact time depending on laser power. As in the case of the Eu^{3+} sample this permanent signal can also be erased thermally.

Figure 7 displays the normalized intensity of the permanent and transient LIG signal as a function of the total write beam crossing angle, $2\Theta_A$. The numerical values for the experimental points are listed in Table I. It is seen that both the transient and permanent signals display the strongest intensity at the smallest write beam crossing angle which corresponds to the largest value of grating spacing. As the write beam crossing angle is increased, and the grating spacing decreases, the intensities of both the permanent and the transient signals decrease. This is typical behavior for FWM signals with the exact form depending on the coupling mechanism for the beams [14].

The build-up and erase times of the permanent LIG are displayed in Figs. 8 and 9. The values for the experimental points are listed in Table II. The scatter in the experimental values for the build-up and erase times suggests that there is no correlation between these times and the write beam crossing angle, however, more data needs to be acquired and analyzed before any definite conclusions are made. One thing to note though is that the build-up and erase times in the Pr^{3+} -doped glass are all of the order of seconds whereas in the Eu^{3+} -doped glass these time

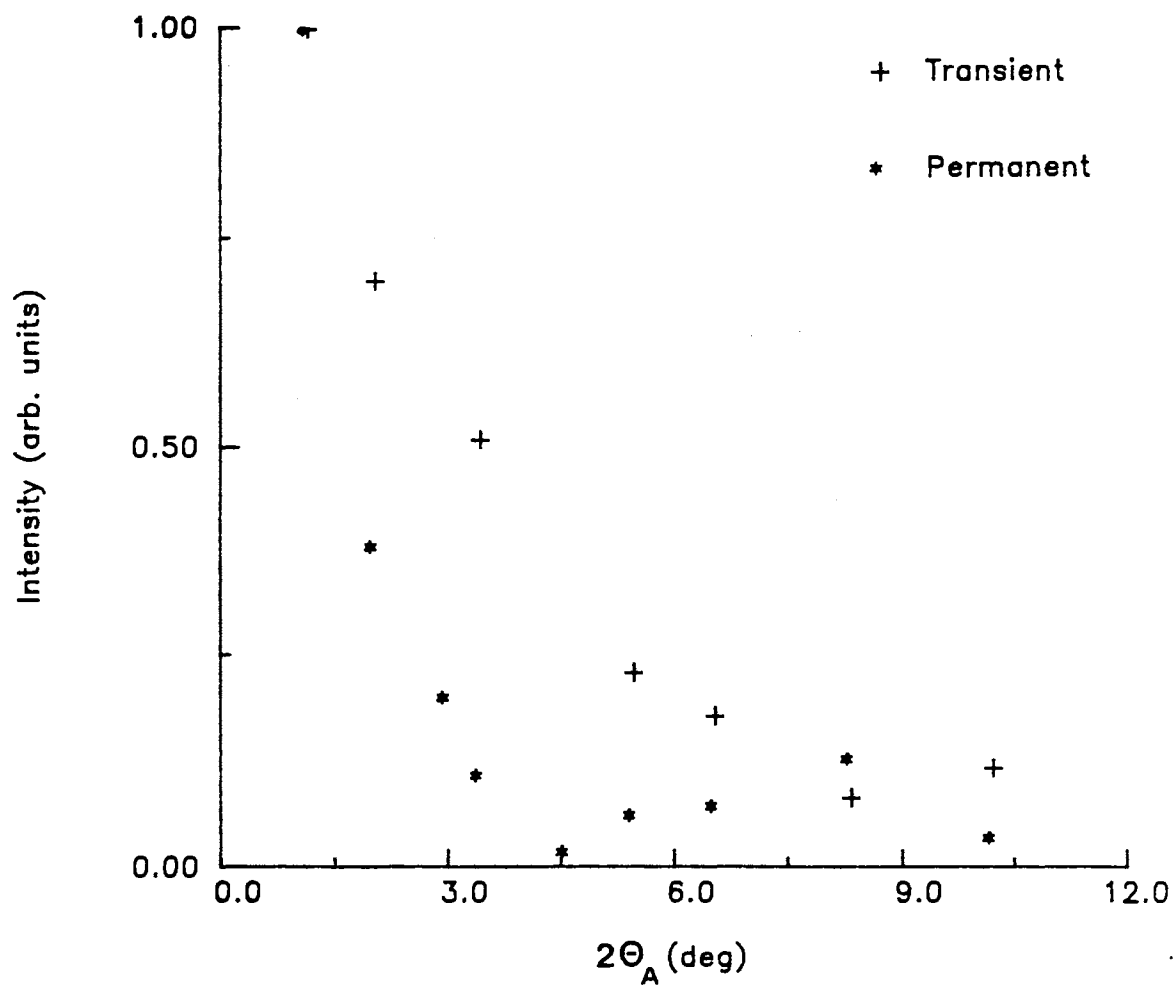


Figure 7. LIG Signal Intensity as a Function of Write Beam Crossing Angle $2\theta_A$ in Pr^{3+} Sample.

TABLE I
 LIG SIGNAL INTENSITY AS A FUNCTION
 OF WRITE BEAM CROSSING ANGLE
 $2\Theta_A$ IN Pr^{3+} SAMPLE

Intensity (arb. units)	$2\Theta_A$ (deg)
Permanent Signal	
1.000	1.10
0.380	1.99
0.200	2.95
0.110	3.39
0.019	4.53
0.063	5.42
0.074	6.50
0.130	8.28
0.036	10.16
Transient Signal	
1.000	1.10
0.700	1.99
0.510	3.39
0.230	5.42
0.180	6.50
0.084	8.28
0.120	10.16

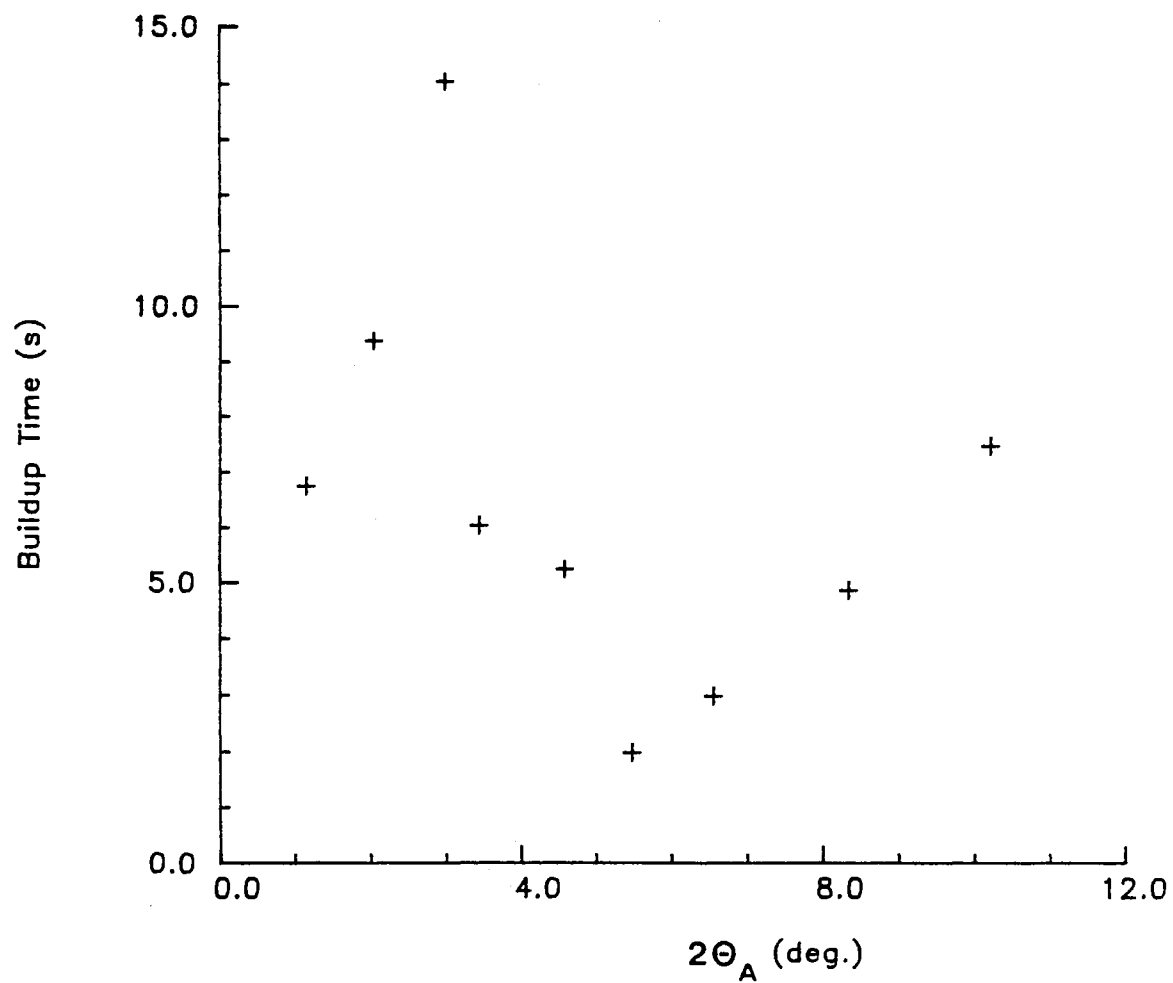


Figure 8. Build-Up Time of the Permanent LIG Signal as a Function of the Total Write Beam Crossing Angle $2\Theta_A$ in Pr^{3+} Sample.

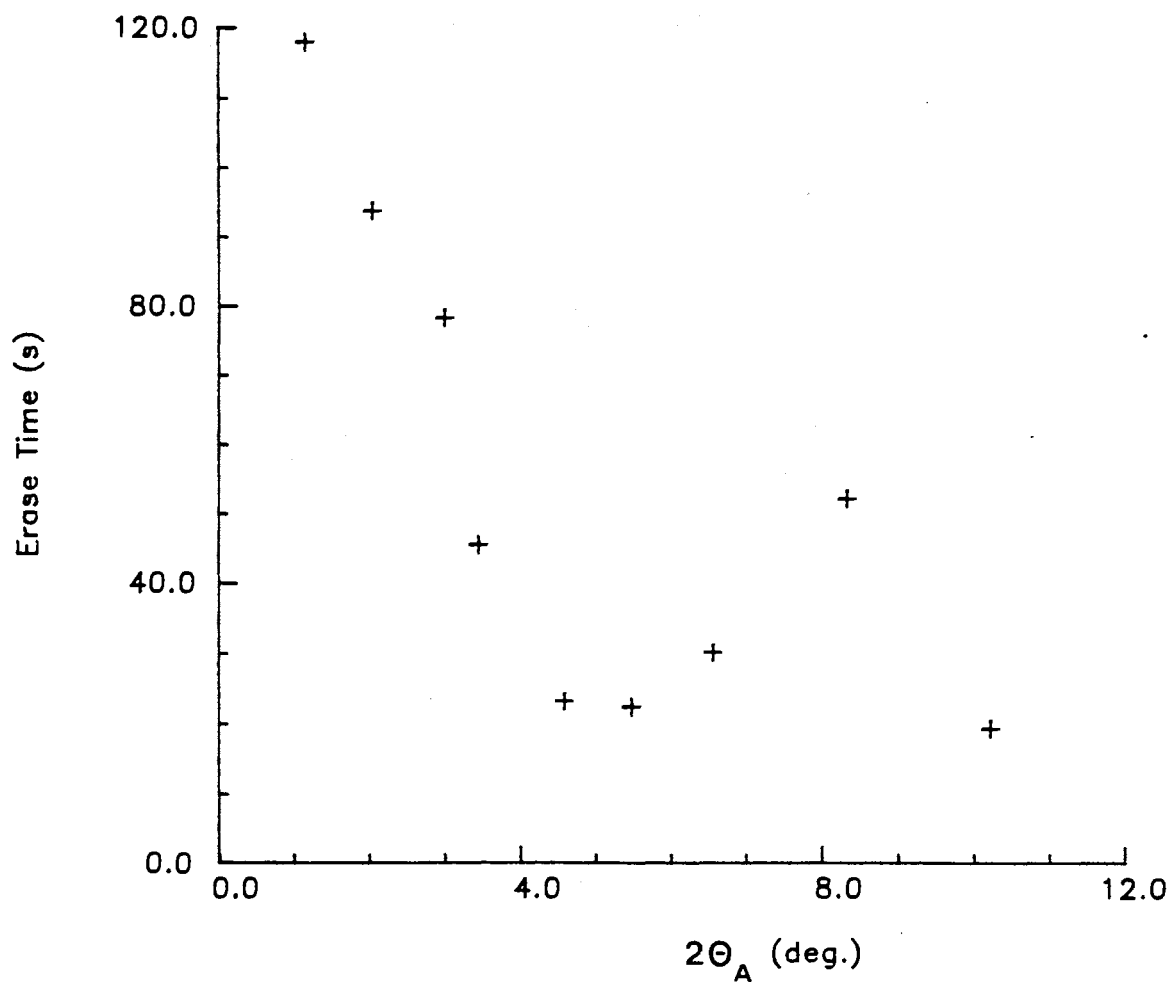


Figure 9. Erase Time of the Permanent LIG Signal as a Function of the Total Write Beam Crossing Angle $2\Theta_A$ in Pr^{3+} Sample.

TABLE II
 BUILD-UP AND ERASE TIMES OF THE
 PERMANENT LIG AS A FUNCTION
 OF THE TOTAL WRITE BEAM
 CROSSING ANGLE $2\theta_A$
 IN Pr^{3+} SAMPLE

Time (sec)	$2\theta_A$ (deg)
Build-up	
6.750	1.10
9.380	1.99
14.060	2.95
6.050	3.39
5.255	4.53
2.000	5.42
3.000	6.50
4.880	8.28
7.500	10.16
Erase	
118.13	1.10
93.75	1.99
78.38	2.95
45.75	3.39
23.25	4.53
22.50	5.42
30.37	6.50
52.50	8.28
19.50	10.16

scales were of the order of tens of minutes. This seems reasonable if the lifetimes of the excited states are considered as the source of this discrepancy. The lifetime of the 1D_2 metastable state in Pr^{3+} is roughly 100 times smaller than that of the 5D_0 metastable state in Eu^{3+} . Thus the Pr^{3+} ions will go through approximately 100 more cycles of being excited and relaxing to every one cycle for the Eu^{3+} ion. This will produce more phonons per unit time in the Pr^{3+} sample and will enhance the build-up and erase times. If the build-up time for the Pr^{3+} sample is taken to be 10 seconds and that for the Eu^{3+} sample to be 10 minutes, then a factor of 60 exists for the difference in the build-up times which is of the same order of magnitude as the difference in metastable lifetimes. Caution must be taken however in relying too heavily on this explanation as many other factors are involved in the formation and erasure of permanent LIGs including the availability of the proper phonon modes.

These LIG signal intensity and build-up and erase times were also measured for different values of the total power of the laser write beams. Figure 10 displays the normalized intensity of the permanent and transient signals as a function of the laser power and the numerical values are listed in Table III. As in the case of the Eu^{3+} -doped samples the transient signal intensity varies linearly with laser power and the permanent signal displays a quadratic behavior up to approximately 200 mW where saturation occurs. For superimposed transient and permanent gratings the FWM signal intensity is given by [8, 9]

$$I_S \propto |\Delta n_T|^2 e^{-\frac{2t}{\tau}} + 2 |\Delta n_T| |\Delta n_P| e^{-\frac{t}{\tau}} + |\Delta n_P|^2 \quad (13)$$

where Δn_T and Δn_P are the changes in the index of refraction due to the transient and permanent gratings, respectively, and $1/\tau$ is the fluorescence decay rate. Equation 13 predicts that the intensity of the transient component of the FWM signal varies linearly with laser power and that the intensity of the permanent component varies quadratically with laser power. This is precisely what is observed in Fig. 10. The measurements of the transient and permanent signal intensities took

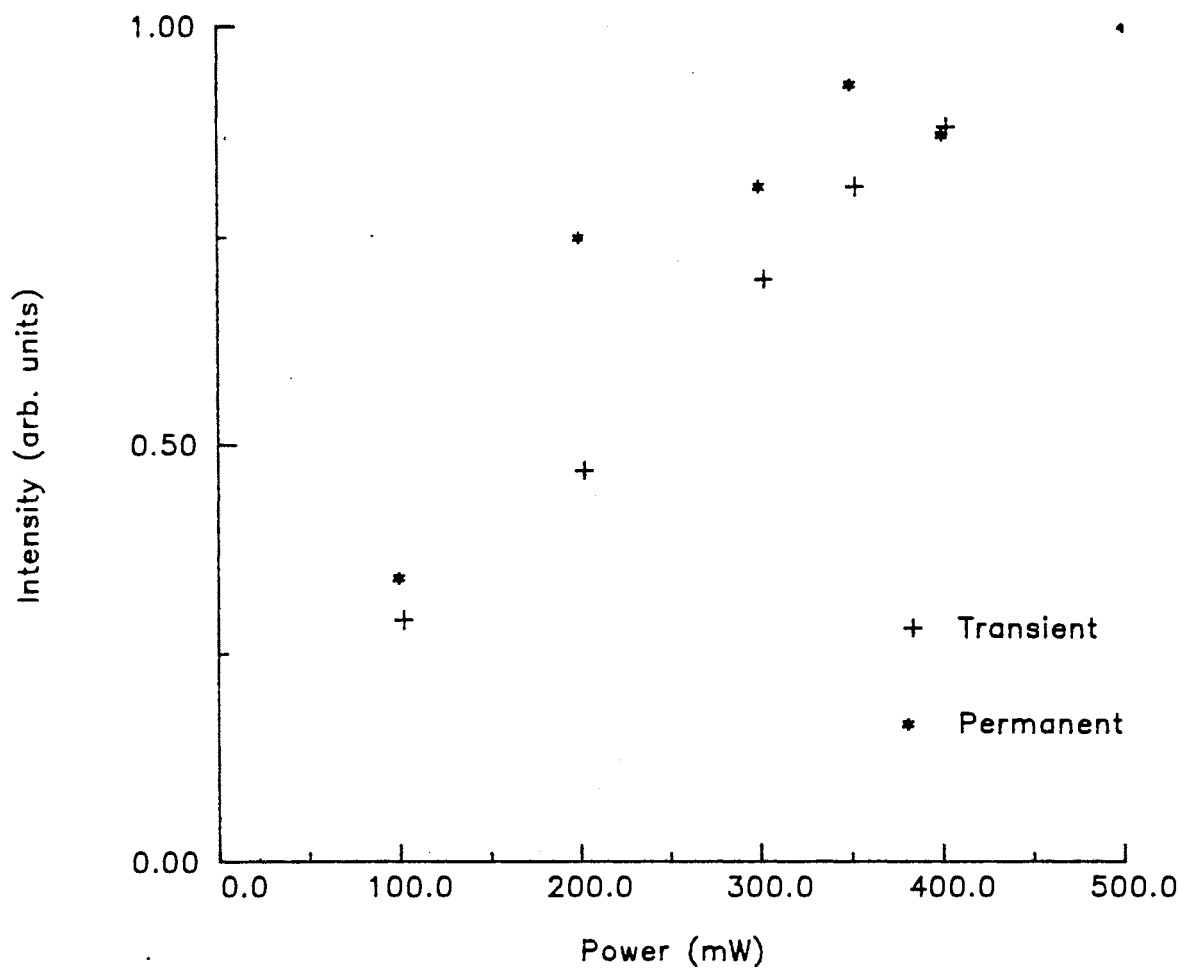


Figure 10. LIG Signal Intensity as a Function of the Total Laser Write Beam Power in Pr³⁺ Sample.

TABLE III
LIG SIGNAL INTENSITY AS A FUNCTION OF
THE TOTAL LASER WRITE BEAM
POWER IN Pr³⁺ SAMPLE

Intensity (arb. units)	Power (mW)
Transient	
1.00	500
0.88	400
0.81	350
0.70	300
0.47	200
0.29	100
Permanent	
1.00	500
0.87	400
0.93	350
0.81	300
0.75	200
0.34	100

place after the permanent signal had reached its maximum value. Thus the measured variation of the transient grating signal intensity may be associated with the presence of a strong permanent grating. The observed saturation in the permanent signal shows that there is a limit to the structural modification of the glass.

The build-up and erase times of the permanent grating as a function of laser write beam power are displayed in Figs. 11 and 12 and the numerical values are given in Table IV. It is seen that as the laser power is increased both the erase time and the build-up time decrease. The erase time decreases linearly as the laser power is increased but the build-up time decreases almost exponentially with increasing laser power. However, the general trend in both cases of decreasing times with increasing power is consistent with the model proposed previously.

The final measurement performed on the Pr^{3+} sample was to measure the temperature dependence of the permanent LIG. It was found that the signal displayed an arrhenius type of behavior with a measured activation energy of $2.825 \times 10^3 \text{ cm}^{-1}$. This is comparable to that seen in Eu^{3+} -doped glasses which are reported below.

The fact that permanent LIGs were seen only in samples doped with Eu^{3+} and Pr^{3+} can be attributed to the differences in the radiationless decay processes of these ions. It is well known that radiationless decay processes in rare earth ions take place by the emission of the appropriate number of the highest energy phonons available in the host material needed to cross the energy gap between the initial and final states [15]. (The term "phonon" is not technically correct for the vibrational modes of a glass. However, here the use of the term "phonon" will refer to any vibrational mode including local modes.)

Figure 13 displays the partial energy level diagrams for Eu^{3+} , Pr^{3+} , Nd^{3+} , and Er^{3+} . In forming the permanent LIG in the Pr^{3+} -doped glass sample the Pr^{3+} is excited from the $^3\text{H}_4$ ground state to the $^3\text{P}_0$ excited state. Figure 14 displays the room temperature fluorescence of the Pr^{3+} -doped glass sample after excitation by the 4880 Å line of the argon laser. This corresponds to exciting the Pr^{3+} ion from the $^3\text{H}_4$ ground state into the $^3\text{P}_0$ excited state. This spectrum displays a

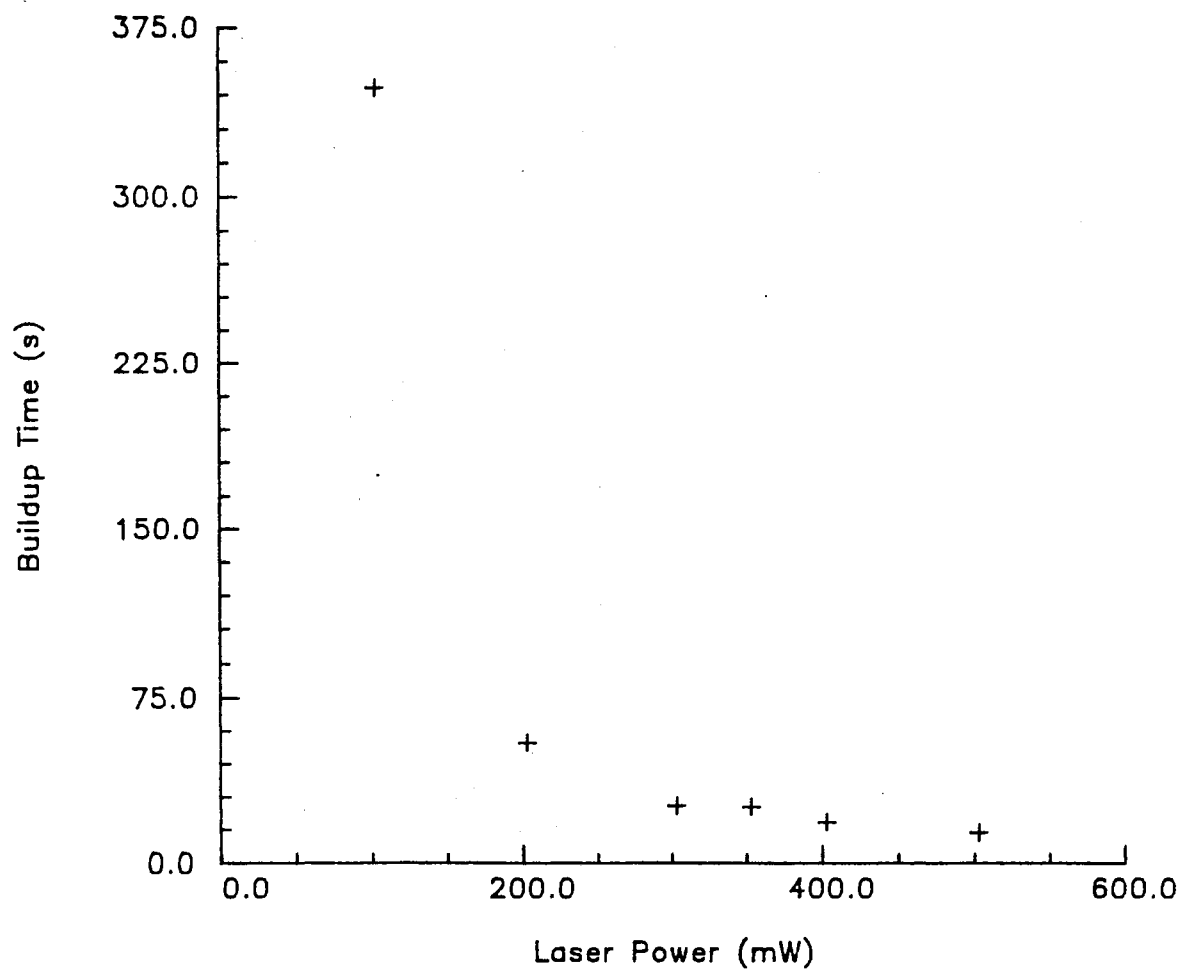


Figure 11. Build-Up Time of the Permanent LIG as a Function of the Total Laser Write Beam Power in Pr^{3+} Sample.

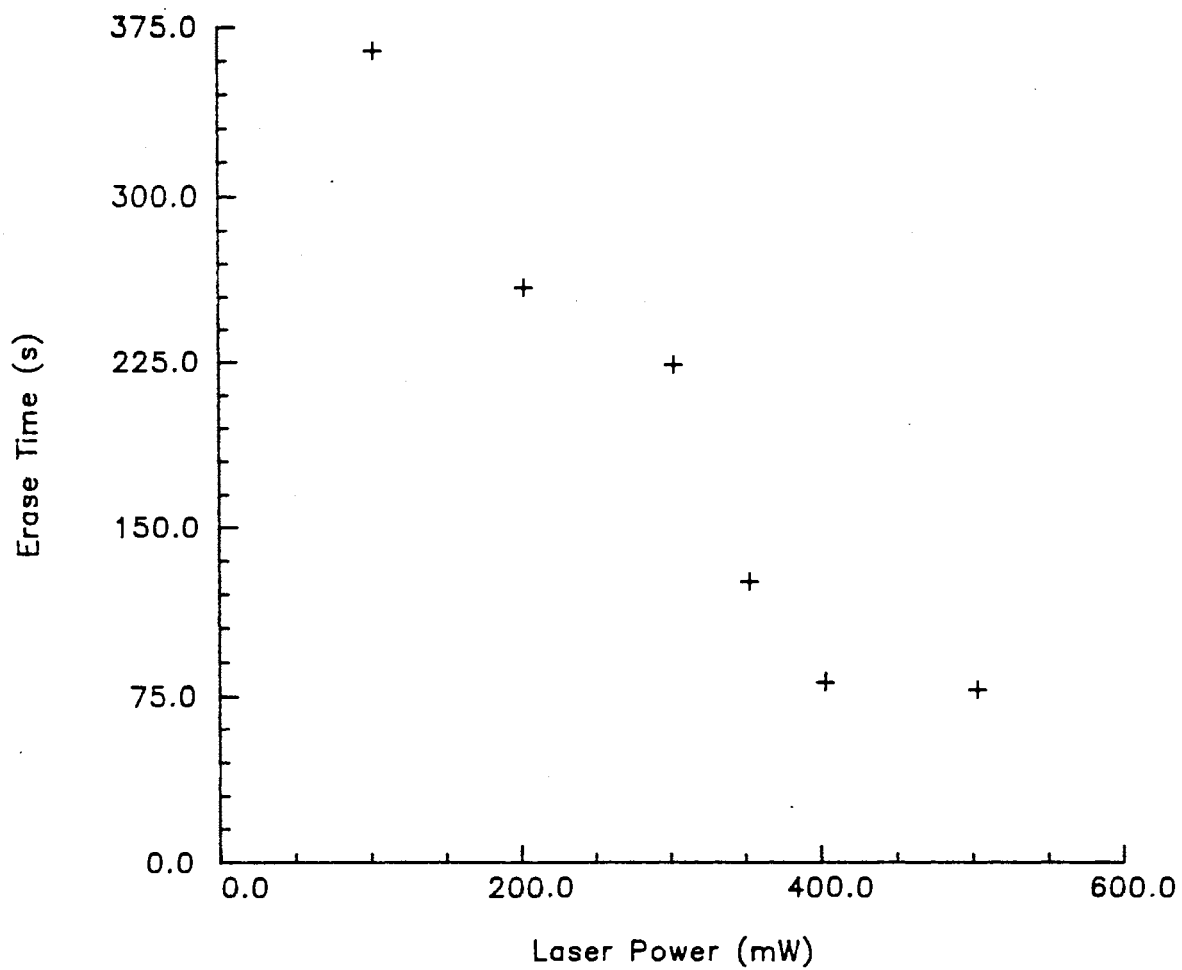


Figure 12. Erase Time of the Permanent LIG as a Function of the Total Laser Write Beam Power in Pr^{3+} Sample.

TABLE IV
BUILD-UP AND ERASE TIME OF THE
PERMANENT LIG AS A FUNCTION OF
THE TOTAL LASER WRITE BEAM
POWER IN Pr³⁺ SAMPLE

Time (sec)	Power (mW)
Build-up	
14.06	500
18.75	400
25.88	350
26.25	300
55.13	200
348.75	100
Erase	
78.38	500
81.75	400
126.00	350
223.88	300
259.50	200
364.88	100

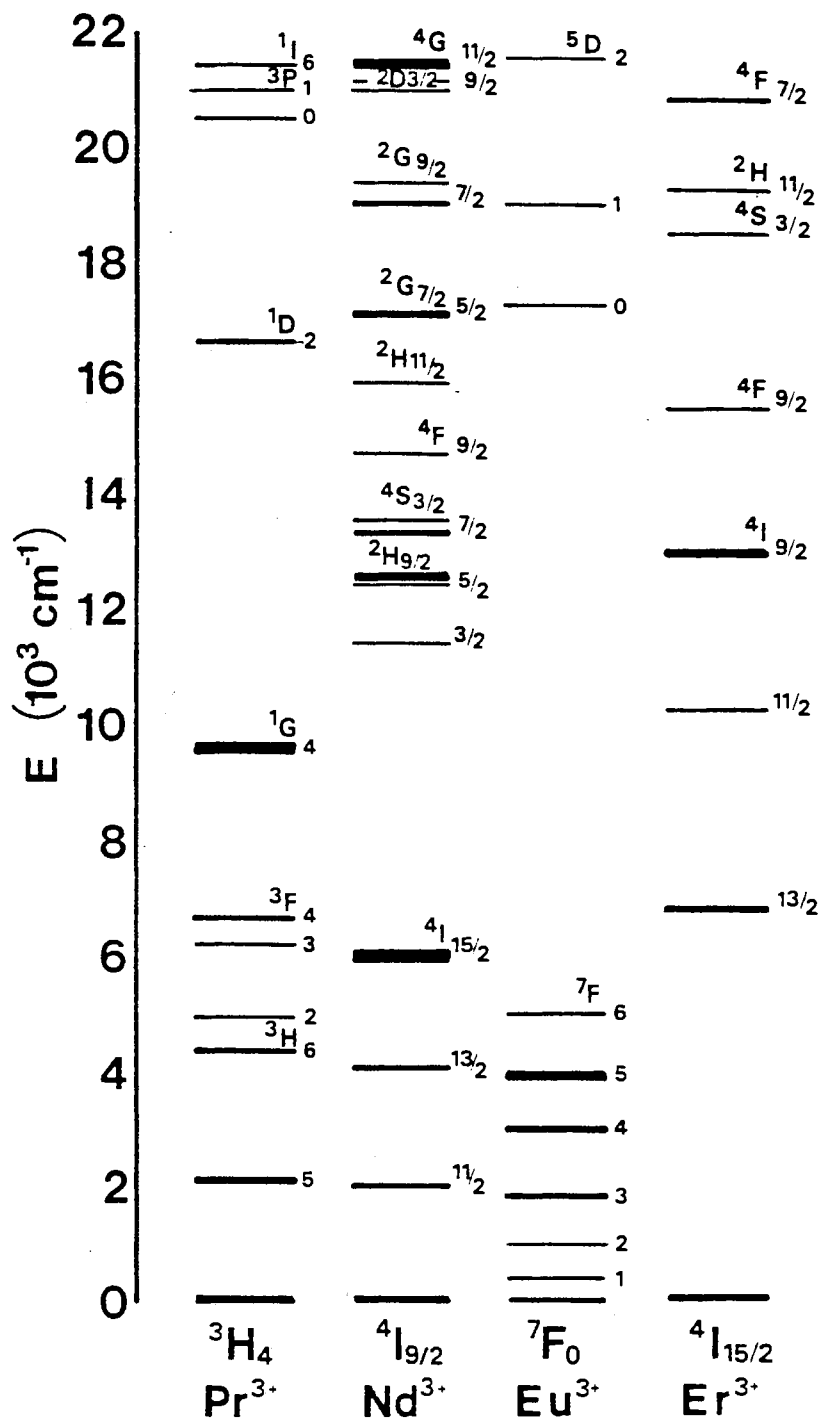


Figure 13. Partial Energy Level Diagram for Several Trivalent Rare Earth Ions.

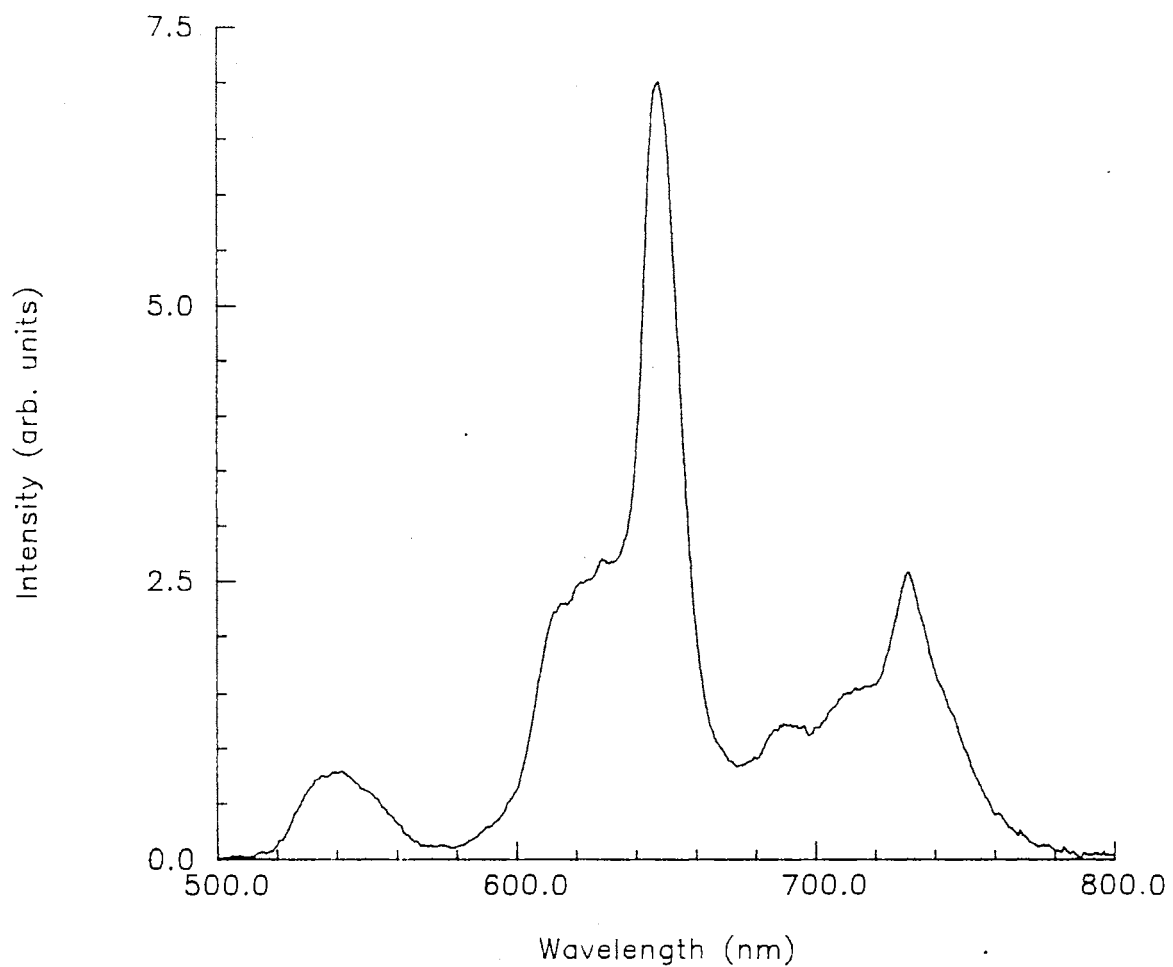


Figure 14. Room Temperature Fluorescence of the Pr³⁺-Doped Glass Sample after Excitation into the ³P₀ Excited State.

large peak at 645 nm which corresponds to the 3P_0 - 3F_2 radiative transition and two other peaks, one at 520 nm and another at 730 nm, which also correspond to radiative transitions for the 3P_0 level. Thus a large amount of the relaxation occurs radiatively without the emission of any phonons. However, there is a broad shoulder at 610 nm which corresponds to the 1D_2 - 3H_4 transition and another at 710 nm which corresponds to the 1D_2 - 3H_5 radiative transition. This shows there is some nonradiative relaxation taking place between the 3P_0 level and the 1D_2 level which results in phonons with energies of the order of 1000 cm^{-1} being emitted and will produce the structural modification needed to form the permanent LIG.

The same corresponding behavior is observed in a Eu^{3+} -doped silicate glass sample (70 SiO_2 , 15 Na_2O , 5 ZnO , 5 BaO , 5 Eu_2O_3 in mol %). Upon excitation from the 7F_0 ground state to the 5D_2 excited state the Eu^{3+} ion relaxes radiatively back to the 7F ground state manifold, however, there is a significant amount of fluorescence occurring from the 5D_0 level. This establishes the presence of high energy phonons which are produced from nonradiative relaxation from the 5D_J levels above 5D_0 and allows for the formation of the permanent LIG.

In the case of the Nd^{3+} -doped glass sample ($\text{NdP}_5\text{O}_{14}$) the Nd^{3+} ion is excited from the ${}^4I_{9/2}$ ground state to the ${}^4G_{9/2}$ excited state. Relaxation occurs through the emission of phonons, however in the Nd^{3+} ion the energy levels are much closer than in the Eu^{3+} or Pr^{3+} ions. Thus when the Nd^{3+} ion relaxes the phonons emitted are of much lower energy than those from Eu^{3+} or Pr^{3+} and as a result no permanent LIG is formed.

The final sample which is a silicate glass doped with Er^{3+} (70 SiO_2 , 15 Na_2O , 5 ZnO , 5 BaO , 5 Er_2O_3 in mol %) is an interesting case. In Fig. 13 it is seen that overall the spacing between the energy levels is much greater than in Nd^{3+} but not quite as large as in Eu^{3+} or Pr^{3+} . Write beam wavelengths of 4880 Å and 5145 Å which correspond to absorption transitions of the Er^{3+} ion from the ${}^4I_{15/2}$ ground state to the ${}^4F_{7/2}$ and ${}^2H_{11/2}$ excited state, respectively, were utilized in an attempt to create a permanent LIG in this sample. Under both excitation conditions no grating was observed. The explanation for this is

found in the fluorescence spectrum of the Er^{3+} sample obtained using the 4880 Å wavelength as the excitation source and is displayed in Fig. 15. Two large peaks are observed around 540 nm which corresponds to a radiative transition from the $^2\text{H}_{11/2}$ and $^4\text{S}_{3/2}$ excited states to the $^4\text{I}_{15/2}$ ground state. This shows that the Er^{3+} ion relaxes nonradiatively from the $^4\text{F}_{7/2}$ level down to the $^2\text{H}_{11/2}$ and $^4\text{S}_{3/2}$ levels by the emission of phonons before relaxing radiatively to the ground state. These phonons have small energies, comparable to those in the Nd^{3+} sample, which are insufficient to create the changes necessary to produce a permanent LIG. Notice there is a broad peak at 630 nm which corresponds to a radiative transition from the $^4\text{F}_{9/2}$ excited state to the ground state. For the Er^{3+} ions to relax nonradiatively from the $^4\text{S}_{3/2}$ level to the $^4\text{F}_{9/2}$ level they must cross an energy gap comparable to those seen in the Eu^{3+} and Pr^{3+} samples which suggests the existence of high energy phonons. However, from the size of the fluorescence peak it appears that there are very few of these phonons available for the formation of the permanent LIG.

Thus it is found that even though the same total heat energy is generated in each of the four samples, it is associated with very different types of vibrational modes. To demonstrate the effects of different types of vibrational modes, thermal lensing measurements were conducted [16]. Phosphate glasses containing either Eu^{3+} ($\text{EuP}_5\text{O}_{14}$), which will be referred to as EP, or Nd^{3+} ($\text{NdP}_5\text{O}_{14}$), which will be referred to as NP, along with one Nd^{3+} -doped silicate glass, which will be referred to as ED2, were studied.

The spatial pattern of the transmitted probe beam was observed on a screen for different experimental conditions. At low excitation power the results were qualitatively similar for all three materials with each excitation wavelength. With the samples placed just before the beam waist of the probe beam, the transmitted probe beam profile was expanded when the excitation beam was turned on. With the samples placed just after the probe beam waist, the transmitted probe beam profile contracted when the excitation beam was turned on. These observations indicate that the excitation beam causes the sample to act as a positive lens.

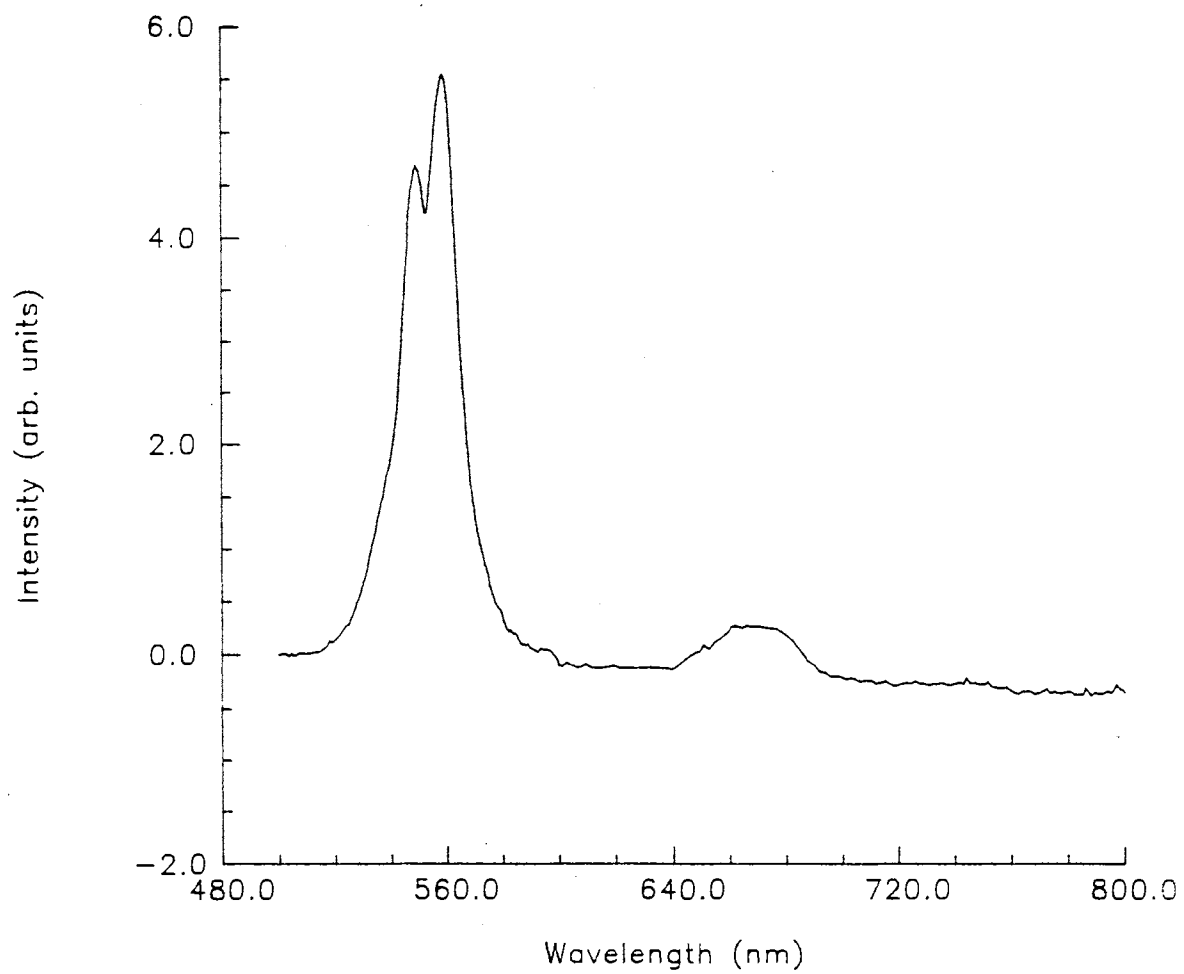


Figure 15. Room Temperature Fluorescence of the Er³⁺-Doped Glass Sample after Excitation into the ⁴F_{7/2} Excited State.

The magnitude of the change in the beam profile depends on the wavelength and power of the excitation beam as well as on the exact position of the sample relative to the beam waist of the probe beam. Figure 16 displays qualitatively the probe beam profile as the power of the excitation beam is increased for the NP glass. The wavelength of the excitation beam is 5145 Å. At relatively low excitation beam power the probe beam profile is a solid circle which expands as the excitation beam power is increased. Around an excitation beam power of 275 mW the probe beam profile begins to take the shape of a doughnut. This doughnut shape persists up to the maximum excitation beam power investigated of 530 mW. This type of behavior was also observed in the EP glass. In contrast, Fig. 17 displays the results of the same experiment performed on the Nd³⁺-doped ED2 silicate sample. Again with an excitation beam wavelength of 5145 Å at low powers the probe beam profile is that of a solid circle. The solid circle expands as the excitation beam power is increased as in the case of the phosphate glass, however, at approximately 370 mW the solid circle begins to split into two solid circles one above the other. This process continues as the excitation beam power is increased until at 1250 mW the probe beam profile has broken into two separate solid circles. The difference in probe beam profiles for the phosphate and silicate glasses is under investigation at this time.

The temporal variation of the observed changes in the probe beam pattern provides useful information for understanding the mechanism of the laser-induced refractive index change. A typical time evolution of the intensity in the center of the transmitted probe beam after turning on the excitation beam is shown in Fig. 18. For the NP sample, tens of milliseconds are required for the signal to reach equilibrium after the excitation laser is turned on, and a slightly longer time is required for the signal to decay to its initial level after the excitation laser is turned off. These results apply to both on- and off-resonance excitation. Similar results are obtained for off-resonance excitation of the EP sample. However, for resonance excitation of the ⁷F₀-⁵D₂ transition of the Eu³⁺ in the EP sample, an additional effect is observed. After turning on the excitation beam, the signal keeps

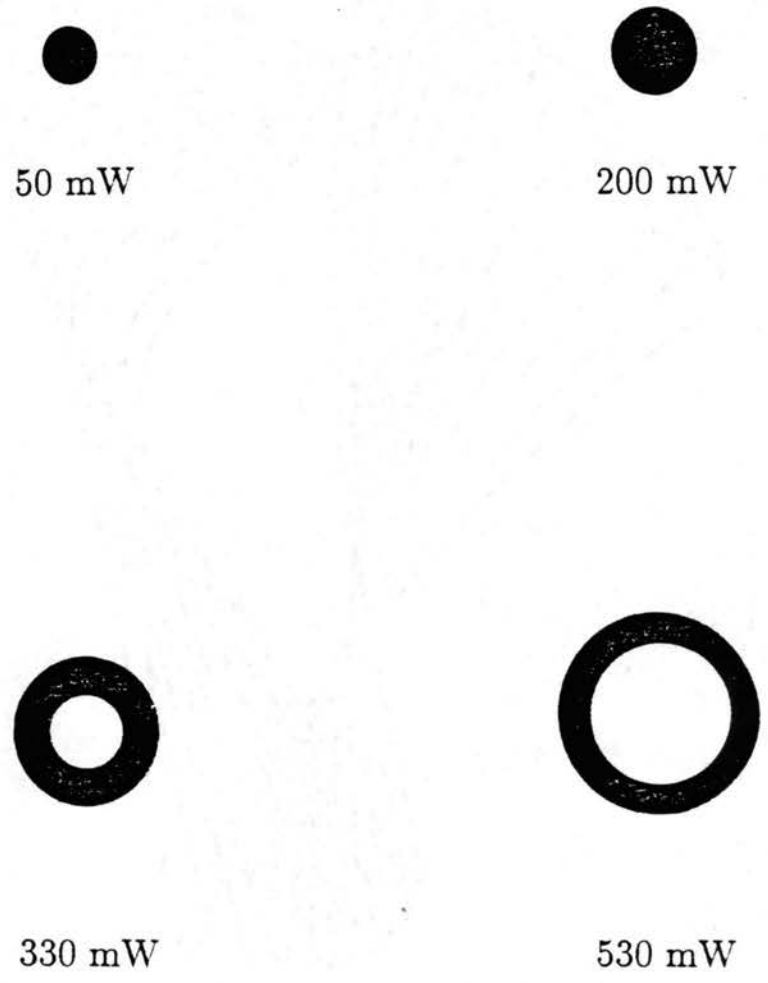
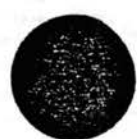


Figure 16. Spatial Profile of Transmitted Probe Beam as a Function of Excitation Beam Power in NP.



37 mW



370 mW



1050 mW



1250 mW

Figure 17. Spatial Profile of Transmitted Probe Beam as a Function of Excitation Beam Power in ED2 Silicate Glass.

decreasing for several minutes as shown in Fig. 19. When the excitation beam is turned off again, the signal does not return to its original level. This characteristic shows the creation of a permanent change in the refractive index and disappears when the sample is heated to temperatures above approximately 380 K.

The results just described are useful in understanding the properties of laser-induced refractive index changes in this type of material. The refractive index change can be associated with several types of physical mechanisms such as thermal lensing [17, 18], electrostriction [18], the Kerr effect [18], and resonant self-focusing [19]. The last three mechanisms are directly related to the atomic properties of the sample and have response times on the order of nanoseconds or less. The first mechanism is related to the microstructure of the sample and has a much slower response time. The general characteristics and response times observed in these experiments indicate that thermal lensing is the mechanism dominating the laser-induced refractive index changes in these samples. The results of previous experiments based on damage threshold measurements involving much higher laser powers indicated that the Kerr effect was more important than thermal lensing under these conditions [18]. The results here show that thermal lensing is predominant in these absorbing glasses at medium power levels (10^4 – 10^6 W cm⁻²).

Thermal lensing is a well-known phenomenon in liquids and gases [20] and has been used to investigate different spectroscopic properties of weakly absorbing media [21, 22]. An expression for the focal length of a thermal lens has been derived previously using the assumption of Gaussian-beam profiles [17, 22]. The heat generated at a radius r is proportional to the square of the electric field at this position:

$$Q(r) = PA \exp(-2r^2/w^2) \quad (14)$$

where P is the power in the incident excitation beam, A is the absorbance of the sample at the wavelength of the excitation beam, and w is the excitation-beam radius inside the sample. The temperature rise at this position at time t for one unit heat source at radial position r' is

$$G(r, r', t) = (4\pi kt)^{-1} \exp[-(r^2 + r'^2)/(4Dt)] I_0(rr'/2Dt) \quad (15)$$

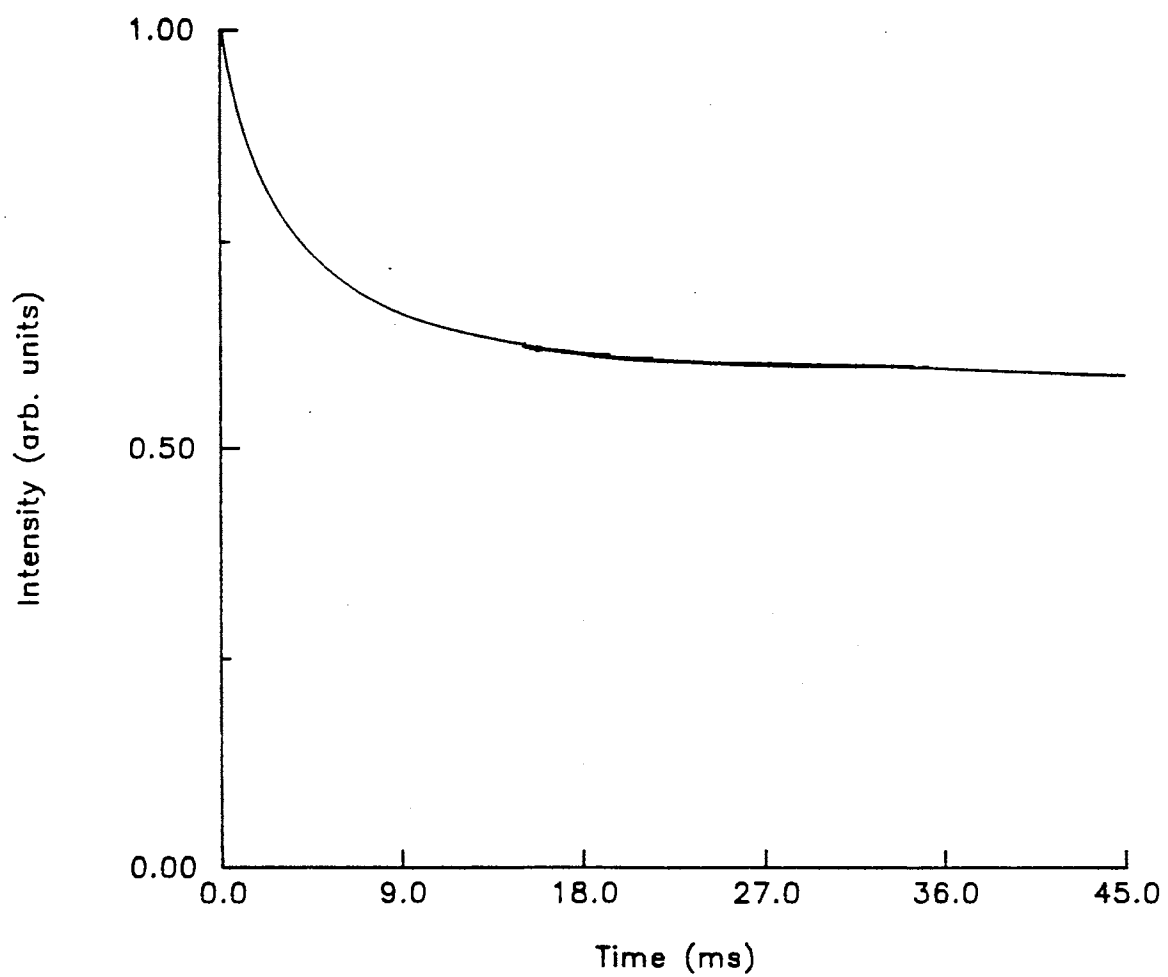


Figure 18. Time Evolution of the Intensity at the Center of the Transmitted Probe Beam for the NP Sample.

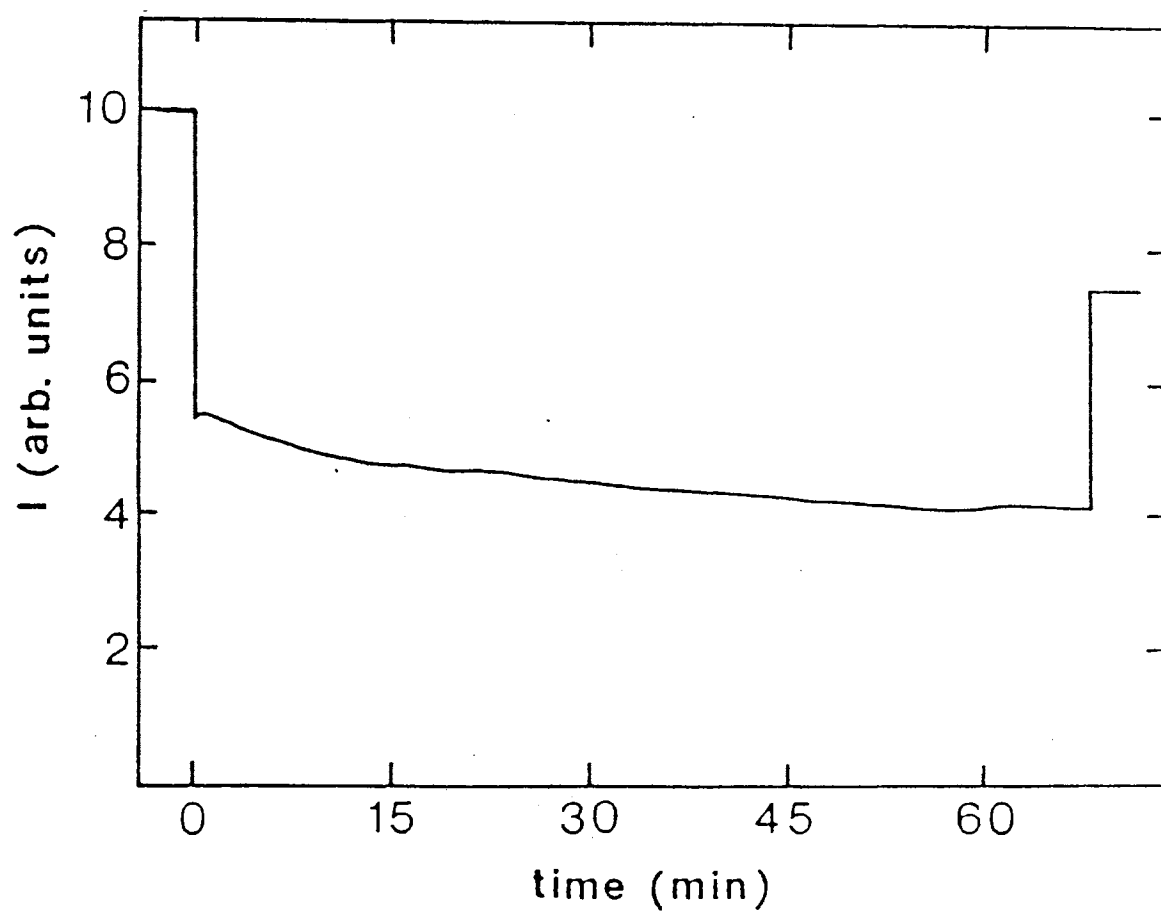


Figure 19. Time Evolution of the Intensity at the Center of the Transmitted Probe Beam for the EP Sample.

where I_0 is a modified Bessel function, k is the thermal conductivity (in units of cal $\text{cm}^{-1} \text{sec}^{-1} \text{ }^\circ\text{C}^{-1}$), and D is the thermal diffusivity (in units of $\text{cm}^2 \text{sec}^{-1}$). The latter is given by

$$D = \frac{k}{\rho C_\rho} \quad (16)$$

where ρ is the density and C_ρ is the specific heat. The rise in the temperature at position r and time t is then

$$\Delta T(r, t) = \int_0^\infty \int_0^t Q(r') G(r, r', t) dr' dt. \quad (17)$$

This temperature rise produces a change in the refractive index given by

$$n(r, t) = n_0 + (dn/dt)\Delta T(r, t). \quad (18)$$

Near the axis, the temperature profile can be approximated by a parabola. This parabolic variation of the refractive index is equivalent to a thin lens. The corresponding focal length is given by

$$F(t) = f(\alpha)[1 + (t_c/2t)] \quad (19)$$

where

$$f(\alpha)^{-1} = 0.553PA/[(\pi k w^2)(dn/dT)] \quad (20)$$

and

$$t_c = w^2/4D. \quad (21)$$

Depending on the sign of dn/dt , the thermal lens will be either positive or negative. The thermal lens is usually negative for liquids and gasses and is usually positive in glasses [18], consistent with the results reported above.

The relative change in the intensity at the center of the transmitted probe beam can be determined from ray analysis by using transfer matrices and by assuming a Gaussian beam shape. For this experimental configuration,

$$I_0/I(t) = 1 + \Theta(1 + t_c/2t)^{-1} + \Theta^2[4(1 + t_c/2t)^2]^{-1}, \quad (22)$$

where

$$\Theta = 2(F_1 - d_1)d_2[(d_1 + d_2 - F_1)f(\alpha)]^{-1}. \quad (23)$$

In Eq. 23 F_1 is the focal length of the focusing lens, d_1 is the distance between the focusing lens and the sample, and d_2 is the distance between the sample and the screen. The parameter Θ is a dimensionless collection of variables and can be viewed as characterizing the strength of the thermal lens.

A computer fit of Eq. 22 to the experimental data can be obtained by treating Θ and t_c as adjustable parameters. An example of this type of fitting is shown in Fig. 20. Excellent agreement is obtained between theory and experimental results, and the values obtained for the adjustable parameters under different experimental conditions are listed in Table V. The nonresonant thermal lensing is due to the absorption from the network of the glass host, in these samples mainly the O^{2-} ions. In this case, the time behavior is governed by the thermal properties of the bulk sample, namely the heat-diffusion coefficient. The observed difference in the time constant t_c between the two samples reflects a difference in the thermal diffusivities of the materials. It is not totally surprising to observe a different thermal behavior for the two samples since Nd^{3+} and Eu^{3+} have somewhat different physical and chemical properties. In addition, when these two compounds are in the crystalline form they have different crystal structures, which implies that the short-range structure in the two glasses may be different.

For resonant excitation of the rare earth ions, the heat is generated through radiationless relaxation processes that produce local vibrational modes that then transfer their energy to the phonon modes of the glass network. The time constant of the thermal lensing is then governed both by the interaction between the rare earth ions and the phonons and by the propagation of the phonons. The difference in the mechanisms of generating the phonons is responsible for the difference in the thermal lensing time constant for resonant and nonresonant excitation. This difference is greater in the NP sample than in the EP sample. The Nd^{3+} ions will relax from the ${}^2G_{9/2}$ to the ${}^4F_{3/2}$ metastable state cascading between closely spaced intermediate electronic levels by the successive emission of several different phonons. The Eu^{3+} ions will relax from the 5D_2 level to the 5D_0 level by the

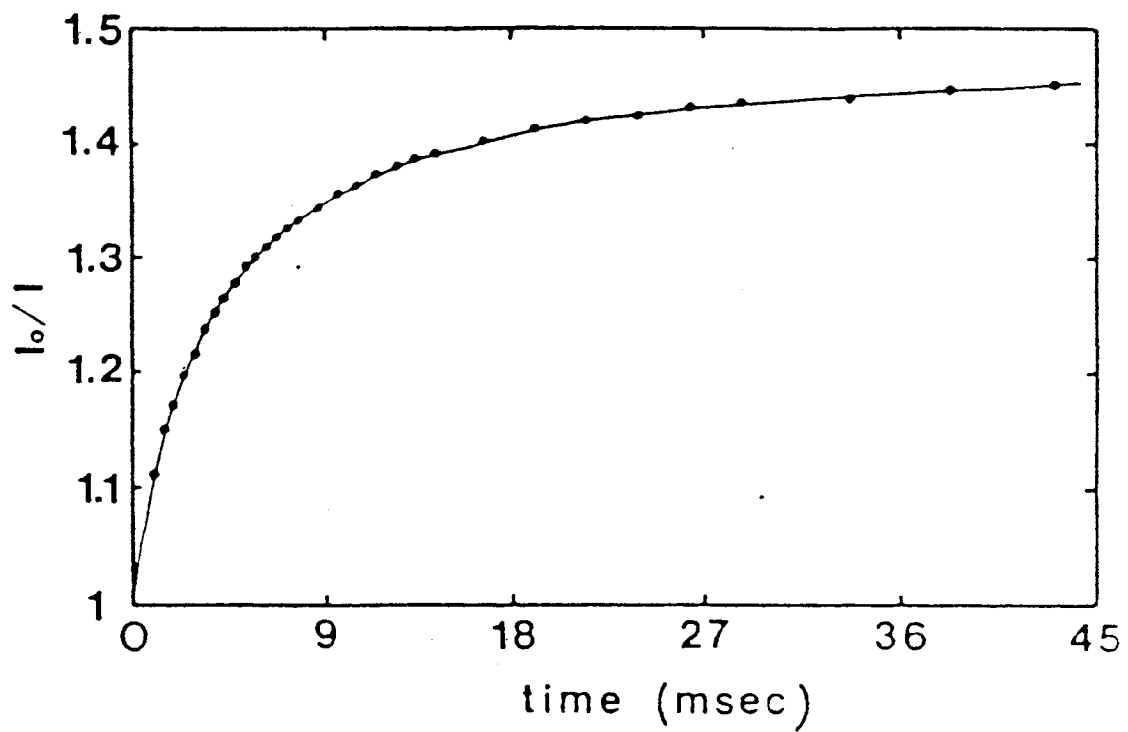


Figure 20. Theoretical Fit of the Time Evolution of the Signal in the NP Sample.

TABLE V
SUMMARY OF PARAMETERS FROM
THERMAL LENSING
EXPERIMENTS

Sample	λ (nm)	P (W)	A	Θ	t_c (msec)	Θ / PA (W ⁻¹)
EP	465.8	0.02	0.161	0.1078	2.63	33.480
	514.5	1.70	0.098	0.0781	3.11	0.468
NP	514.5	0.06	0.236	0.2840	2.76	20.060
	488.0	1.55	0.094	0.4410	6.46	3.027

emission of a few high-energy phonons [15]. These two different types of radiationless relaxation channels result in very different initial distributions of vibrational modes, which lead to different thermal lensing time constants.

From the results listed in Table V, the strengths of the thermal lenses can be compared. The absolute strengths cannot be determined because the fluorescence efficiencies are unknown. To eliminate the influence of differences in the absorbed power, the ratio Θ/PA was worked with,

$$\frac{(1/k_1)(dn/dT)_1}{(1/k_2)(dn/dT)_2} = \frac{\Theta_1 P_2 A_2}{\Theta_2 P_1 A_2}, \quad (24)$$

where the subscripts 1 and 2 refer to two different samples or experimental conditions. The results show the thermal lensing for the EP sample to be more than 71.5 times stronger for resonance excitation than for nonresonance excitation, whereas the difference is only about 6.6 for the NP sample. For on-resonance excitation, the thermal lensing is about 1.7 times stronger in EP than in NP, while for off-resonance excitation thermal lensing is about 6.5 times stronger in NP than in EP.

The same arguments just presented explain that the differences in the time constants for thermal lensing can be used to explain the differences in the strengths of the thermal lensing. For the nonresonant excitation, the strength of the thermal lensing is associated with the change of the polarizability of the glass network and mainly the O^{2-} ions. The glass network of the NP sample is much more sensitive to thermal effects than the EP sample because of the lower thermal conductivity. On the other hand, the strength of thermal lensing for the resonance excitation is associated with the change of the polarizability around the rare earth ions. Eu^{3+} is more sensitive to thermal effects than Nd^{3+} , owing to its strong coupling to localized high-energy phonons as observed in Raman scattering experiments [8, 9, 16].

Using Eqs. 20 and 22, the permanent change in the refractive index induced by the thermal lens effect can be calculated. When the excitation beam is focused down to about $20 \mu\text{m}$, the calculated value is $\Delta n = 1.23 \times 10^{-5}$, which

is on the same order as that produced in the four-wave mixing experiments with similar excitation power in the weakly focused, crossed excitation beams. The single focused beam in the sample is approximately the same size as the interfringe distance in crossed-beam experiments. This size similarity results in similar intensities and gradients of the electric fields in the two types of experiments, and thus similar changes in the refractive index should be expected.

The Er^{3+} -doped sample has also exhibited strong thermal lensing implying that the onset of thermal lensing inhibits the formation of the permanent LIGs. However, the Pr^{3+} -doped sample displays a slight amount of thermal lensing along with a permanent LIGs. This suggests that thermal lensing and permanent LIGs formation are competing processes which depend on the energy of the phonons being produced through nonradiative relaxation of the rare earth ion dopant.

To further establish the importance of radiationless relaxation in the excited state, an attempt was made to produce permanent LIGs by exciting the Eu^{3+} ion directly into the $^5\text{D}_0$ level instead of the $^5\text{D}_2$ level as was done previously. An argon-laser-pumped ring dye laser with R6G was used for these experiments. The laser power was set to achieve the same density of excited Eu^{3+} ions as obtained in the previous experiments in which permanent LIGs were formed. Several samples were investigated, including the europium pentaphosphate sample which exhibits strong permanent LIGs for $^5\text{D}_2$ excitation. No permanent LIGs were observed in any of the samples for $^5\text{D}_0$ excitation. This confirms the importance of having radiationless relaxation in the excited state to establish this type of grating.

To determine the importance of the rare earth ion concentration on the formation of the permanent LIGs, samples were obtained whose compositions varied only in the Eu^{3+} concentration. The first samples investigated were two Eu^{3+} -doped metaphosphate samples, one with a composition of 90 mole percent $\text{La}(\text{PO}_3)_3$, 10 mole percent Eu_2O_3 and the other with 50 mole percent $\text{La}(\text{PO}_3)_3$, 50 mole percent Eu_2O_3 . These are labeled MP10 and MP50, respectively.

Permanent LIGs were written in each sample at room temperature and the scattering efficiency of the gratings was measured. It was found that the permanent

LIG signal intensity of the MP50 sample was eight times stronger than that of the MP10 sample. This is consistent with the double minima potential well model discussed below.

One other set of samples was investigated along this line, a lithium borate glass, LB15, with composition 75 mole percent B_2O_3 , 10 mole percent Li_2O , and 15 mole percent Eu_2O_3 . It was possible to establish a permanent LIG in this sample whereas in a previously investigated lithium borate sample, LB1, with only 1 mole percent Eu_2O_3 no grating was created.

Additional experiments were performed on the europium pentaphosphate sample which exhibited strong permanent LIGs. For example, the effects of changing the polarization direction of the probe beam compared to the polarization directions of the write beams were investigated. No dependence of signal intensity on the probe beam polarization direction was observed. Also, a phosphate glass sample (52.3 P_2O_5 , 30.0 Li_2O , 10.0 Ca_2O , 4.7 Al_2O_3 , 3.0 Eu_2O_3 in mol %) was investigated which contained approximately the same concentration of europium as the lithium phosphate glass studied earlier but which had a mixture of Eu^{3+} and Eu^{2+} valence states. No permanent LIG was observed in this sample.

Thus, to create the type of permanent LIG described here, it is necessary to have a high concentration of rare earth ions that have a relatively large energy gap between excited electronic energy levels and this gap should be crossed by radiationless relaxation.

Properties of the Host Glass

Table VI lists the compositions of the Eu^{3+} -doped glasses that have been investigated for permanent grating formation. Phosphate, silicate, and borate glass hosts are found to produce gratings very efficiently while no gratings have been observed in the germanate and fluoride glasses that have been tested thus far.

All of the samples investigated had dimensions of roughly 2.0 cm wide by 2 mm thick by 1 cm high and were polished to optical quality on two parallel faces.

TABLE VI
SAMPLE COMPOSITIONS

Sample	Network Former	Network Modifier	Eu Content	Permanent Grating
EP	83.3 P ₂ O ₅		16.7 Eu ₂ O ₃	YES
LP3	52.3 P ₂ O ₅	30.0 Li ₂ O 10.0 CaO 4.7 Al ₂ O ₃	3.0 Eu ₂ O ₃	YES
MP10	90.0 La(PO ₃) ₃		10.0 Eu(PO ₃) ₃	YES
MP50	50.0 La(PO ₃) ₃		50.0 Eu(PO ₃) ₃	YES
NS3	72.0 SiO ₂	15.0 Na ₂ O 5.0 BaO 5.0 ZnO	3.0 Eu ₂ O ₃	YES
LS3	57.0 SiO ₂	27.5 Li ₂ O 10.0 CaO 2.5 Al ₂ O ₃	3.0 Eu ₂ O ₃	NO
LB15	75.0 B ₂ O ₃	10.0 Li ₂ O	15.0 Eu ₂ O ₃	YES
LB1	59.0 B ₂ O ₃	40.0 Li ₂ O	1.0 Eu ₂ O ₃	NO
ZF5	53.0 ZrF ₄	13.7 BaF ₃ 5.5 LaF ₃ 3.6 AlF ₃ 19.2 NaF	5.0 EuF ₃	NO

TABLE VI (Continued)

Sample	Network Former		Network Modifier		Eu Content		Permanent Grating
CLAP	36.1	PbF ₂	26.1	CdF ₂	5.0	EuF ₃	NO
			27.1	AlF ₃			
			4.7	LiF			
LS5	70.0	SiO ₂	15.0	Li ₂ O	5.0	Eu ₂ O ₃	YES
			5.0	BaO			
			5.0	ZnO			
NS5	70.0	SiO ₂	15.0	Na ₂ O	5.0	Eu ₂ O ₃	YES
			5.0	BaO			
			5.0	ZnO			
KS5	70.0	SiO ₂	15.0	K ₂ O	5.0	Eu ₂ O ₃	YES
			5.0	BaO			
			5.0	ZnO			
RS5	70.0	SiO ₂	15.0	Rb ₂ O	5.0	Eu ₂ O ₃	YES
			5.0	BaO			
			5.0	ZnO			
CS5	70.0	SiO ₂	15.0	Cs ₂ O	5.0	Eu ₂ O ₃	YES
			5.0	BaO			
			5.0	ZnO			

This is important in order to minimize surface scattering to ensure accurate values in the scattering efficiency measurements.

One important difference between some of these glasses is the number of metastable states. An Eu^{3+} -doped fluoride glass, BZLT(27 ZnF_4 , 19 BaF_2 , 26 LaF_3 , 27 ThF_4 , 1 EuF_3 in mole percent) showed a significant amount of fluorescence emission from the ${}^5\text{D}_J$ levels above ${}^5\text{D}_0$. This results in fewer ions relaxing nonradiatively from the ${}^5\text{D}_2$ and ${}^5\text{D}_1$ levels to the ${}^5\text{D}_0$ metastable state leading to a smaller number of high energy phonons being available for grating formation which inhibits the ability to form permanent gratings.

In contrast, it was found that in a fluorophosphate glass, FP (Schott FK-54), with 5 mole percent EuF_3 , it was possible to produce a permanent LIG. This suggests that the fluorophosphate glass contains enough of the characteristics of the phosphate glasses to allow formation of the permanent grating.

In order to investigate the vibrational modes involved in the writing of permanent gratings of this type, the Raman spectra and resonant Raman spectra for glasses which exhibited permanent LIGs with those of glasses in which no permanent LIGs could be produced were compared. Typical results are shown in Figs. 21-24. An argon laser was used as the source and an Instruments S. A. Ramanor U-1000 with computer-controlled data acquisition was used to record the spectra. The 5145 Å argon-laser line gives the normal Raman spectra shown by dashed lines in Figs. 21-24, while the 4727 Å laser line is close to the ${}^7\text{F}_0$ - ${}^5\text{D}_2$ Eu^{3+} transition and therefore produces resonant Raman scattering. The solid lines in the figures show the latter type of spectra.

The disordered structure of glasses causes the network vibrations to have a short coherence length compared to the optical wavelength. This causes a breakdown of the wave-vector selection rule which is present for glasses which are directly related to the vibrational density of states [23]. In addition, the vibrational modes of a glass are more localized than those of a crystal due to the lack of translational

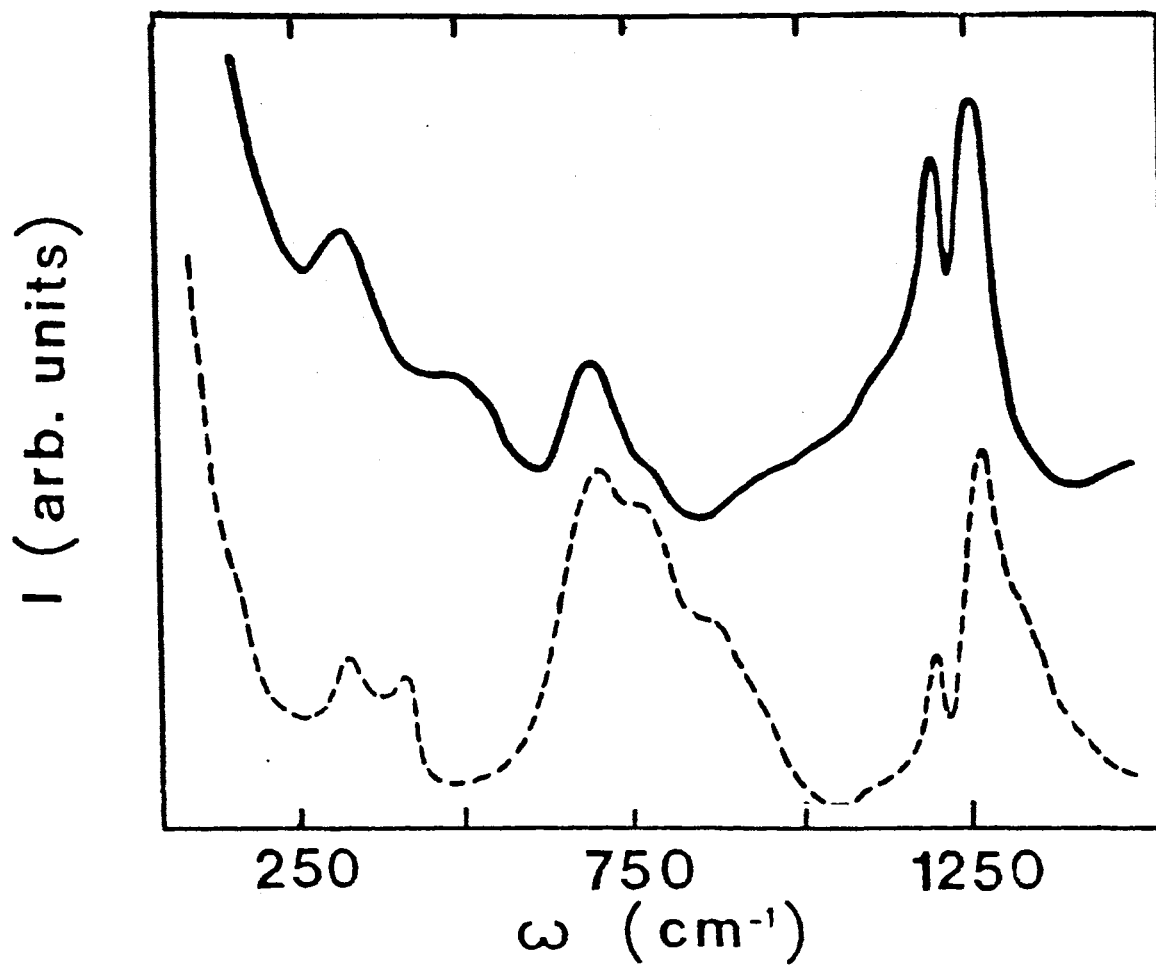


Figure 21. Raman Spectra (Dashed Line) and Resonant Raman Spectra (Solid Line) of Europium Pentaphosphate Glass.

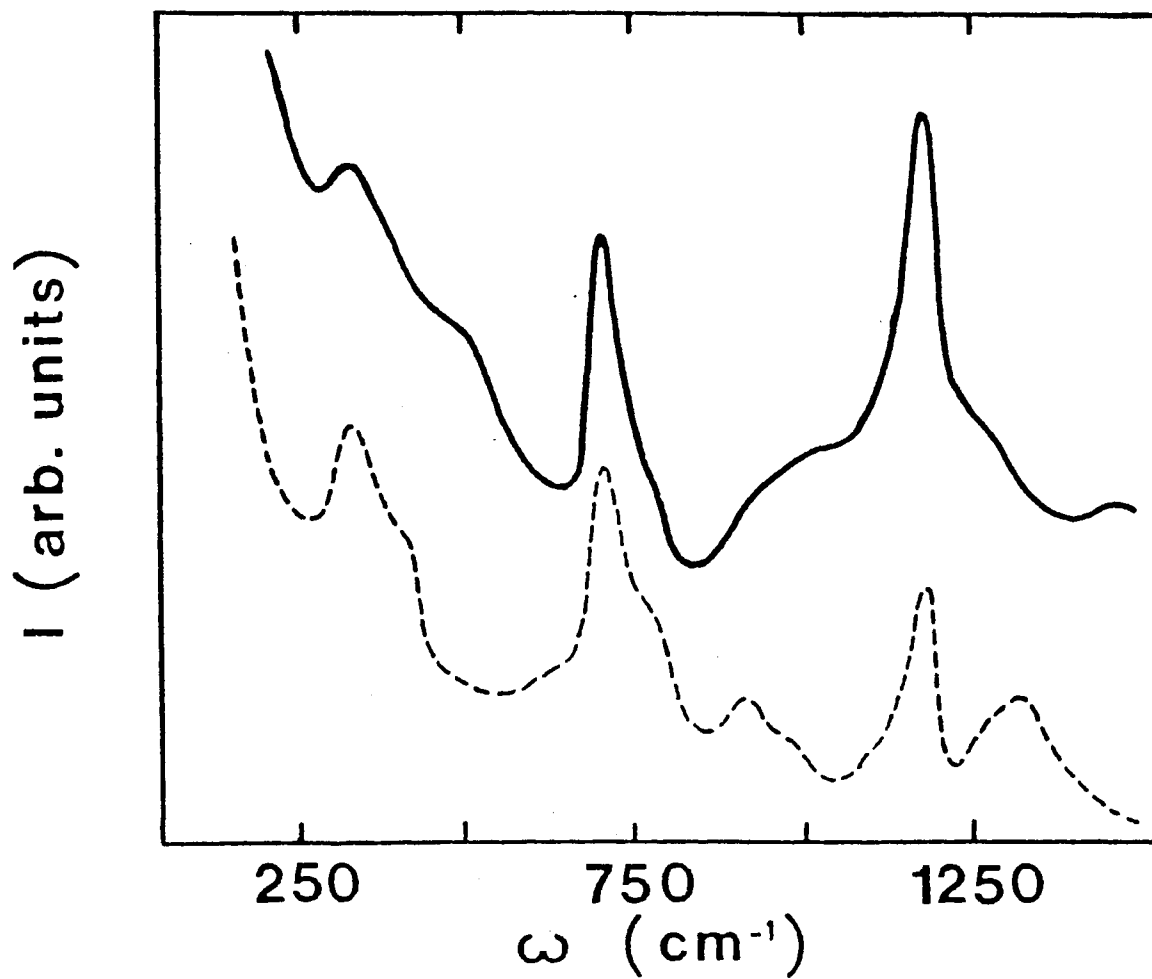


Figure 22. Raman Spectra (Dashed Line) and Resonant Raman Spectra (Solid Line) of Eu^{3+} -Doped Lithium Phosphate Glass.

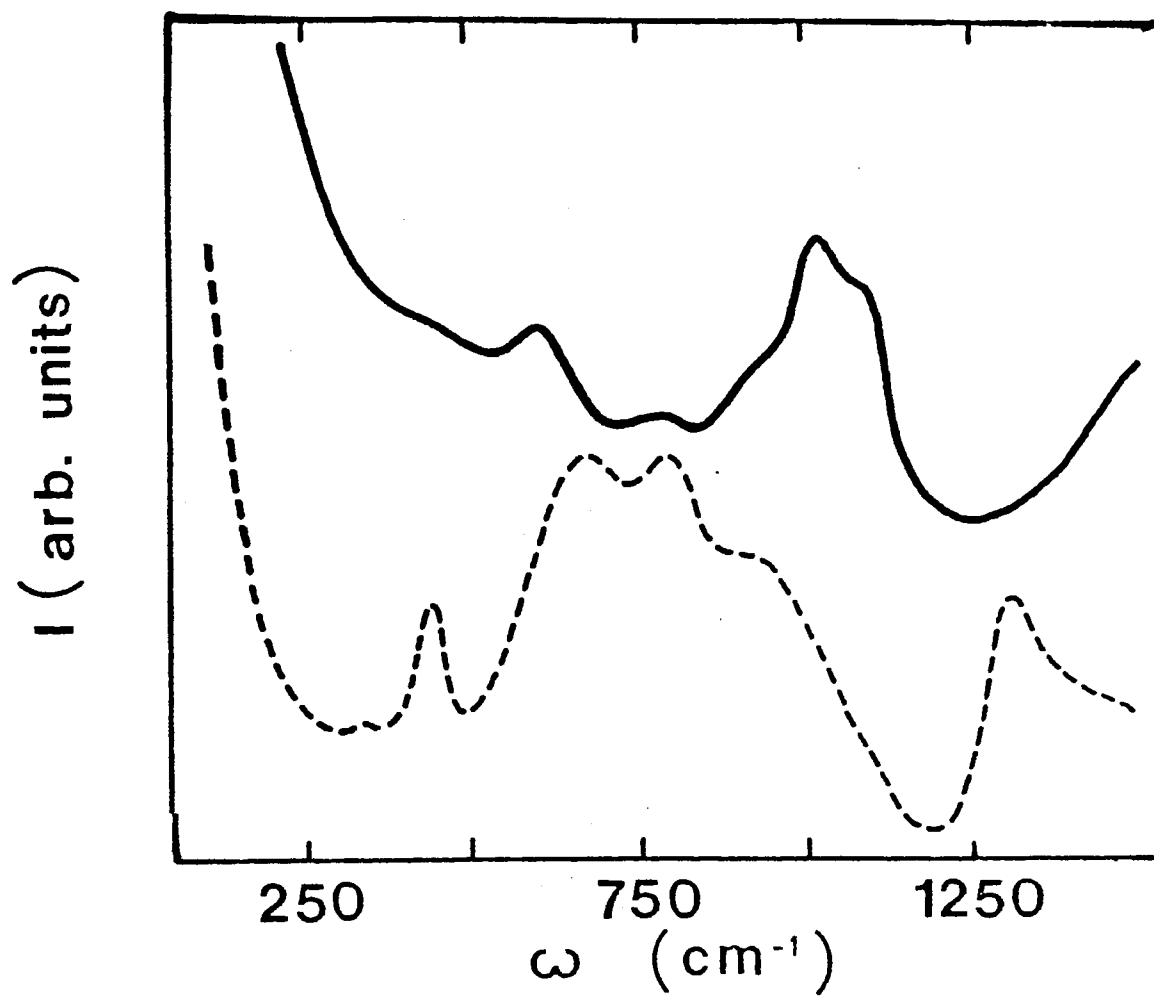


Figure 23. Raman Spectra (Dashed Line) and Resonant Raman Spectra (Solid Line) of Eu³⁺-Doped Sodium Silicate Glass.

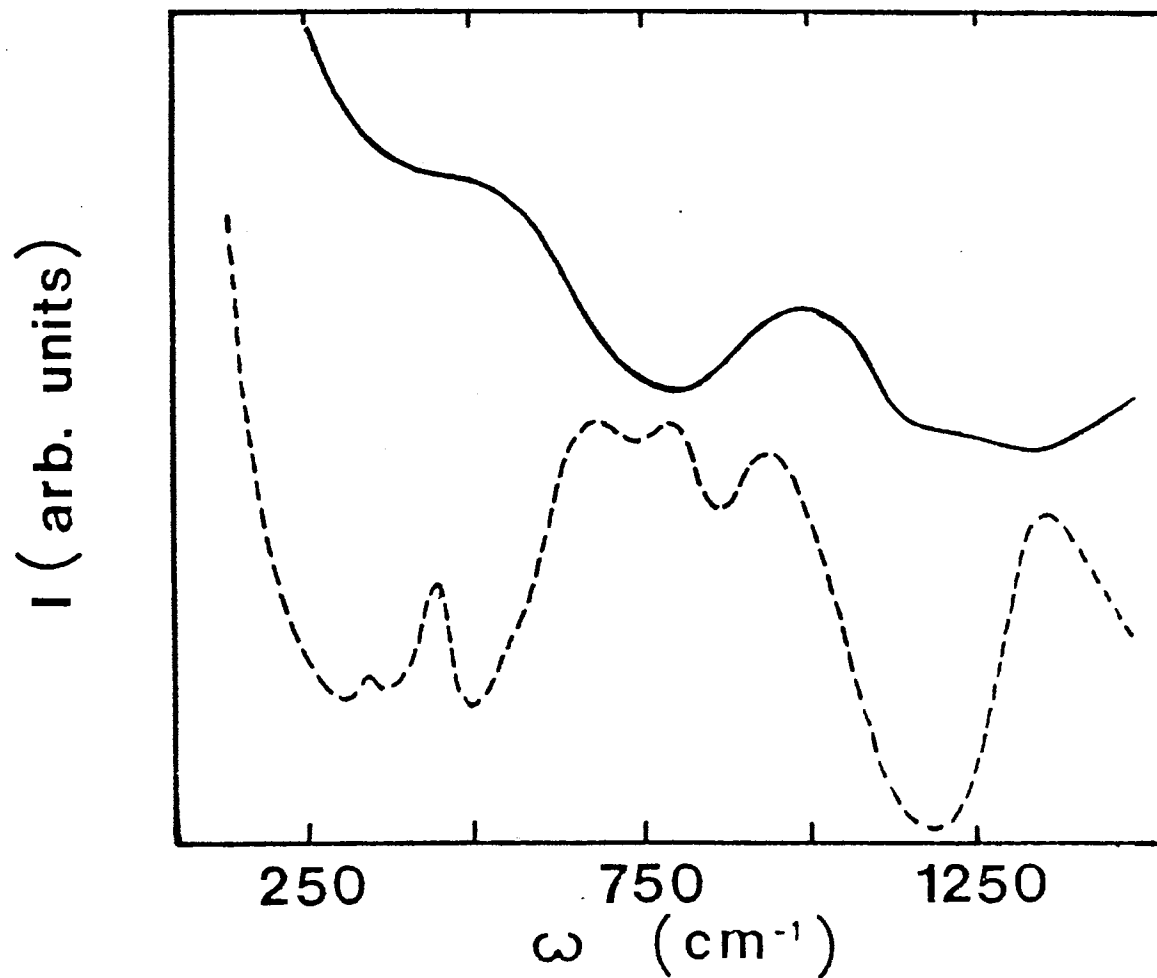


Figure 24. Raman Spectra (Dashed Line) and Resonant Raman Spectra (Solid Line) of Eu^{3+} -Doped Lithium Silicate Glass.

symmetry. The Stokes Raman scattering intensity is given by [24]

$$I(\omega_0, \omega) = \left(\frac{\hbar\nu E_0^2}{2\pi c^3}\right) \left\{(\omega_0 + \omega)^4 \frac{[n(\omega) + 1]}{\omega}\right\} \times \sum_b C_b(\omega_0, \omega) \rho_b(\omega) \quad (25)$$

where b refers to the different bands, E_0 and ω_0 are the incident electric field and frequency, respectively, ω is the frequency of the Raman shift, ρ_b is the vibrational density of states for band b , $n(\omega) = [\exp(\hbar\omega/k_B T) - 1]^{-1}$ is the population factor, and $C_b = |\sum_l P_l u_l^b(\omega)|^2$ is the coupling constant for the b band. Here P^l is the electronic polarizability and u_l is the normal displacement coordinate where l refers to the $3N$ Cartesian coordinates of the atoms. When ω_0 is close to an electronic transition frequency of Eu^{3+} , the coupling coefficient is dominated by contributions of $P^l u_l^b$ associated with vibrational modes localized around the Eu^{3+} ions.

The Raman spectra for the europium pentaphosphate (EP) and lithium phosphate (LP) samples shown in Figs. 21 and 22 both show a high-frequency band near 1200 cm^{-1} which is enhanced in the resonant Raman spectra. This indicates that the vibrational mode of the frequency is strongly coupled to the Eu^{3+} ions. Figures 23 and 24 show similar spectra obtained on sodium silicate (NS) and lithium silicate (LS) glass. The resonant Raman spectrum of the NS glass shows a strong enhancement of a band near 1050 cm^{-1} . This same band appears in the spectra of the LS sample, but no significant enhancement occurs under resonant excitation conditions. Such high-frequency bands do not appear in the Raman spectra of borate and fluorite glasses [25, 26, 27, 28].

These results show that the formation of permanent LIGs of the type of interest here requires a glass host having high-frequency local modes of vibration and further requires these modes to be strongly coupled to the Eu^{3+} ions. This enhances the radiationless relaxation processes compared to the radiative processes occurring after excitation of the Eu^{3+} ions, and these produce the local heating necessary for causing the structural modification of the host.

So far the best hosts for establishing these permanent gratings have been found to be phosphate glasses. The fundamental skeletal structure of phosphate

glasses can be represented by practically infinite chains of interlinked PO_4 tetrahedra with two of the oxygens shared with neighboring tetrahedra. The vibrational band observed around 1200 cm^{-1} is attributed to stretching vibrations of PO_2 lateral groups [29, 30] which involves the two unshared oxygens of the tetrahedra. The resonant enhancement of this band shows that the Eu^{3+} ions are bonded to the PO_2 lateral groups and not to the chains. Thus the Eu^{3+} enter the glass structure as network modifiers. Because of the motional freedom of the lateral group oxygen ions, it is not unreasonable to expect different possible equilibrium positions for these groups, leading to different local environments for dopant ions such as Eu^{3+} .

On the other hand, silicate glasses have fundamental structures which are generally better described as a continuously random packed network with SiO_4 tetrahedra as the basic unit [31]. The introduction of alkali-metal ions partly breaks down this type of structure. These glasses exhibit a vibrational band near 1100 cm^{-1} that is attributed to the bond-stretching vibration of the Si-O nonbridging group [32, 33]. In our sample, the resonantly enhanced band between $1000\text{--}1100\text{ cm}^{-1}$ can be seen as the superposition of three different bands with frequencies 940, 1020, and 1100 cm^{-1} . This last band corresponds to the stretching vibration of the Si-O nonbridging group. These vibrational bands are weaker in the LS sample due to the weaker activation of this vibrational mode by the Li^+ ion as compared with the Na^+ ions [32]. The Raman spectra suggest that part of the Eu^{3+} ions are bonded with the nonbridging oxygen ions in the NS sample, entering the glass structure as network modifiers along with the Na^+ ions. As in the pentaphosphate glasses, it is not unreasonable to expect different possible equilibrium positions for the nonbridging oxygens, leading to different Eu^{3+} environments.

The types of suggested structural modifications discussed above are not applicable to borate glasses where the structure is more rigid and can be formed by various cyclic units depending on the alkali-metal or alkaline-earth-metal content of the material [25, 26, 27]. The major vibrational band of borate glasses is around 805 cm^{-1} and is associated with the breathing mode of the boroxol rings forming the basic structural unit of the glass [25, 26, 27]. The other vibrational bands are

at lower frequencies. The structure of the ZrF_4 -based glasses can be described by chains of ZrF_6 octahedra sharing two oxygens with each of two other octahedra [28]. This is somewhat similar to the phosphate glass structure except that the octahedron are more rigid and exhibit a lower degree of disorder, making it more difficult to consider local structural modifications. The major vibrational bands of these glasses appear around $500\text{--}600\text{ cm}^{-1}$ and are associated with stretching vibrations of the Zr-F nonbridging bonds of the ZrF_6 octahedron forming the basic structural unit of the glass [28].

The results described here are consistent with the model proposed previously for the formation of permanent LIGs through resonant excitation of Eu^{3+} ions in glasses. The criteria for forming gratings of this type include having a glass structure which allows different local configurations for the Eu^{3+} ions through different possible equilibrium positions of the surrounding oxygen ions. The mechanism for switching between different types of equilibrium positions requires structures with high-frequency local vibrational modes such as those associated with structural defects (lateral or nonbridging groups) and further requires that the Eu^{3+} ions are strongly coupled to these vibrational modes. It also appears that these modes should be uncoupled with the rest of the vibrational modes of the structure so that the generation of local heating through radiationless relaxation of the Eu^{3+} ions leads to structural changes instead of becoming thermalized and causing thermal lensing.

To study the affect of the network modifier ions of the host glass on the ability to produce permanent LIGs with high scattering efficiencies, five silicate glasses were obtained which had identical compositions except for one modifier ion. This modifier ion was changed through the series of alkali-metal ions Li, Na, K, Rb, and Cs. These are the last five glasses in Table VI and are listed with their exact compositions.

Permanent LIGs were written in each of the five samples at room temperature and measurements were made of the scattering efficiencies using a He-Ne laser for the read beam. The effective scattering efficiency, which is defined below, was

found to decrease as the modifier ion was changed from Li→ Na→ K→ Rb→ Cs and the results are shown in Fig. 25 where the experimental values of the effective scattering efficiency are given in Table VII and are plotted versus the mass of the alkali modifier ion. The solid line represents the best fit to the data using the theoretical treatment discussed below.

The temperature dependence of the scattering intensity was also measured in these glasses. It was previously found that the temperature dependence of the scattering efficiency in these types of glasses displayed an Arrhenius type behavior

$$I = I_0 \exp\left(\frac{\Delta E}{kT}\right) \quad (26)$$

where ΔE is the activation energy and k is Boltzmann's constant. The experimental values are displayed in Fig. 26 and Table VIII where it is seen that the alkali-metal glasses display this type of behavior. However, the LS and NS samples display two different regions of behavior. At high temperature they display a larger slope than at low temperatures. Table IX displays the measured activation energies where ΔE_L and ΔE_H refer to these low and high temperature regions. For KS, RS, and CS $\Delta E_L = \Delta E_H$. The values found for the activation energies will be compared with the results from the two-level system model described below.

Two-Level System Model

Permanent changes in the refractive index of a material can be induced by lasers due to several physical processes. However, most of these processes are not consistent with the experimental observations described above. The most common mechanism is the photorefractive effect which is associated with the photoionization of defects and subsequent trapping of the free electrons. This type of mechanism can also lead to spectral hole-burning, however this mechanism is seen only at low temperatures and is incompatible with the results reported here.

The photoionization of defects can cause a change in the refractive index. However, the energy level scheme for Eu^{3+} in these glass hosts is not compatible with an ionization transition at the laser wavelength and powers used in these

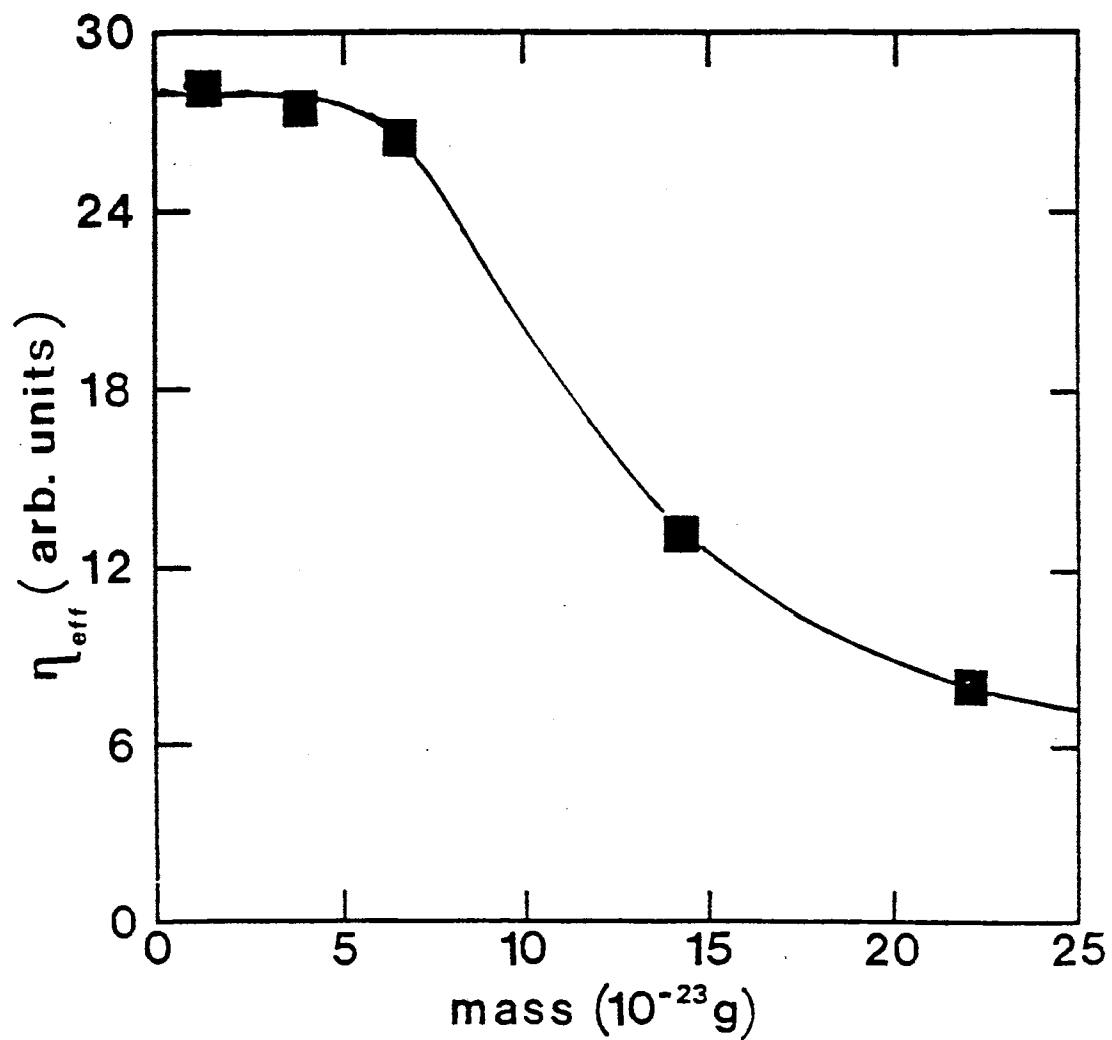


Figure 25. Scattering Efficiency of Silicate Glass Samples as a Function of the Alkali-Metal Ion.

TABLE VII
EXPERIMENTAL VALUES OF THE EFFECTIVE
SCATTERING INTENSITY AS A FUNCTION
OF THE MASS OF THE
ALKALI-METAL ION

Sample	Intensity (arb. units)
LS5	28.24
NS5	27.47
KS5	26.65
RS5	13.30
CS5	8.03

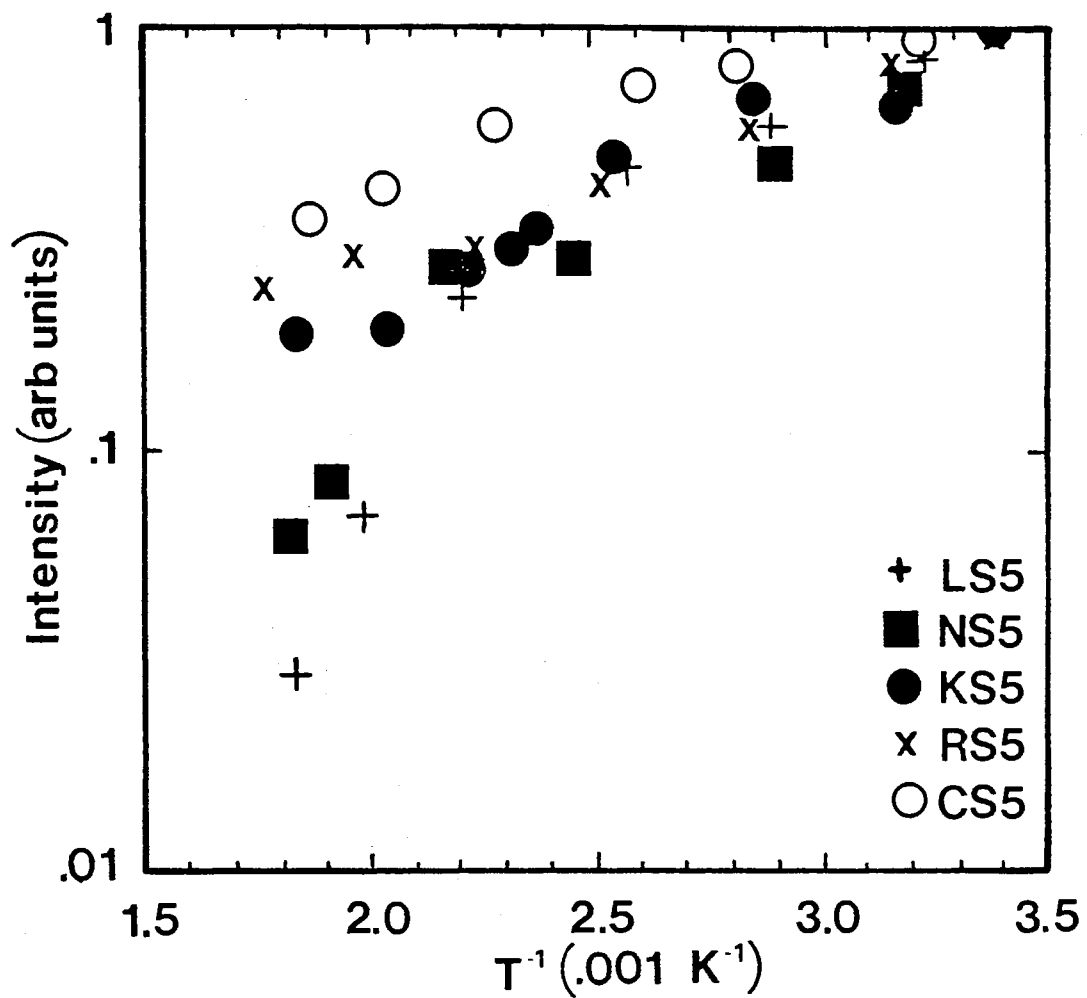


Figure 26. Temperature Dependence of LIG Scattering Intensity for Alkali-Metal Glasses.

TABLE VIII
 EXPERIMENTAL VALUES OF THE SCATTERING
 INTENSITY AS A FUNCTION OF
 THE TEMPERATURE

Sample	$1/T$ (10^{-3} K)	Intensity (arb. units)
LS5	3.367	1.0000
	3.221	.8547
	2.874	.3930
	2.565	.4651
	1.980	.0698
	1.828	.0291
NS5	3.333	1.0000
	3.185	.7127
	2.890	.4872
	2.451	.2792
	2.174	.2721
	1.916	.0845
	1.828	.6160
KS5	3.356	1.0000
	3.155	.6567
	2.841	.6866
	2.532	.4925
	2.364	.3343
	2.309	.2985
	2.212	.2687
	2.033	.1940
1.828	.1910	

TABLE VIII (Continued)

Sample	$1/T$ (10^{-3} K)	Intensity (arb. units)
RS5	3.378	1.0000
	3.170	.7870
	2.841	.5900
	2.513	.4260
	2.237	.2790
	1.969	.2950
	1.764	.2460
CS5	3.378	1.0000
	3.215	.9560
	2.809	.8330
	2.597	.7440
	2.278	.6000
	2.028	.4220
	1.866	.3560

TABLE IX
ACTIVATION ENERGIES OF
ALKALI-METAL GLASSES

Sample	ΔE_H ($\times 10^3 \text{ cm}^{-1}$)	ΔE_L ($\times 10^2 \text{ cm}^{-1}$)
LS5	3.869	8.167
NS5	3.022	7.934
KS5	.894	
RS5	.616	
CS5	.466	

experiments. In addition, the fact that optical erasure occurs only when Eu^{3+} ions are resonantly excited is not consistent with the photoionization mechanism.

The intensities of the two write beams were also monitored as a function of time and no energy transfer between the two beams was observed. These two-beam mixing results show that the laser-induced grating is in phase with the laser interference pattern. This shows that the mechanism causing the grating is localized, which is not always true for gratings involving the migration of charge carriers.

Another mechanism which can produce a permanent grating is the radiation pressure exerted by an electric gradient field on an electric dipole. However, the force exerted on the electric dipole by the electric gradient field was calculated to be 1.05×10^{-13} dynes which is much too small to be considered as the source of the permanent structural modification seen in the samples.

Thermal processes can also directly produce refractive index changes and laser-induced stress-optic changes including some permanent effects have been seen in some rare earth doped glasses [34, 35]. However, these effects occur at higher laser powers than those used in our experiments. For the laser powers used in these experiments, the thermal properties of the glass hosts produce a local rise in the temperature of approximately 3.13×10^{-4} K which is too small to give a measurable effect.

The mechanism which is consistent with the observed results is a change in the local structure of the glass caused by the vibrational energy released during the radiationless relaxation of the rare earth ions. The radiationless relaxation transitions of rare earth ions in glasses have been shown to be multiphonon emission process [15] each of which generates several high energy phonons of the order of 1000 cm^{-1} . Since these are generated by the rare earth ions and the thermal diffusion in glasses is slow, the phonons are localized thus creating a high level of nonthermalized vibrational energy around each ion. This can produce a local effective temperature which is extremely high, depending on the energy gap being crossed in the relaxation process. For the Eu^{3+} and Pr^{3+} ions under the excitation

conditions of these experiments, effective local temperatures of several thousand degrees Kelvin can be produced. This is easily enough to allow ionic motion over short ranges and thus produce a local structural modification of the host glass. The energy associated with this local temperature rise is consistent with the measured activation energies for the formation and erasure of permanent gratings. In addition, the time scale of several minutes for grating formation and erasure is consistent with the time scale for producing structural changes.

Based on the above discussion, a double minima potential well model was proposed to explain the permanent LIGs. In the double minima potential well model the network former and network modifier ions of the glass host can arrange themselves in two possible configurations in the local environment of the Eu^{3+} ion. Thus these ions or groups of these ions have available to them two mutually accessible equilibrium positions and move in a potential of the form shown in Fig. 27. In this model it is assumed that the index of refraction depends on which configuration is present. Thus the total index of refraction of the material will be of the form

$$n = n_I N_I + n_{II} N_{II} \quad (27)$$

where $N_{I(II)}$ is the population of well I(II) and $n_{I(II)}$ is the index of refraction per ion populating the well. When the laser beam is turned on the population of the wells will display a time dependence of the form

$$\frac{dN_I(t)}{dt} = -p_I N_I(t) + p_{II} N_{II}(t) \quad (28)$$

$$\frac{dN_{II}(t)}{dt} = p_I N_I(t) - p_{II} N_{II}(t) \quad (29)$$

where $p_{I(II)}$ is the jump frequency and is the probability per unit time that the ion will have enough energy to jump from well I(II) to well II(I). In these experiments the system is allowed to reach equilibrium before measurements are taken. Thus the population of each well can be taken as constant and Eqs. 28 and 29 give the ratio of the populations of the two wells as

$$\frac{N_I(\infty)}{N_{II}(\infty)} = \frac{p_{II}}{p_I} \quad (30)$$

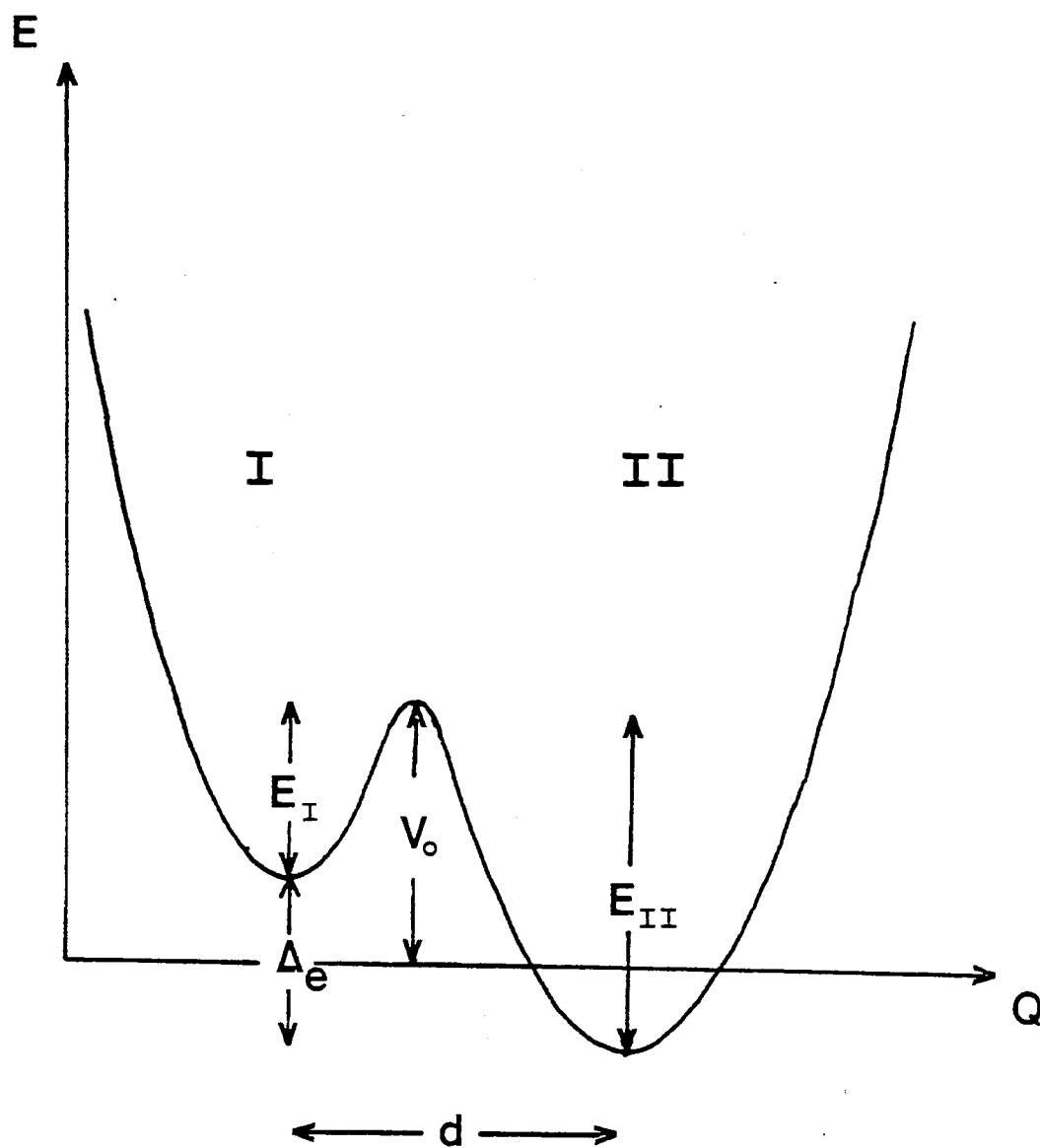


Figure 27. Two-Level System Model.

where $p_{I(II)}$ is given by [36]

$$p_{I(II)} = \nu_{I(II)} \exp\left(-\frac{E_{I(II)}}{k_B T}\right). \quad (31)$$

k_B is Boltzmanns constant and $\nu_{I(II)}$ is the attack frequency which is the number of attempts the ion makes at surmounting the barrier of height $E_{I(II)}$. Equations 30 and 31 lead to the thermal equilibrium condition

$$\frac{N_I(\infty)}{N_{II}(\infty)} = \frac{\nu_{II}}{\nu_I} \exp\left(-\frac{\Delta_e}{k_B T}\right) \quad (32)$$

where $\Delta_e = E_{II} - E_I$. The equations derived so far are completely general and are valid for a single beam or crossed beam experiments.

For crossed beams the intensity of the LIG signal is given by [37]

$$I \propto |n_p - n_v|^2 \quad (33)$$

where n_p and n_v refer to the index of refraction of the peak and valley regions of the LIG with

$$n_p = n_I N_{Ip}(\infty) + n_{II} N_{IIp}(\infty) \quad (34)$$

$$n_v = n_I N_{Iv}(\infty). \quad (35)$$

The p and v subscripts refer to the peak and valley regions of the LIG whereas the I and II subscripts refer to the potential well occupied. In arriving at Eq. 35 it is assumed that the ions in the valley region of the grating remain in well I for all times. These equations lead to the following expression for the LIG signal intensity

$$I \propto |N_{IIp}(\infty) \Delta n_{II-I}|^2 \quad (36)$$

where $\Delta n_{II-I} \equiv n_{II} - n_I$. By using the thermal equilibrium condition and the fact that the total population of the wells must remain constant, the LIG signal intensity can be written as

$$I \propto \frac{N_I^2(0) |\Delta n_{II-I}|^2}{\left[1 + \frac{\nu_{II}}{\nu_I} \exp\left(-\frac{\Delta_e}{k_B T}\right)\right]^2} \quad (37)$$

where $N_I(0)$ is defined as $N_{Ip}(0) = N_{Iv}(0) \equiv N_I(0)$.

This model can be used to interpret the observed changes in LIG signal intensities. For the MP50 sample and the MP10 sample the only difference will be in the initial population of configuration I. The ratio of the LIG signal intensities will be given by

$$\frac{I_{50}}{I_{10}} \propto \left(\frac{N_I(0)_{50}}{N_I(0)_{10}} \right)^2. \quad (38)$$

This ratio of the squares of the initial populations was calculated using the Eu^{3+} concentration and the size of the peak region of the grating and was found to be 56.33. This number is larger than the measured ratio of 8, however, taking into consideration the simplicity of the model which does not include any saturation effects which have been seen in power dependence measurements [8, 9] the model does a fairly good job in predicting the relative change in LIG signal intensities with a change in Eu^{3+} concentration.

This model can also be used to explain the results shown in Fig. 25. Since the only component of these glasses which has changed is the alkali-metal ion and it is seen that the effective scattering efficiency varies as the mass of this alkali-metal ion, this alkali-metal ion can be taken as the ion that is moving to provide the double equilibrium configuration surrounding the Eu^{3+} ion. In Eq. 37, $N_I(0)$, which is the initial population of well I, will depend on the size of the peak or valley regions of the LIG. Therefore, the effective scattering efficiency is defined as

$$\eta_{eff} \equiv \frac{I}{N_I^2(0)} \propto \frac{|\Delta n_{II-I}|^2}{\left\{ 1 + \frac{\nu_{II}}{\nu_I} \exp\left(-\frac{\Delta_e}{k_B T}\right) \right\}^2}. \quad (39)$$

The attack frequency, $\nu_{I(II)}$ is proportional to the mass of the ion in the well and can be expressed as

$$\nu_{I,II} = \sqrt{\frac{k_{I(II)}}{m}} \quad (40)$$

where $k_{I(II)}$ is the force constant of well I(II) and m is the mass of the ion populating the well. Δn_{II-I} is the change in refractive index per ion and is treated as an adjustable parameter. The term Δ_e which is the difference in the minima of the potential wells can be expressed more specifically using the mathematical formalism developed to describe a double minima potential well [38]. The details are provided in the Appendix.

Basis states $|\Phi_1\rangle$ and $|\Phi_2\rangle$ are chosen which are ground states for the appropriate single well potentials. These basis states are eigenstates of the Hamiltonian of the unperturbed system H_0 with eigenvalues E_1 and E_2 ,

$$H_0 |\Phi_1\rangle = E_1 |\Phi_1\rangle \quad (41)$$

$$H_0 |\Phi_2\rangle = E_2 |\Phi_2\rangle . \quad (42)$$

Upon applying a perturbation W which couples $|\Phi_1\rangle$ and $|\Phi_2\rangle$ the Hamiltonian matrix will become

$$(H) = \begin{pmatrix} E_1 + \langle \Phi_1 | W | \Phi_1 \rangle & \langle \Phi_1 | H | \Phi_2 \rangle \\ \langle \Phi_2 | H | \Phi_1 \rangle & E_2 + \langle \Phi_2 | W | \Phi_2 \rangle \end{pmatrix}. \quad (43)$$

To a good approximation $\langle \Phi_i | W | \Phi_i \rangle \ll E_i$. Defining the zero of energy to be midway between E_1 and E_2 the Hamiltonian matrix will become

$$(H) = \frac{1}{2} \begin{pmatrix} \Delta_e & \Delta_0 \\ \Delta_0 & -\Delta_e \end{pmatrix} \quad (44)$$

where Δ_0 is defined as

$$\Delta_0 = 2 \langle \Phi_1 | W | \Phi_2 \rangle . \quad (45)$$

$\Delta_0/2$ is the coupling energy and is the difference between the two lowest symmetric states. The solution for the coupling energy is derived in a number of quantum mechanics text books and is given by [39]

$$\Delta_0 = \hbar\omega_0 \exp \left[-d \left(\frac{2mV_0}{\hbar^2} \right) \right] \quad (46)$$

where $\hbar\omega_0$ is an energy roughly equal to the zero point energy and will vary as $1/\sqrt{m}$. For this reason we can write

$$\Delta_0 = \hbar \sqrt{\frac{k}{m}} \exp \left[-d \left(\frac{2mV_0}{\hbar^2} \right)^{\frac{1}{2}} \right] \quad (47)$$

where k is the force constant for the initial configuration.

The coupling energy can be related to the asymmetry by [40]

$$\tan \Theta = \frac{\Delta_0}{\Delta_e} \quad (48)$$

where Θ is a measure of the mixing of the original eigenstates due to the perturbation. Combining Eqs. 47 and 48 gives

$$\Delta_e = \frac{\hbar}{\tan \Theta} \sqrt{\frac{k}{m}} \exp \left[-d \left(\frac{2mV_0}{\hbar^2} \right)^{\frac{1}{2}} \right]. \quad (49)$$

Inserting this into Eq. 39 the effective scattering efficiency becomes

$$\eta_{eff} = \frac{|\Delta n_{II-I}|^2}{\left\{ 1 + \frac{\nu_{II}}{\nu_I} \exp \left[-\frac{\hbar}{k_B T \tan \Theta} \sqrt{\frac{k}{m}} \exp \left[-d \left(\frac{2mV_0}{\hbar^2} \right)^{\frac{1}{2}} \right] \right] \right\}^2}. \quad (50)$$

Equation 50 was fit to the experimental values of the effective scattering efficiency with $|\Delta n_{II-I}|^2$, ν_{II}/ν_I , $\hbar\sqrt{k}/k_B T \tan \Theta$, and $d(2V_0/\hbar^2)^{1/2}$ treated as adjustable parameters. The best fit to the data is the solid line plotted in Fig. 25 where the following values were found for the adjustable parameters:

$$\begin{aligned} |\Delta n_{II-I}|^2 &= 2.787 \times 10^{-37} \\ \frac{\nu_{II}}{\nu_I} &= 1.329 \\ \frac{\hbar\sqrt{k}}{k_B T \tan \Theta} &= 2.25 \times 10^{10} \\ d \left(\frac{2V_0}{\hbar^2} \right) &= 2.39 \times 10^{-11}. \end{aligned} \quad (51)$$

It is seen that as an ion moves from one potential well to the other the index of refraction changes by 5.279×10^{-19} . The number of ions that accumulate in well II is of the order of 1×10^{16} . This gives a total change in the index of refraction of 5.279×10^{-3} . This number is of a similar order of magnitude to that found in other experiments [16].

From the ratio of the attack frequencies the relationship between the force constants of the individual well can be found. From Eq. 40 it is seen that

$$\frac{\nu_{II}}{\nu_I} = \sqrt{\frac{k_{II}}{k_I}}. \quad (52)$$

It is seen that the force constant for well II, k_{II} is 1.766 times larger than that for well I, k_I .

It is also possible to approximate the distance between the two wells, d , using the last parameter. From Fig. 27 it is seen that V_0 must be as large as $\Delta_e/2$. Taking V_0 to range from 3000 cm^{-1} for LS5 to 45 cm^{-1} for CS5 leads to

values of d from .023 Å to .189 Å respectively. It should be remembered that this model has considered only the alkali ion to be the source of the double minima potential well. There are realistically many ions involved and the small values for d suggest that even though individual ions may move over large distances the net affect on the configuration coordinate is minimal in moving between equilibrium configurations.

From the final two adjustable parameters it is possible to calculate Δ_e for each sample using Eq. 49. These values are listed in Table X. It is observed that as the mass of the network modifier ion increases there is a dramatic change in the asymmetry. As this ion becomes heavier the difference in the minima of the two wells becomes less, implying that the change in the local environment of the Eu^{3+} ion becomes less pronounced as you go from $\text{Li} \rightarrow \text{Na} \rightarrow \text{K} \rightarrow \text{Rb} \rightarrow \text{Cs}$. It has been reported that in alkali silicate glasses the glass becomes more ordered as the radius of the alkali ion increases [41]. This same trend would be expected to continue in these glasses and as the glass becomes more ordered there would be less opportunity for multiple configurations leading to a smaller asymmetry between the two potential wells.

To compare the values of Δ_e calculated from the two-level system model to the values of ΔE found from temperature dependent measurements of the scattering intensity a relation between the two must be found. Solving Eq. 32 for N_{IIP} and substituting directly into Eq. 36 leads to the following equation for the temperature dependence of the LIG signal intensity

$$I \propto N_I^2(\infty) \Delta n_{II-I}^2 \left(\frac{\nu_I}{\nu_{II}} \right)^2 \exp \left(\frac{2\Delta E}{kT} \right). \quad (53)$$

Comparing this result with Eq. 26 it is seen the measured value of the activation energy ΔE is equal to twice the asymmetry of the two-level system model, Δ_e . Table XI displays these values where for simplicity only the value of ΔE_H has been plotted. The agreement between the values is quite good considering the simplicity of the model, all values are within an order of magnitude of each other. It should also be pointed out at this time that the equation derived for the permanent LIG

TABLE X
SUMMARY OF PARAMETERS FROM
TWO-LEVEL SYSTEM MODEL

Sample	Δ_e (cm^{-1})	$N_I(0)$ $\times 10^{16}$	$N_I(\infty)$ $\times 10^{15}$	$N_{II}(\infty)$ $\times 10^{16}$	$\frac{N_{II}(\infty)}{N_I(0)}$
LS5	6068.38	1.041	0	1.041	1.00
NS5	1714.43	1.809	.001	1.808	.999
KS5	838.61	.815	.181	.7969	.978
RS5	225.84	.718	2.21	.4972	.692
CS5	89.69	.442	2.04	.2376	.538

TABLE XI
VALUES OF ACTIVATION
ENERGY AND
ASYMMETRY

Sample	ΔE (10^3 cm^{-1})	$2\Delta_e$ (10^3 cm^{-1})
LS5	3.869	12.136
NS5	3.022	3.428
KS5	.894	1.678
RS5	.616	.452
CS5	.466	.179

signal intensity is applicable to any rare earth ion and only depends on the glass host. Therefore, the activation energy from the Pr^{3+} -doped silicate glass should be the same as that in the NS5 sample. It was found that this activation energy was $2.825 \times 10^3 \text{ cm}^{-1}$ which is in excellent agreement with the two-level system model.

From Eq. 32 and the fact that the initial population of well I must equal the final population of well I and well II it is possible to find the final populations of the two wells for each sample. These populations along with the ratio of the final population of well II to the initial population of well I are given in Table X. This ratio can be interpreted as the relative effectiveness of moving an ion initially in well I to well II. It is observed that in LS5, NS5, and KS5 almost one hundred percent of the ions are driven into well II. In RS5 and CS5 a majority will end up in well II, however it is a much smaller number than in the first three. In the heavier alkali glasses it is harder to trap the ions in well II implying that the asymmetry is less than in the lighter alkali glasses.

The inability to produce a LIG in fluoride glasses is also consistent with the double-minima potential well model which requires the presence of high energy "phonons" to enable the ions to surmount the barrier and hop from well I to well II. With the absence of the high energy local mode vibrations produced by radiationless relaxation of the Eu^{3+} ions the ions remain trapped in well I and no grating will be produced.

Summary and Conclusions

The double minima potential well model used to describe the formation of the permanent, LIG agrees well with experimental results. It also provides some insight into the physical processes involved in the formation and erasure of these gratings. However, caution must be used in the interpretation of the physical parameters since a simple model is being used to describe a complex and poorly understood physical system.

The Eu^{3+} ions play a major role by providing the high energy local mode phonons required to produce a structural modification of the glass host. The strength of the grating which can be produced is proportional to the concentration of Eu^{3+} ions, however, at high Eu^{3+} concentrations saturation effects occur.

The structure of the glass host in the local environment of the Eu^{3+} ions is also important to the formation of the grating. By changing one of the network modifier ions variations in the LIG intensity can be produced.

As a simple model consider the glass to consist of point masses connected by springs. These point masses have available to them two equilibrium configurations which result from a change in position or a change in the force constants of the springs to which they are attached. Independent measurements have shown the elastic constants of the glasses to decrease from LS5 to CS5 [42]. This implies that the two equilibrium configurations will be more stable in the lighter alkali glasses than in the heavier ones. This will result in a larger value of $N_{II}(\infty)/N_I(0)$ in the lighter alkali glasses than in the heavier alkali glasses and is what is observed in Table X.

Stronger elastic constants also suggest there will be less displacement of the ions in the lighter alkali glasses. This is exactly what was calculated where it was found that d ranged from .023 Å for LS5 to .189 Å for CS5.

The ball and spring model above which gives a feel for what is happening physically agrees quite well with the results of the two-level system model. As pointed out earlier though this model is quite simplified and does not take into account the rare earth ion involved or saturation effects, thus it should be used with these points taken into consideration.

CHAPTER III

APPLICATIONS OF LASER-INDUCED GRATINGS

Introduction

In the past decade there has been a dramatic increase in interest in optical devices resulting from the invention of the laser and the development of fiber optics. Several new devices have been developed including photo-optical switches [4], narrow-band-waveguide reflection filters [43], and opto-optical deflectors [44]. As the names imply these devices rely on the interaction of light with matter and are created by optical interference methods. The exact mechanism responsible for the creation of the optical device depends on the material being utilized.

The materials discussed in the preceding chapter are excellent candidates for the creation of new and useful devices. They can be produced relatively easily and at low costs and are easy to integrate into fiber optic systems. The LIGs used to produce the devices described below have the added benefit of being stable indefinitely at room temperature and are insensitive to broadband light.

In this chapter novel applications of the LIGs are demonstrated and their applicability to specific devices discussed. First, the long-term room temperature stability is discussed in terms of holographic imaging. Areas of application include information storage and medical imaging. Next, the demultiplexing of multifrequency laser beam is investigated and its applicability to superimposing multiple gratings in order to create a tunable, frequency selective filter is studied. The final application involves utilizing the transient component of the LIG to perform beam-to-beam information coupling through amplitude modulation.

Experimental Configuration

The experimental configuration used to form the LIG is essentially the same as that reported in Chapter II. For these applications it is important to recall that the LIG was produced using the 4658 Å line of an argon-ion laser and that the power of a single beam was of the order of 70 mW. The only significant addition is a mirror, mounted on a translational base which can move parallel to the sample, which is placed between the probe laser and the sample. This facilitates proper alignment of the probe beam and allows the angle between the probe beam and the perpendicular to the sample to be monitored. The probe beam, with a wavelength in the sample λ_P , is reflected off this mirror and onto the sample at an angle θ_A from the perpendicular to the sample. Φ_A is the angle measured in air, once inside the sample the angle becomes Φ_S which is corrected for the samples index of refraction.

The samples used in these experiments are ordinary phosphate and silicate glasses which have been doped with Eu^{3+} ions. In the holographic storage experiments a phosphate glass, MP10, was used and in the demultiplexing experiments MP10, and a silicate glass, NS5, were investigated. In the signal modulation experiment the sample was a silicate glass, LS5. The compositions of these samples is given in the preceding chapter. All samples display the same LIG characteristics so any of them could have been used for any of the experiments. The laser wavelength used for writing the gratings is in resonance with an absorption transition of the Eu^{3+} ions.

Holographic Information Storage

The time evolution of a LIG is reflected in the intensity of the signal beam and for the type of gratings of interest here this time dependence was displayed in Fig. 1. It was seen that when the write beams are turned off the grating decays with a rate equal to the decay rate of the $^5\text{D}_0$ excited state of the Eu^{3+} ion [45]. However, the signal does not return to zero but rather to approximately 60% of

its original value implying the formation of a permanent grating. The permanent grating can then be erased thermally by heating the sample to temperatures above room temperature or it can be erased optically by illuminating the grating with a single beam tuned in resonance with the 7F_0 - 5D_2 absorption transition of the Eu^{3+} ion. No grating formation or erasure occurs if the beams are not in resonance with the 7F_0 - 5D_2 absorption transition.

These results demonstrate that permanent holographic images can be written in rare-earth doped phosphate and silicate glasses using this technique. Since the mechanism responsible for the formation of the permanent LIG involves structural changes which are stable at room temperature, these images have an infinite fading time. This suggests the use of these glasses in areas such as optical information processing and medical imaging where there is a need for long-term information storage. Even though the response time of the material is too slow for real-time processing the long-time room temperature stability makes it important for read only applications. This is a significant advantage over many photorefractive materials whose memory is volatile at room temperature and the image must be fixed in order to remain stable [46]. Another advantage is that diffraction efficiencies as high as 30 % have been observed in these glasses without the use of external fields. This occurs with the use of a common argon laser and relatively low power.

Demultiplexing Results

To investigate the demultiplexing properties of the permanent LIG in these types of glasses permanent gratings were written in the MP10 and NS5 glass samples. The angle between the write beams, $2\theta_A$ was measured to be 2.22° in air or, with an index of refraction of 1.5 for the glass, 1.48° inside the sample, which is defined as $2\theta_S$. The grating spacing, which is the distance between the fringes of the LIG, is designated as Λ_G . The definition of these parameters is displayed in Fig. 3.

The permanent LIG was probed with both a helium-neon laser and several different lines of an argon-ion laser . The strength of the probe beam was kept under 15 mW and out of resonance with the 7F_0 - 5D_2 Eu^{3+} absorption transition to insure no erasure of the permanent LIG. The geometry of the probe portion of the experiment is presented in Fig. 5. The alignment of the probe beam for maximum scattering efficiency is determined by the probe beam wavelength and the wavelength of the permanent LIG.

To determine the spatial displacement of the signal beam, its intensity was measured as a function of the angle of incidence of the probe beam Φ_A . This measurement was performed with probe beam wavelengths in air of 632.8, 514.5, 501.7, 496.5, 488.0, and 476.5 nm. Figure 28 displays the results for the MP10 sample where Φ_A has been converted to Φ_S and for clarity only the results from probe beam wavelengths of 632.8 and 514.5 nm are displayed. Table XII displays the results for all the wavelengths. It should be pointed out that the same type of behavior was observed for all probe beam wavelengths with a shift in the angle for maximum scattering. An identical behavior was seen in the NS5 glass and the numerical values are displayed in Table XIII. It is seen that as Φ_S is varied the signal intensity increases from zero to a maximum then decreases back to zero as would be expected for Bragg scattering.

Figure 29 displays the probe beam wavelength in the sample, λ_p versus the angle, Φ_S at which maximum signal intensity occurs. As the probe beam wavelength decreases, the angle at which maximum signal intensity occurs also decreases. This is described by the Bragg scattering Eq. [37]

$$n\lambda_p = 2\Lambda_G \sin \Phi_0 \quad (54)$$

where λ_p is the probe beam wavelength, Λ_G is the wavelength of the permanent LIG grating, and Φ_0 is the Bragg angle. For the experiments performed here the values of Φ_S plotted in Fig. 29 may not represent the Bragg angle Φ_0 . If the fringes of the permanent LIG are not perpendicular to the sample surface then Φ_S will not be equal to Φ_0 . If the fringes of the permanent LIG make an angle Φ' to the

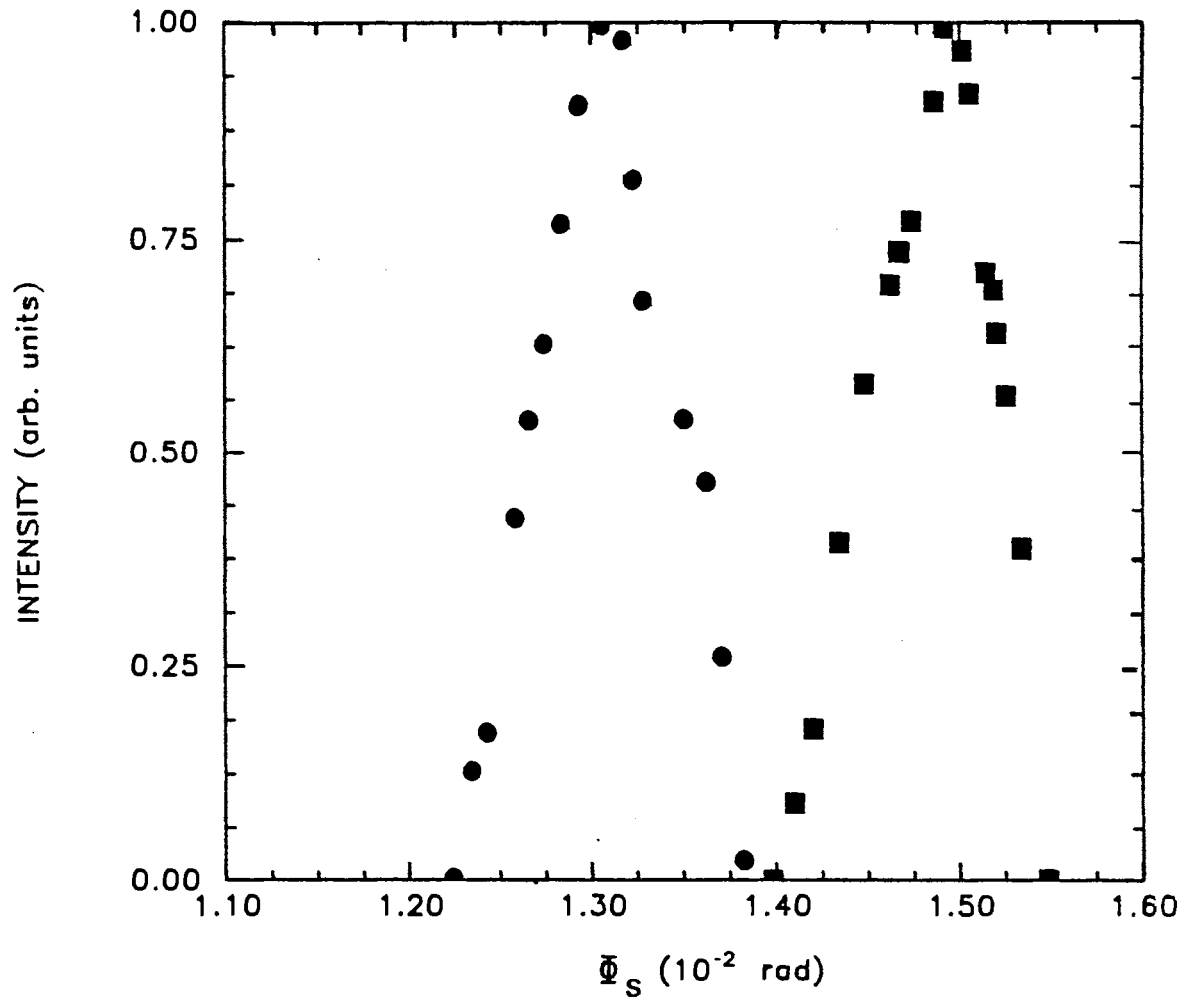


Figure 28. Intensity of LIG Signal as a Function of the Angle Between the Probe Beam and the Perpendicular to the MP10 Sample.

TABLE XII
SIGNAL INTENSITY AS A FUNCTION
OF PROBE BEAM ANGLE
FOR MP10 SAMPLE

Intensity (arb. units)	Φ_S (rad)
$\Lambda_P = 6328 \text{ \AA}$	
0.000	0.01396
0.095	0.01408
0.180	0.01418
0.397	0.01432
0.585	0.01446
0.700	0.01460
0.740	0.01465
0.775	0.01472
0.910	0.01484
1.000	0.01489
0.970	0.01499
0.918	0.01503
0.715	0.01512
0.695	0.01516
0.645	0.01518
0.570	0.01523
0.390	0.01532
0.000	0.01548

TABLE XII (Continued)

Intensity (arb. units)	Φ_S (rad)
$\Lambda_P = 5145 \text{ \AA}$	
0.000	0.01225
0.130	0.01235
0.175	0.01244
0.425	0.01259
0.540	0.01267
0.630	0.01275
0.770	0.01284
0.905	0.01294
1.000	0.01306
0.980	0.01318
0.820	0.01323
0.680	0.01329
0.540	0.01351
0.465	0.01363
0.260	0.01372
0.025	0.01384
$\Lambda_P = 5017 \text{ \AA}$	
0.000	0.01233
0.345	0.01247
0.775	0.01259
0.875	0.01274
0.950	0.01287
1.000	0.01301
0.990	0.01314
0.970	0.01329
0.925	0.01344
0.730	0.01357
0.715	0.01371

TABLE XII (Continued)

Intensity (arb. units)	Φ_S (rad)
$\Lambda_P = 4965 \text{ \AA}$	
0.150	0.01219
0.315	0.01229
0.475	0.01239
0.960	0.01258
0.970	0.01271
0.985	0.01288
1.000	0.01303
0.990	0.01317
0.970	0.01323
0.650	0.01342
0.475	0.01356
0.000	0.01371
$\Lambda_P = 4880 \text{ \AA}$	
0.000	0.01189
0.215	0.01200
0.320	0.01208
0.745	0.01221
0.770	0.01231
0.815	0.01245
0.955	0.01262
1.000	0.01281
0.950	0.01297
0.825	0.01318
0.745	0.01337
0.230	0.01356
0.080	0.01368

TABLE XII (Continued)

Intensity (arb. units)	Φ_S (rad)
$\Lambda_P = 4765 \text{ \AA}$	
0.030	0.01157
0.220	0.01167
0.400	0.01181
0.525	0.01194
0.650	0.01207
0.765	0.01223
0.850	0.01233
0.920	0.01245
1.000	0.01259
0.910	0.01276
0.815	0.01290
0.670	0.01308
0.520	0.01322
0.240	0.01335

TABLE XIII
 SIGNAL INTENSITY AS A FUNCTION
 OF PROBE BEAM ANGLE
 FOR LS5 SAMPLE

Intensity (arb. units)	Φ_S (rad)
$\Lambda_P = 6328 \text{ \AA}$	
0.107	0.01517
0.271	0.01508
0.573	0.01498
0.693	0.01493
0.789	0.01488
0.877	0.01481
0.965	0.01470
1.000	0.01465
0.972	0.01460
0.893	0.01435
0.721	0.01432
0.431	0.01420
0.244	0.01409
0.134	0.01403
$\Lambda_P = 5145 \text{ \AA}$	
0.277	0.01286
0.409	0.01280
0.630	0.01269
0.870	0.01262
0.915	0.01256
0.950	0.01245
0.972	0.01230
1.000	0.01220
0.910	0.01200
0.767	0.01190
0.413	0.01173
0.202	0.01154

TABLE XIII (Continued)

Intensity (arb. units)	Φ_S (rad)
$\Lambda_P = 4880 \text{ \AA}$	
0.000	0.01234
0.175	0.01230
0.278	0.01225
0.531	0.01219
0.618	0.01214
0.734	0.01206
0.805	0.01195
0.911	0.01182
0.946	0.01166
1.000	0.01153
0.997	0.01140
0.962	0.01128
0.828	0.01109
0.702	0.01093
0.600	0.01082
0.241	0.01068
0.166	0.01053
$\Lambda_P = 4765 \text{ \AA}$	
0.310	0.01200
0.451	0.01192
0.619	0.01184
0.848	0.01176
0.935	0.01167
0.987	0.01158
1.000	0.01146
0.991	0.01132
0.936	0.01119
0.855	0.01103
0.527	0.01089
0.374	0.01082
0.110	0.01074

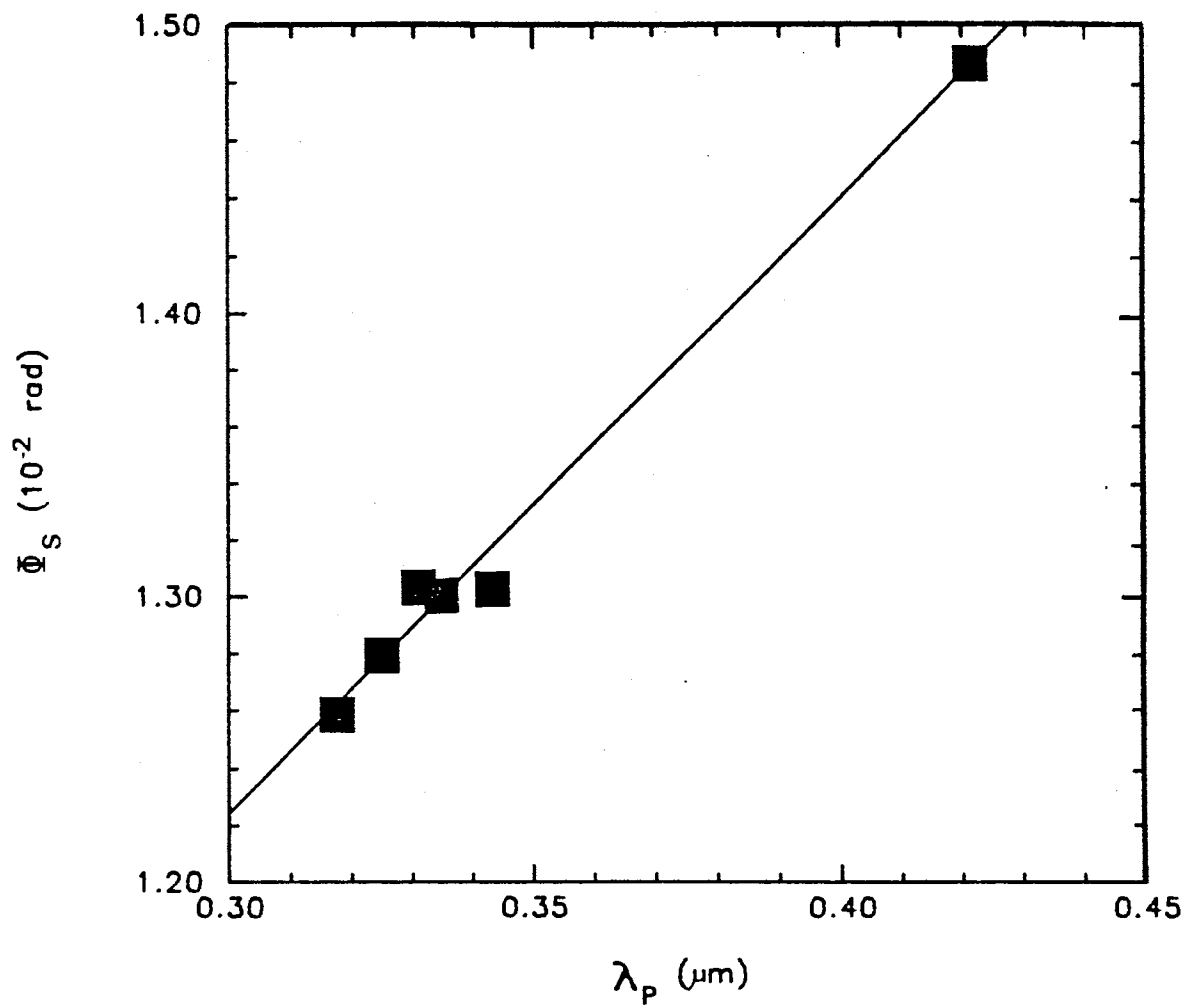


Figure 29. Angle in the Sample at Which Maximum Scattering Intensity Occurs Versus Probe Beam Wavelength in the MP10 Sample.

perpendicular to the sample surface then the Bragg angle will be $\Phi_0 = \Phi_S - \Phi'$ as is displayed in Fig. 30.

In order to correct for this the Bragg angle Φ_0 must be replaced with $\Phi_S - \Phi'$. It is unlikely that Φ' will be known accurately, thus consider the case of two probe beams λ_{p1} and λ_{p2} which have two separate Bragg angles Φ_{01} and Φ_{02} . Since only Φ_S is changing Φ' will remain the same for both beams so that

$$\lambda_{p1} = 2\Lambda_G \sin(\Phi_{S1} - \Phi') \quad (55)$$

$$\lambda_{p2} = 2\Lambda_G \sin(\Phi_{S2} - \Phi'). \quad (56)$$

For small angles $\sin(\Phi_S - \Phi') = (\Phi_S - \Phi')$. Taking the difference between these two equations gives

$$\Delta\lambda_p = 2\Lambda_G \Delta\Phi_S. \quad (57)$$

Thus the grating spacing is given by

$$\Lambda_G = \frac{\Delta\lambda_p}{2\Delta\Phi_S}. \quad (58)$$

The solid line in Fig. 29 represents the best fit to the data and the slope of the line gives

$$m = \frac{\Delta\Phi_S}{\Delta\lambda_p} \quad (59)$$

so that the wavelength of the permanent grating is

$$\Lambda_G = \frac{1}{2m}. \quad (60)$$

The slope of the solid line in Fig. 29 was found to be $.0214 \mu\text{m}$ corresponding to a grating spacing of $23.364 \mu\text{m}$. In order to check this value the grating spacing of the sinusoidal light interference pattern was calculated. This is also given by Bragg's Law and will exhibit a wavelength of

$$\Lambda_L = \frac{\lambda_W}{\Theta_S} \quad (61)$$

where λ_W is the write beam wavelength. For a write beam wavelength of $.3105 \mu\text{m}$ and crossing angle of $.0258$ radians the wavelength of the sinusoidal interference pattern should be $12.022 \mu\text{m}$. It is seen that the permanent LIG apparently

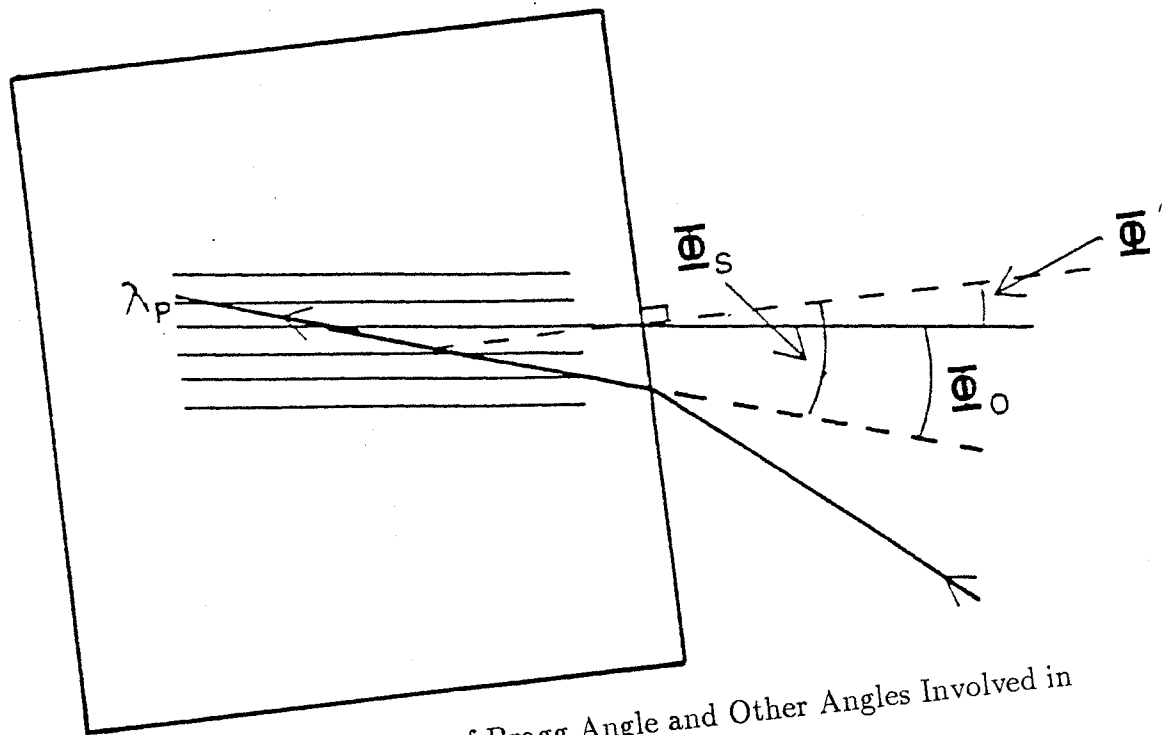


Figure 30. Definition of Bragg Angle and Other Angles Involved in Grating Spacing Calculation.

displays a wavelength approximately twice that of the sinusoidal laser interference pattern.

It has been shown that the Eu^{3+} -doped phosphate glasses exhibit thermal lensing [16]. When illuminated with a single beam tuned in resonance with the ${}^7\text{F}_0$ - ${}^5\text{D}_2$ Eu^{3+} transition a permanent change is produced in the refractive index of these glasses. The change in the refractive index is proportional to the change in temperature of the glass. This temperature profile can be approximated by a parabola, producing an effective thin lens with a positive focal length. In the crossed beam configuration each beam will produce its own thermal lens. This will result in a new crossing angle, $2\Theta'_S$ as shown in Fig. 31 and produce a change in the wavelength of the laser interference pattern.

We can predict the change in the crossing angle of the write beams by considering the thermal lense to act as an effective positive focal length lens placed in the path of each beam. The focal length can be calculated by using a method similar to that used in Chapter II.

In the long time limit the focal length of the effective lens was given by

$$f = \frac{\pi k w^2 \frac{\partial n}{\partial T}}{0.553 P A} \quad (62)$$

The parameters k , A and $\frac{\partial n}{\partial T}$ are properties of the sample and will be the same in both experiments. This leads to a focal length of

$$f_B = \frac{f_D P_D w_B^2}{P_B w_D^2} \quad (63)$$

where the D subscripts refer to the values quoted in Chapter II and the B subscripts refer to the values in this experiment. With $w_B = .5$ mm and $P_B = .07$ W a focal length of 38.563 mm is found. From this the change in Θ_S can be calculated and a new value for the wavelength of the laser interference pattern of $24.109 \mu\text{m}$ is calculated. This is in good agreement with the wavelength of the permanent LIG found from Eq. 58.

It is also possible to calculate the tilt angle Φ' shown in Fig. 30. From

$$\lambda_P = 2\Lambda_G \sin(\Phi_S - \Phi') \quad (64)$$

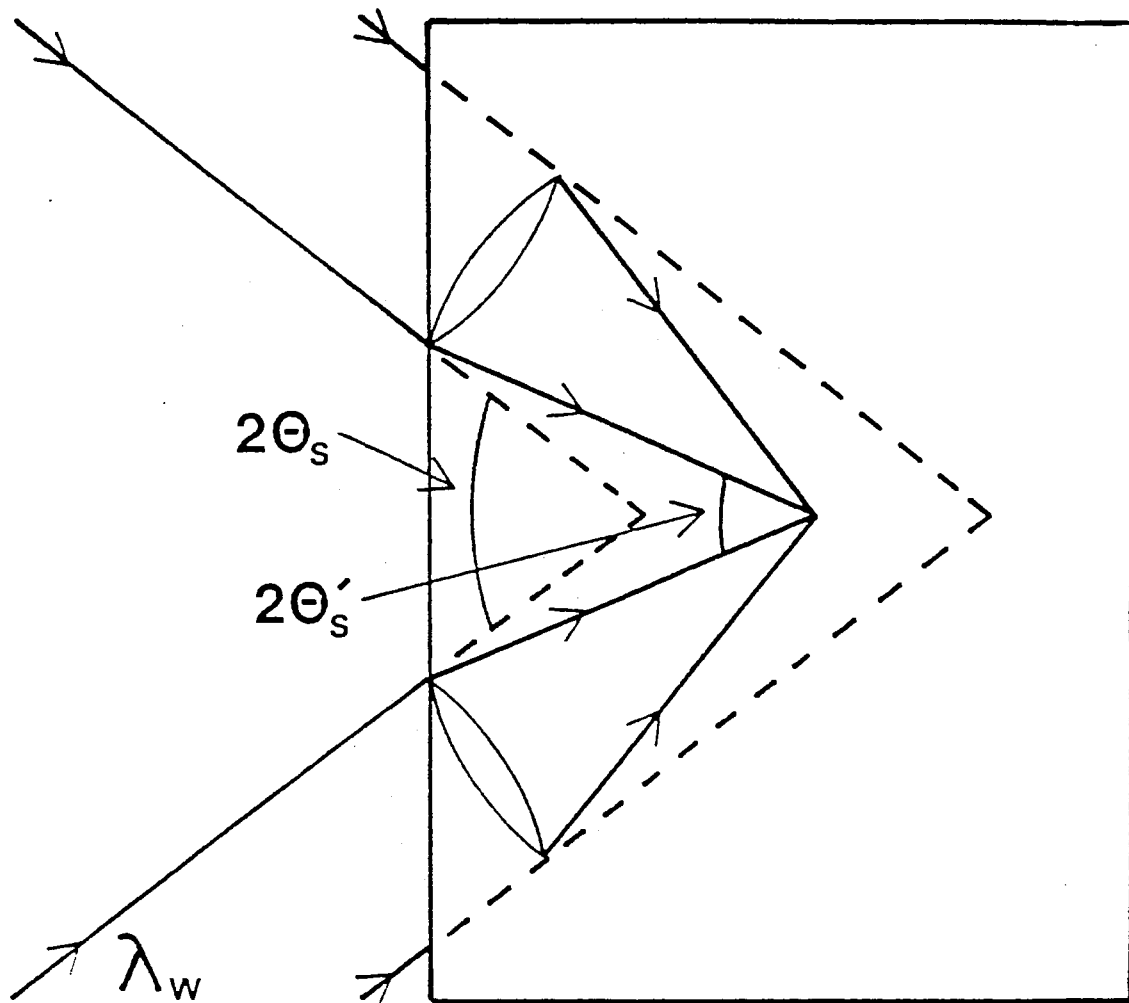


Figure 31. Definition of Angles Involved in Thermal Lensing Process.

and with the small angle approximation, the tilt angle will be given by

$$\Phi' = \Phi_S - \frac{\lambda_P}{2\Lambda_G}. \quad (65)$$

For this experiment a tilt angle of 5.860×10^{-3} radians is found. Notice that if Φ_S is measured from a reference other than the perpendicular to the sample, this will give the angle between the fringes and the reference.

The demultiplexing of the various frequencies of laser beams by the permanent LIG demonstrates the ability of using these holographic gratings as frequency selective notch filters. The filter can be tuned to different frequencies by rotating the sample to different angles. By stacking different holographic gratings in the same material several laser beams of different frequencies can be filtered simultaneously at the same angle of incidence. The limiting factor to the resolution of such a device is the fringe spacing of the permanent LIG and gratings can be formed with spacings more than an order of magnitude smaller than that of the grating used in these experiments.

Signal Modulation

The final experiment performed was to demonstrate amplitude modulation of the permanent LIG signal. After writing the permanent LIG as described above the write beams were turned on and off randomly. The result was an amplitude modulation of the signal beam as shown in Fig. 32. The top portion of the figure displays the time dependence of the write beams. The time scale of the experiment was approximately two minutes. The middle section depicts the intensity of the probe beam. As can be seen the probe beam is stable at a constant amplitude before interacting with the permanent LIG. The bottom section of Fig. 32 displays the time dependence of the intensity of the signal beam. It is seen that this is a superposition of the write beams and the probe beam resulting in an amplitude modulation of a constant beam.

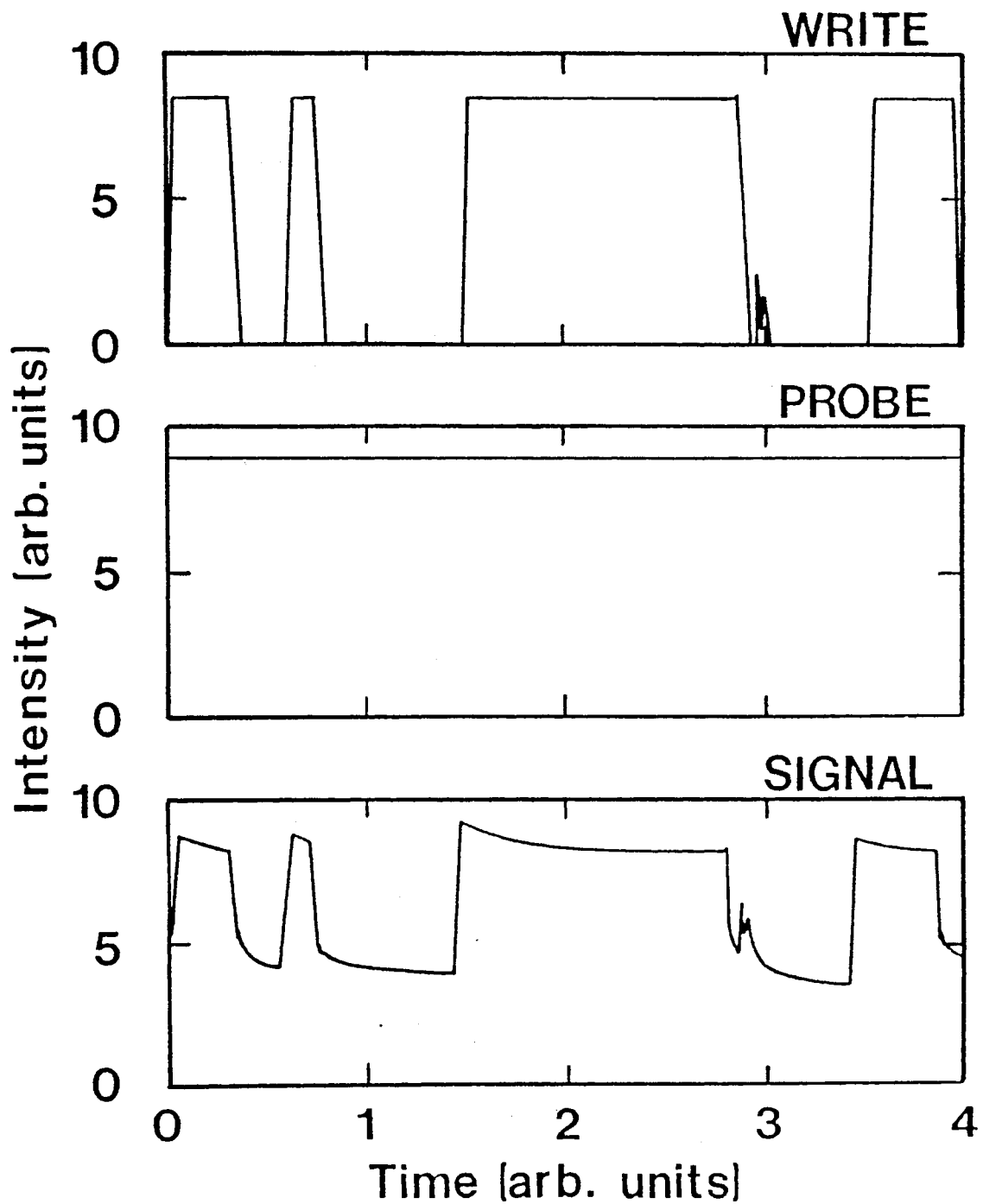


Figure 32. From Top to Bottom: Write, Probe, and Signal Beam Intensities in Modulation Experiment.

The time dependence of the intensity has been discussed previously and is given by[9]

$$I(t) = I_1 e^{-\frac{t}{\tau}} + I_2 \quad (66)$$

where I_1 and I_2 represent the transient and permanent contributions to the intensity and τ is the transient signal decay time. Thus when the write beams are on a total signal intensity of $I = I_1 + I_2$ will be measured, however when the write beams are turned off the transient signal will decay leaving a total intensity of $I = I_2$.

The rate at which the signal amplitude can be modulated is limited by the decay time of the transient component of the signal intensity. The decay time of the transient component has been associated with a population grating of the Eu^{3+} ions in the $^5\text{D}_0$ metastable state [9]. This limits the amplitude modulation by a decay time of 2.7 ms in this sample [47].

These results establish that a permanent LIG of this type can be utilized to allow one light beam to modulate the intensity of another light beam. This provides a means of transferring information from one beam to the other. The speed at which information can be transferred will depend on the modulation rate which is limited by the lifetime of the metastable state of the rare-earth ion and can vary between a kilohertz and a megahertz.

Summary and Conclusions

Three potential applications of permanent LIG's have been demonstrated in rare earth-doped glasses which have the ability to produce superimposed permanent and transient gratings. These include holographic storage, demultiplexing multifrequency laser beams, and signal modulation. The permanent LIG's can be written at room temperature with low laser power, have exhibited scattering efficiencies as high as 30%, and remain stable at room temperature indefinitely. [9]

These same permanent LIG's have been formed in a Pr^{3+} -doped silicate glass (70 SiO_2 , 15 Na_2O , 5 ZnO , 5 BaO and 5 Pr_2O_3 mol percent). The transient component of the signal in this glass is associated with the relaxation of the $^1\text{D}_2$

metastable state which has a lifetime of the order of microseconds. This will produce an increase of three orders of magnitude in the response time of the transient grating compared to the Eu^{3+} -doped glasses. This will allow for a faster amplitude modulation rate of light beams passing through the sample. The response time of the permanent holographic grating is still very slow in Pr^{3+} -doped glasses.

The above results are important when considering these glasses for potential optical devices. The type of glasses used in this work include common silicate glasses which can be made into fibers, and thus these permanent LIG devices can be used in fiber optic systems. A better knowledge of the microscopic structural change associated with the permanent LIG in these glasses will allow for optimization of these materials for specific applications.

CHAPTER IV

SUMMARY AND CONCLUSIONS

Summary of Thesis

This thesis has reported the results of experiments performed on rare earth-doped glasses and explained these results in terms of a two-level system model. In Chapter II the properties of the laser-induced gratings were discussed in terms of the properties of the active ion and the properties of the glass host. The rare earth ions Pr^{3+} , Nd^{3+} , Eu^{3+} , and Er^{3+} , were used as dopants in glass hosts and LIG signals were observed only in glasses doped with Pr^{3+} or Eu^{3+} . The characteristics of the LIG include a transient component which is associated with a population grating and a permanent component which is due to a structural rearrangement of the glass host in the local environment of the Pr^{3+} or Eu^{3+} . This structural rearrangement is produced by high energy phonons which are emitted when the Pr^{3+} or Eu^{3+} ion relaxes to a metastable state after being excited to a higher lying excited state. The difference in the time scales between the Pr^{3+} data and the Eu^{3+} data can be explained by considering the lifetime of the metastable state for each ion. For the Pr^{3+} ion the lifetime of the metastable state is of the order of microseconds whereas that of the Eu^{3+} ion is of the order of milliseconds. Thus the process of the ion being excited, relaxing to the metastable state through the emission of high energy phonons, then relaxing radiatively to its ground state occurs much more rapidly in Pr^{3+} than in Eu^{3+} . This produces phonons faster in the Pr^{3+} glass and will enhance the build-up or erasure of the permanent LIG.

The fact that no grating was observed in the Nd^{3+} or Er^{3+} samples was attributed to the energies of the phonons emitted when these ions relax from an excited state. In both cases the energies were much smaller than the energies of

the phonons emitted in the Pr^{3+} and Eu^{3+} samples. Thermal lensing measurements were performed to investigate the effects of the different vibrational modes. It was discovered that a permanent thermal lensing occurred in the Eu^{3+} sample when it was excited resonantly which is consistent with the results of the permanent LIG results. The off-resonance thermal lensing is due to absorption from the network of the glass host whereas resonant thermal lensing is produced through heat generated from the radiationless relaxation of the rare earth ions. The difference in mechanisms for the generation of phonons between the Eu^{3+} and Nd^{3+} is responsible for the different characteristics of the thermal lensing.

It was also discovered that no gratings were produced when the Eu^{3+} ions were excited directly into the metastable state further establishing the importance of the high energy phonons to grating formation. The importance of the rare earth ion concentration was demonstrated in samples which had different concentrations. Samples with higher concentrations of Eu^{3+} ions were found to produce stronger LIG signals than identical samples with lower concentrations.

Several glass hosts, all doped with Eu^{3+} , were investigated and it was found that phosphate, silicate, and borate formed permanent LIGs while fluoride and germanate glass hosts did not produce permanent LIGs. It was discovered that in fluoride glasses the Eu^{3+} ion relaxes radiatively from the highest lying excited states bypassing any nonradiative relaxation. Thus in these glasses no phonons are available for the creation of the permanent LIG.

The Raman and resonant Raman spectra were taken of several glasses. Those glasses which displayed permanent LIG signals were found to exhibit enhanced peaks at high frequency in the resonant Raman experiments indicating the necessity of these modes to permanent LIG formation and their strong coupling to the Eu^{3+} ion. Glasses which do not form permanent LIGs did not display these high energy vibrational modes.

The mass of the network modifier alkali-metal ion was found to have a direct affect on the permanent LIG formation. Lighter alkali-metal ions produce more efficient LIGs compared to heavier alkali-metal ions. This was explained

in terms of a two-level system model in which the ion can reside in two possible equilibrium configurations. This leads to a double minima potential well for the energy levels of the Eu^{3+} ion. It was found that this model does an excellent job of describing the permanent LIG signal characteristics and predicting activation energies for the glasses.

Chapter III exhibits potential applications of the glasses in optical devices. Applications to information storage and medical imaging are discussed along with using the permanent LIG to form a tunable, frequency selective filter. The final application involves using the permanent LIG to perform beam-to-beam coupling of information.

Future Work

Although the model proposed here does a good job of describing the permanent LIG characteristics there is still very little known about the microscopic structure of the two different configurations. Thought needs to be given as to how to extract this information. This is no easy task and may require the creation of new experimental techniques.

In the near future however, investigations need to be performed to better determine the role played by thermal lensing. Even though a very small amount of thermal lensing was seen in the Eu^{3+} sample, the Pr^{3+} and Er^{3+} samples exhibited much stronger thermal lensing. Experiments need to be performed to determine when thermal lensing becomes the dominate effect and how this is related to the phonon energy. Experiments should be performed to investigate the difference in the thermal lensing spatial profile between the silicate and phosphate glasses. This should also give interesting information about the different structures of these two materials.

A second investigation needs to be conducted using the Er^{3+} sample. It may be possible to excite this ion into a lower lying level which relaxes with the emission of high energy phonons. If this is the case it should be possible to form the permanent LIG.

Finally, one should constantly be on the lookout for new and exciting applications for permanent LIGs in these glasses. The applications described previously have aroused a considerable amount of interest and excitement outside the academic world. The best way to maintain this excitement and involve others is through device applications. This aspect is also important in obtaining funding through companies with a direct interest in the device but not necessarily in the basic science behind the permanent LIGs.

BIBLIOGRAPHY

1. Bures, J., J. Lapierre, and D. Pascale, *Appl. Phys. Lett.* 37, 860 (1980).
2. Hill, K. O., Y. Fujii, D. C. Johnson, and B. S. Kawasaki, *Appl. Phys. Lett.* 32, 647 (1978); B. S. Kawasaki, K. O. Hill, D. C. Johnson, and Y. Fujii, *Opt. Lett.* 3, 66 (1978).
3. Street, R. A., *Solid State Commun.* 24, 363 (1977).
4. Tanaka, K. and A. Osajima, *Appl. Phys. Lett.* 38, 481 (1981).
5. Dwon, J. H., C. H. Kwak, and S. S. Lee, *Opt. Lett.* 10, 568 (1985).
6. Pepper, D. M., and Amnon Yariv, in Optical Phase Conjugation, edited by R. A. Fisher, (Academic Press, London, 1983).
7. Eichler, H. J., P. Gunter, and D. W. Pohl, Laser-Induced Dynamic Gratings, (Springer-Verlag, Berlin, 1986).
8. Behrens, E. G., F. M. Durville, and R. C. Powell, *Opt. Lett.* 11, 653 (1986).
9. Durville, F. M., E. G. Behrens, and R. C. Powell, *Phys. Rev. B*, 34, 4213 (1986).
10. Hamilton, D. S., D. Heiman, J. Feinberg, and R. W. Hellwarth, *Opt. Lett.* 4, 124 (1979).
11. Behrens, E. G., R. C. Powell, and D. H. Blackburn, *J. Opt. Soc. Am. B*, to be published.
12. Jackson, J. D., Classical Electrodynamics, (Wiley and Sons, New York, 1975), p. 271.
13. Behrens, E. G., M.S. Thesis, Oklahoma State University (1986).
14. Feinberg, J., in Optical Phase Conjugation, edited by R. A. Fisher (Academic, New York, 1983) p. 417.
15. Layne, C. B., W. H. Lowdermilk, and M. J. Weber, *Phys. Rev. B* 16, 10 (1977).
16. Durville, F. M., and R. C. Powell, *J. Opt. Soc. Am. B* 7, 1934 (1987).
17. Gordon, J. P., R. C. C. Leite, R. S. Moore, S. P. S. Porto, and J. R. Whinnery, *J. Appl. Phys.* 36, 3 (1965).

18. Feldman, A., D. Horowitz, and R. Waxler, *IEEE J. Quantum Electron.* QE-9, 1054 (1973).
19. Boshier, M. G., and W. J. Sandle, *Opt. Commun.* 42, 371 (1982).
20. Carter, C., and J. M. Harris, *Appl. Opt.* 23, 476 (1984).
21. Bialkowski, S. E., *Spectroscopy* 1, 26 (1986).
22. Twarowski, A. J., and D. S. Klinger, *Chem. Phys.* 20, 253 (1977).
23. Shuker, R., and R. W. Gammon, *Phys. Rev. Lett.* 25, 222 (1970).
24. Galeener, F. L., and P. N. Sen, *Phys. Rev. B* 17, 1928 (1978).
25. Wong, J. and C. A. Angell, *Appl. Spectr. Rev.* 4, 155 (1971).
26. Mozzi, R. L., and B. E. Warren, *J. Appl. Cryst.* 3, 251 (1970).
27. See, for example, Irion, M., and M. Couzi, *J. Solid State Chem.* 31, 285 (1980).
28. Almeida, R. M., and J. D. Mackenzie, *J. Chem. Phys.* 74, 5954 (1981).
29. Bobovich, Ya. S., *Opt. Spectrosc.* 13, 274 (1962).
30. Nelson, B. N., and G. J. Exarhos, *J. Chem. Phys.* 71, 2739 (1979).
31. See, for example, Bell, R. J., N. F. Bird, and P. Dean, *J. Phys. C* 2, 299 (1968).
32. Hass, M., *J. Phys. Chem. Solids* 31, 415 (1970).
33. Matson, D. W., S. K. Sharma, and J. A. Philpotts, *J. Non-Cryst. Solids* 58, 323 (1983).
34. DeShazer, L. G., private communication.
35. Sauer, C. L., Ph.D. thesis, University of Southern California, 1980.
36. Kittel, C., Introduction to Solid State Physics, (John Wiley & Sons, New York, 1976).
37. Kogelnik, H., *Bell System Tech. J.* 48, 2909 (1969).
38. Phillips, W. A., in Amorphous Solids: Low-Temperature Properties (Topics in Current Physics 24), edited by W. A. Phillips, (Springer-Verlag, Berlin, 1981).
39. Park, D., Introduction to the Quantum Theory, (McGraw-Hill Book Co. New York 1964), p.100.

40. Phillips, W.A. J. Low Temp. Phys.,4, No. 3/4, 351 (1972).
41. Brawer, S. A. and W. B. White, J. Chem. Phys. 63, 2421 (1975); S. Brawer, Phys. Rev. B 11, 3173 (1975).
42. Wicksted, J. P., and G. W. Gangwere, private communication.
43. Kawasaki, B. S., K. O. Hill, D. C. Johnson and Y. Fujii, Opt. Lett. 3, 66 (1978).
44. Sincerbox, G. T., and G. Roosen, Appl. Opt. 22, 690 (1983).
45. Powell, R. C., F. M. Durville, E. G. Behrens, and G. S. Dixon, J. Lumin. (40-41), 68 (1988).
46. Gunter, P., Physics Reports, 93, No. 4, 199 (1982).
47. Gang, X. and R.C. Powell, J. Appl. Phys., 57, 1299, (1985).
48. Merzbacher, E., Quantum Mechanics, 2nd edition, (Wiley & Sons, New York, 1970).
49. Anderson, P. W., Phys. Rev. B 34, 953 (1986).
50. Black, J. L., Phys. Rev. B 17, 2740 (1978).
51. Phillips, W. A., Rep. Prog. Phys. 50, 1657 (1987).
52. Golding, B., and J. E. Graebner, in Amorphous Solids: Low-Temperature Properties (Topics in Current Physics 24), edited by W. A. Phillips, (Springer-Verlag, Berlin, 1981).
53. DiBartolo, B., Optical Interactions in Solids, (Wiley & Sons, New York, 1968).
54. Kittel, C. Quantum Theory of Solids, (Wiley & Sons, New York, 1963).

APPENDIX

The two-level-system theory proposes that an atom or group of atoms in the solid can arrange themselves into two possible equilibrium configurations. This will lead to a potential of the form shown in Fig. 27. Each well will be of the form of a simple harmonic oscillator. The energy levels of the particle are calculated by using as the starting point the solutions to the single well problem, this is known as the well, non-diagonal or localized representation. In this localized representation we will take $|i, 1\rangle$ and $|j, 2\rangle$ as the basis states of the Hamiltonians H_1 and H_2 with eigenvalues E_1 and E_2 respectively:

$$H_1 |i, 1\rangle = E_1^i |i, 1\rangle \quad (67)$$

$$H_2 |j, 2\rangle = E_2^j |j, 2\rangle. \quad (68)$$

The states of a well are all orthogonal to each other and normalized, however the states of well 1 are not orthogonal to the states of well 2. In seeking a solution for the combined wells it is assumed that any higher lying levels are far enough removed so as not to enter into the mixing of the states, thus the i, j notation will be dropped and each state is the ground state of the appropriate potential V_1 or V_2 . The Hamiltonian for the asymmetric double well is

$$H = -\frac{\hbar^2}{2m}\nabla^2 + V_1 + V_2 \quad (69)$$

$$= H_1 + (V - V_1) \quad (70)$$

$$= H_2 + (V - V_2) \quad (71)$$

where H_1 and H_2 are the individual well Hamiltonians. In this representation the Hamiltonian becomes

$$\langle i | H | j \rangle = \begin{pmatrix} \langle 1 | H | 1 \rangle & \langle 1 | H | 2 \rangle \\ \langle 2 | H | 1 \rangle & \langle 2 | H | 2 \rangle \end{pmatrix}. \quad (72)$$

The diagonal elements of the matrix can be expressed more explicitly as

$$\langle 1 | H | 1 \rangle = E_1 + \langle 1 | V - V_1 | 1 \rangle \quad (73)$$

$$\langle 2 | H | 2 \rangle = E_2 + \langle 2 | V - V_2 | 2 \rangle \quad (74)$$

so that

$$H \equiv \langle i | H | j \rangle \quad (75)$$

$$H = \begin{pmatrix} E_1 + \langle 1 | V - V_1 | 1 \rangle & \langle 1 | H | 2 \rangle \\ \langle 2 | H | 1 \rangle & E_2 + \langle 2 | V - V_2 | 2 \rangle \end{pmatrix}. \quad (76)$$

If the extension of each localized wavefunction into the barrier is small, the terms $\langle i | V - V_i | i \rangle$ will be small compared to E_i the ground state energy of well i . This leaves the following expression for the Hamiltonian

$$H = \begin{pmatrix} E_1 & H_{12} \\ H_{21} & E_2 \end{pmatrix}. \quad (77)$$

Since the wavefunctions are harmonic oscillator wavefunctions and the Hamiltonian is real $H_{12} = H_{21}$

To find the eigenvalues of a 2x2 matrix is extremely simple and usually it is also easy to find the normalized eigenvectors. Sometimes however, this can be extremely complicated as in this case. In order to simplify the process the following procedure was utilized. Using the half-sum and half-difference of the diagonal elements E_1 and E_2 , H can be expressed as

$$H = \begin{pmatrix} \frac{1}{2}(E_1 + E_2) & 0 \\ 0 & \frac{1}{2}(E_1 + E_2) \end{pmatrix} + \begin{pmatrix} \frac{1}{2}(E_1 - E_2) & H_{12} \\ H_{12} & -\frac{1}{2}(E_1 - E_2) \end{pmatrix}. \quad (78)$$

From this it is seen that the operator H itself can be broken down as follows

$$H = \frac{1}{2}(E_1 + E_2)1 + \frac{1}{2}(E_1 - E_2)K \quad (79)$$

where

$$K = \begin{pmatrix} 1 & \frac{2H_{12}}{(E_1 - E_2)} \\ \frac{2H_{12}}{(E_1 - E_2)} & 1 \end{pmatrix}. \quad (80)$$

It can be seen from Eq. 79 that H and K have the same eigenvectors

$$H|\Psi_{\pm}\rangle = E_{\pm}|\Psi_{\pm}\rangle \quad (81)$$

$$K|\Psi_{\pm}\rangle = \kappa_{\pm}|\Psi_{\pm}\rangle \quad (82)$$

with eigenvalues for H

$$E_{\pm} = \frac{1}{2}(E_1 + E_2) + \frac{1}{2}(E_1 - E_2)\kappa_{\pm}. \quad (83)$$

To solve for the eigenvectors of H let

$$\tan 2\Theta = \frac{2H_{12}}{E_1 - E_2}. \quad (84)$$

Thus K becomes

$$K = \begin{pmatrix} 1 & \tan 2\Theta \\ \tan 2\Theta & -1 \end{pmatrix}. \quad (85)$$

The eigenvalues for this matrix are

$$\kappa_{\pm} = \pm \frac{1}{\cos 2\Theta}. \quad (86)$$

Using Eqs. 84 and 86 it is found that

$$\frac{1}{\cos 2\Theta} = \frac{\sqrt{(E_1 - E_2)^2 + 4H_{12}^2}}{E_1 - E_2} \quad (87)$$

and for the eigenvalues of H

$$E_{\pm} = \frac{1}{2}(E_1 + E_2) \pm \frac{1}{2}\sqrt{(E_1 - E_2)^2 + 4H_{12}^2}. \quad (88)$$

To calculate the eigenvectors of H let a and b be the components of $|\Psi_+\rangle$ on $|1\rangle$ and $|2\rangle$. Thus

$$\begin{pmatrix} 1 & \tan 2\Theta \\ \tan 2\Theta & -1 \end{pmatrix} \begin{pmatrix} a \\ b \end{pmatrix} = \frac{1}{\cos 2\Theta} \begin{pmatrix} a \\ b \end{pmatrix}. \quad (89)$$

Solving for b in terms of a gives $b = a \tan \Theta$. Next, normalize the components by requiring that $\Psi^*\Psi = 1$. This gives $a = \cos \Theta$ and $b = \sin \Theta$.

Using a similar procedure for $|\Psi_- \rangle$ the components are found to be $a = \sin \Theta$ and $b = -\cos \Theta$. The new wavevectors are given by

$$\Psi_+ = \cos \Theta |1 \rangle + \sin \Theta |2 \rangle \quad (90)$$

$$\Psi_- = \sin \Theta |1 \rangle - \cos \Theta |2 \rangle . \quad (91)$$

Notice if we take the zero of energy to be halfway between E_1 and E_2 then the eigenfunctions Ψ_- and Ψ_+ have energies in the true, diagonal or energy representation of $\pm E/2$ where

$$E = \sqrt{\Delta^2 + \Delta_0^2} \quad (92)$$

and

$$2H_{12} = 2 \langle 1|H|2 \rangle = \Delta_0 \quad (93)$$

$$E_1 - E_2 = \Delta. \quad (94)$$

The exact form of Δ_0 has been evaluated for specific potentials [48]. The results imply an exponential dependence of Δ_0 on the barrier height and well separation. The use of a particular detailed form cannot be justified in amorphous solids because the microscopic structure is uncertain, thus a simplified expression is usually adequate

$$\Delta_0 = \hbar \tilde{\omega}_0 \exp(-\lambda) \quad (95)$$

$$= \hbar \tilde{\omega}_0 \exp \left[-d(2mV_0/\hbar^2) \right] \quad (96)$$

where $\hbar \tilde{\omega}_0$ is approximately equal to $(E_1 + E_2)/2$, d is the well separation, V_0 the barrier between the two wells, and m is the particle mass.

For this problem as with any problem involving two energy levels there exists a formal analogy to the spin 1/2 particle in a magnetic field. Introducing the Pauli spin matrices

$$\sigma_x = \begin{pmatrix} 0 & 1 \\ 1 & 0 \end{pmatrix} \quad (97)$$

$$\sigma_y = \begin{pmatrix} 0 & -i \\ i & 0 \end{pmatrix} \quad (98)$$

$$\sigma_z = \begin{pmatrix} 1 & 0 \\ 0 & -1 \end{pmatrix} \quad (99)$$

the Hamiltonian in the diagonal representation can be written as

$$H = \frac{1}{2}E\sigma_z. \quad (100)$$

The advantage to using this form becomes obvious when interactions with electric and acoustic fields are discussed later.

The time dependence of the tunneling state is defined by specifying the complex amplitudes $a_+(t)$ and $a_-(t)$ of the two lowest states with eigenfunctions $\Psi_+(\vec{r})$ and $\Psi_-(\vec{r})$. At the low temperatures considered here higher lying states can be neglected. The general time-dependent wavefunction is

$$\Phi = a_+(t)\Psi_+(\vec{r}) \exp\left(\frac{-iE_+t}{\hbar}\right) + a_-(t)\Psi_-(\vec{r}) \exp\left(\frac{-iE_-t}{\hbar}\right) \quad (101)$$

where E_+ and E_- are the energies of the states Ψ_+ and Ψ_- and for normalization purposes $a_+a_+^* + a_-a_-^* = 1$.

Variations of $a_+(t)$ and $a_-(t)$ occur through the time dependent Schrodinger equation by interaction with external fields. Two simplifications can be made in treating electromagnetic and strain fields. First, the frequency needed to induce transitions between the two levels is of the order of 20 GHz for states contributing to thermal properties below 1K. This corresponds to wavelengths of 10 mm for photons and 100 nm for acoustic phonons, both much larger than the spatial extent of the two-level state. Thus the dipole approximation, where the local electric and strain fields are treated as constants, is valid. The second simplification arises from the fact that the dominant effect of these uniform fields affects the asymmetry but changes in the barrier height can be ignored [49, 38]. Therefore the perturbation in the localized representation will be diagonal. Taking as an example the perturbation arising from the strain field which is given by [50]

$$H'_s = -e\gamma \begin{pmatrix} 1 & 0 \\ 0 & -1 \end{pmatrix} \quad (102)$$

where γ is the deformation-potential tensor given by $(1/2)(\partial\Delta/\partial e)$ and e is the local strain tensor. To simplify e and γ have been written as averages over orientations. Equation 102 is written in terms of the same localized basis used in Eq. 77. To change to the diagonal basis use the transformation matrix derived from Eqs. 90 and 91,

$$T = \begin{pmatrix} \cos \Theta & \sin \Theta \\ \sin \Theta & -\cos \Theta \end{pmatrix}. \quad (103)$$

So the strain field perturbation in the diagonal basis becomes

$$H_s = T^\dagger H'_s T \quad (104)$$

$$H_s = -e\gamma \begin{pmatrix} \cos^2 \Theta - \sin^2 \Theta & 2 \cos \Theta \sin \Theta \\ 2 \cos \Theta \sin \Theta & \sin^2 \Theta - \cos^2 \Theta \end{pmatrix} \quad (105)$$

which is simplified in the following steps:

$$H_s = -e\gamma \begin{pmatrix} \cos 2\Theta & \sin 2\Theta \\ \sin 2\Theta & \cos 2\Theta \end{pmatrix} \quad (106)$$

or with

$$\cos 2\Theta = \frac{E_1 - E_2}{\sqrt{(E_1 - E_2)^2 + 4H_{12}^2}} \quad (107)$$

$$= \frac{\Delta}{\sqrt{\Delta^2 + \Delta_0^2}} \quad (108)$$

$$= \frac{\Delta}{E} \quad (109)$$

$$\sin 2\Theta = \cos(2\Theta) \tan(2\Theta) \quad (110)$$

$$= \frac{\Delta}{E} \frac{2H_{12}}{E_1 - E_2} \quad (111)$$

$$= \frac{\Delta}{E} \frac{\Delta_0}{\Delta} \quad (112)$$

$$= \frac{\Delta_0}{E} \quad (113)$$

$$H_s = -e\gamma \begin{pmatrix} \frac{\Delta}{E} & \frac{\Delta_0}{E} \\ \frac{\Delta_0}{E} & -\frac{\Delta}{E} \end{pmatrix}. \quad (114)$$

The same procedure can be used for the perturbation due to an electromagnetic field which is [51]

$$H'_e = -\vec{p}_0 \cdot \vec{F} \begin{pmatrix} 1 & 0 \\ 0 & -1 \end{pmatrix} \quad (115)$$

where \vec{p}_0 is the electric dipole moment when one well is occupied and is defined as $(1/2)(\partial\Delta/\partial\vec{F})$ and \vec{F} is the electric field. This leads to

$$H_e = -\vec{p}_0 \cdot \vec{F} \begin{pmatrix} \frac{\Delta}{E} & \frac{\Delta_0}{E} \\ \frac{\Delta_0}{E} & -\frac{\Delta}{E} \end{pmatrix}. \quad (116)$$

Taking advantage of the Pauli spin matrices the interaction Hamiltonian can then be expressed as

$$H_{int} = -\left(\frac{\Delta}{E}\sigma_z + \frac{\Delta_0}{E}\sigma_x\right)\vec{p}_0 \cdot \vec{F} - \left(\frac{\Delta}{E}\sigma_z + \frac{\Delta_0}{E}\sigma_x\right)e\gamma. \quad (117)$$

The off-diagonal term σ_x is responsible for transitions between Ψ_+ and Ψ_- whereas the diagonal term σ_z changes their relative energy.

In many cases a simpler model is effective which is known as the two-level system model in which the interaction between the diagonal and off-diagonal elements is ignored. The TLS model uses a single parameter E to describe the energy difference between the two levels. The interaction Hamiltonian becomes

$$H_{int} = -\left(\frac{1}{2}\mu\sigma_z + \mu'\sigma_x\right)\xi - \left(\frac{1}{2}D\sigma_z + M\sigma_x\right)e. \quad (118)$$

The interaction between the tunneling states of the TLS and the phonons or photons can be expressed using a rate-equation approach [52]

$$\dot{p}_+ = -p_+\omega_{+-} + p_-\omega_{-+} \quad (119)$$

$$\dot{p}_- = p_+\omega_{+-} - p_-\omega_{-+} \quad (120)$$

where p_+ and p_- are the populations of states $+$ and $-$, \dot{p}_+ and \dot{p}_- are the change in population per unit time, ω_{+-} is the transition probability from state $+$ to state $-$. The population is assumed normalized so that $p_+ + p_- = 1$. In thermal equilibrium

$$\dot{p}_+ = \dot{p}_- = 0 \quad (121)$$

so that

$$p_+^0 \omega_{+-} = p_-^0 \omega_{-+} \quad (122)$$

where p_+^0 and p_-^0 are the equilibrium values of p_+ and p_- . From statistical mechanics the ratio of the populations is given by the Boltzmann factor

$$\frac{p_+^0}{p_-^0} = \exp\left(\frac{E}{kT}\right) \quad (123)$$

where E is the energy difference between states $+$ and $-$. Using Eq. 122 this can be expressed alternatively as

$$\frac{p_+^0}{p_-^0} = \frac{\omega_{+-}}{\omega_{-+}} \quad (124)$$

$$= \exp\left(\frac{-E}{kT}\right). \quad (125)$$

Replacing p_+ in Eq. 120 with $1 - p_-$ gives

$$\dot{p}_- = (1 - p_-)\omega_{+-} - p_- \omega_{-+} \quad (126)$$

$$\dot{p}_- = -p_-(\omega_{+-} + \omega_{-+}) + \omega_{+-}. \quad (127)$$

This defines a relaxation time τ where

$$\tau^{-1} = (\omega_{+-} + \omega_{-+}) \quad (128)$$

$$= \omega_{-+} \left[1 + \exp\left(\frac{E}{kT}\right)\right]. \quad (129)$$

This relaxation time is referred to as T1 the spin-lattice relaxation time.

For a weak strain field the transition probability for a one-phonon process can be calculated from time-dependent perturbation theory. The probability per unit time that the TLS in state Ψ_- absorbs a phonon and jumps to state Ψ_+ is given by [53]

$$\omega_{-+} = \frac{2\pi}{\hbar} \sum_{\alpha} |\langle \Psi_f | H_{int} | \Psi_i \rangle|^2 g(E) \delta(\hbar\omega - E) \quad (130)$$

where the sum over α is to account for all phonon polarizations and $g(E)$ is the phonon density of states. From Eq. 117 it is seen that in order to calculate the matrix element the local strain e needs to be evaluated.

The local strain is defined by the strain tensor $e_{\alpha\beta}$

$$e_{\alpha\beta} = \frac{1}{2} \left(\frac{\partial u_\alpha}{\partial x_\beta} + \frac{\partial u_\beta}{\partial x_\alpha} \right) \quad (131)$$

where u is the displacement of any point from its equilibrium and $\alpha, \beta = 1, 2, 3$. This strain is a result of the distortion of the lattice which is caused by thermal vibrations. In Eq. 102 e was considered as an average over orientations thus it simplifies to

$$e = \frac{\partial u}{\partial x} \Big|_{x=0} . \quad (132)$$

The displacement u is given by [54]

$$u = \sum_q \left(\frac{\hbar}{2\rho\omega_q} \right)^{\frac{1}{2}} (e^{iqx} b_q + e^{-iqx} b_q^\dagger) \quad (133)$$

where ρ is the density of the sample, b_q and b_q^\dagger are the annihilation and creation operators for the q^{th} vibrational oscillator respectively. e is found to be

$$e = i \sum_q \left(\frac{\hbar}{2\rho\omega_q} \right)^{\frac{1}{2}} q (b_q - b_q^\dagger). \quad (134)$$

For the absorption of a phonon the matrix element in Eq. 117 becomes

$$\langle \Psi_f | H_{int} | \Psi_i \rangle = \langle \Psi_f | -\frac{\Delta_0}{E} \gamma_\alpha i \sum_q \left(\frac{\hbar}{2\rho\omega_q} \right)^{\frac{1}{2}} q b_q | \Psi_i \rangle . \quad (135)$$

Note that the σ_z terms vanish since they connect identical states which does not allow for the absorption or emission of a phonon. In order to evaluate the affect of the phonon annihilation and creation operators on the wavefunctions express Ψ_+ and Ψ_- in terms of the TLS and the phonon field as

$$|\Psi_f \rangle = |\Psi_+ \rangle |n_1 \rangle |n_2 \rangle \dots |n_q - 1 \rangle \dots \quad (136)$$

$$|\Psi_i \rangle = |\Psi_- \rangle |n_1 \rangle |n_2 \rangle \dots |n_q \rangle \dots \quad (137)$$

The action of b_q on $|\Psi_i \rangle$ is

$$b_q |\Psi_i \rangle = \sqrt{n_q} |\Psi_- \rangle |n_1 \rangle |n_2 \rangle \dots |n_q - 1 \rangle \dots \quad (138)$$

so that the matrix element becomes

$$\begin{aligned} \langle \Psi_f | H_{int} | \Psi_i \rangle &= -i \frac{\Delta_0}{E} \langle \Psi_+ | \langle n_1 | \dots \gamma_\alpha \sum_q \left(\frac{\hbar}{2\rho\omega_q} \right)^{\frac{1}{2}} q b_q \dots | n_1 \rangle | \Psi_- \rangle \quad (139) \\ &= -i \frac{\Delta_0}{E} \gamma_\alpha \left(\frac{\hbar}{2\rho\omega_q} \right)^{\frac{1}{2}} q \sqrt{n_q} \quad (140) \end{aligned}$$

where n_q is the Bose factor $[\exp(E/kT) - 1]^{-1}$. The absolute square of Eq. 139 is what is needed for Eq. 130 which is

$$| \langle \Psi_f | H_{int} | \Psi_i \rangle |^2 = \frac{\Delta_0^2}{E^2} \gamma_\alpha^2 \frac{\hbar q^2 n_q}{2\rho\omega_q}. \quad (141)$$

The transition probability is then

$$\omega_{-+} = \frac{2\pi}{\hbar} \sum_\alpha \frac{\Delta_0^2}{E^2} \gamma_\alpha^2 \frac{\hbar q^2 n_q}{2\rho\omega_q} g(E) \delta(\hbar\omega - E). \quad (142)$$

Using the dispersion relation

$$q = \frac{\omega}{v} \quad (143)$$

and the Debye density of states per unit volume

$$g(E) = \frac{\omega^2}{2\pi^2 \hbar v^3} \quad (144)$$

Eq. 142 becomes

$$\omega_{-+} = \sum_\alpha \frac{\gamma_\alpha^2 E \Delta_0^2}{v_\alpha^5 2\pi \rho \hbar^4} [\exp(E/kt) - 1]^{-1} \delta(\hbar\omega - E). \quad (145)$$

Thus a spin-lattice relaxation rate is given by

$$\tau^{-1} = \sum_\alpha \frac{\gamma_\alpha^2 E \Delta_0^2}{v_\alpha^5 2\pi \rho \hbar^4} \coth(E/2kT). \quad (146)$$

✓
VITA

EDWARD GRADY BEHRENS

Candidate for the Degree of

Doctor of Philosophy

Thesis: PROPERTIES AND APPLICATIONS OF LASER INDUCED GRATINGS IN RARE EARTH DOPED GLASSES

Major Field: Physics

Biographical:

Personal Data: Born in Tulsa, Oklahoma, December 14, 1961, the son of Edward and Dolores G. Behrens. Married to Linda J. Townsend on June 1, 1985.

Education: Graduated from C. E. Donart High School, Stillwater, Oklahoma, in May, 1980; received Bachelor of Science Degree from Southeastern Oklahoma State University in May 1984 with a double major in physics and math; received the Master of Science Degree from Oklahoma State University in December, 1986, with a major in physics; completed the requirements for the Doctor of Philosophy Degree at Oklahoma State University in July, 1989.

Professional Experience: Undergraduate Research Assistant, Southeastern Oklahoma State University, August 1980 to May 1984; Summer Intern, Oak Ridge National Laboratory, June 1983 to August 1983; Graduate Teaching Assistant, Oklahoma State University, August 1984 to December 1984; Graduate Research Assistant, Oklahoma State University, January 1985 to Present; Research Scientist, Fibertek, May 1987 to August 1987. Member of the American Physical Society, Optical Society of America, and Alpha Phi Alpha.